Alexeev V.A.[1], Bagulya A.V.[2], Volkov A.E.[2], Goncharova L.A.[2], Gorbunov S.A.[2], Kalinina G.V.[1], Konovalova N.S.[2], Okateva N.M.[2], Pavlova T.A.[1], Polukhina N.G.[2], Starkov N.I.[2], Than Naing Soe[2], Chernyvsky M.M.[2], Shchedrina T.V.[2] The track studies of olivine crystals in the pallasites. UDC 550.42

[1]Vernadsky Institute of Geochemistry and Analytical Chemistry RAS, Moscow (AVAL37@mail.ru),
[2]Lebedev Physical Institute RAS, Moscow (polukhina@sci.lebedev.ru)

Abstract. The results of the track investigations in olivine crystals from pallasites conducted for the purpose of detecting and studying the nuclei tracks of transuranium elements in the composition of galactic cosmic rays (GCR) are presented. Distributions of the formation rates of tracks of VH cosmic ray nuclei in olivine crystals versus depth in pallasites with the different pre-atmospheric sizes are calculated. The obtained dependences were used to analyze the data on the track density in olivine crystals from pallasite Marjalahti. In three crystals, the high gradient of tracks density was first found. This gradient, most likely, is due to the exposure onto this crystal by the VH-nuclei of cosmic rays at a shielding layer thickness less than ~n100 μm. Such a scenario assumes a complex exposure history of the meteorite.

Keywords*: superheavy nuclei, tracks, galactic cosmic rays, olivine, pallasites.*

Introduction. When investigating the prevalence of heavy and super heavy chemical elements (with the charge of the nucleus Z>26), the most promising for the composition of galactic cosmic rays (GCR) is the attraction of natural detectors, iron-stone meteorites of the pallasite class (Bagulya et al., 2013). One of the undeniable advantages of these natural detectors is the duration of exposure - meteorites are in outer space for tens and hundreds of millions of years. During this time, they are exposed to cosmic rays, including heavy and super heavy nuclei. Irradiation is accompanied by the formation in olivine crystals of tracks – of radiation-stimulated changes in the microstructure of these crystals, which make it possible to identify the charge of the nuclei that formed these tracks.

Calculation results. In the study of track distributions in pallasite olivine crystals, the calculated rates of track formation (ρ/t, where ρ is the track density, cm^{-2} and t is the exposure age of the meteorite, million years) are usually used for the pyroxene of the chondrites, depending on the depth of the sample (d, cm) in meteorites of different pre-atmospheric sizes (Bhattachrja et al., 1973) with subsequent correction to olivine of pallasites. To unify procedures for analyzing distributions, based on the results (Bhattachrja et al., 1973), calculations were made of the depth distribution of the rate of formation of tracks of the VH nuclei (24≤Z≤28) in olivine of pallasites of different pre-atmospheric sizes. In these calculations, it was taken into account that the rate of formation of tracks in pyroxene is higher than in olivine. The excess ratio was found to be 1.8 ± 0.5; 2.4 ± 0.5; 2.1; 2.9 (according to data (Aaloe et al., 1979; Pereligin et al, 1975), etc).

In the present study the mean significance of these values, 2.3 ± 0.5, was taken for the calculations. In the calculations it was taken into account that the path length of VH nuclei in pallasite matter is 1.4 times less than in the matter of chondrites (Aaloe et al., 1979). According to these amendments, after digitizing the depth distribution curves in the dependencies (Bhattachrja et al., 1973), the coordinates of the selected points decreased: the ordinates (values ρ/t) in 2.3 times, and abscissas (values d) in 1.4 times. The set of coordinate values thus obtained for each new value of the radius R of the pre-atmospheric pallasite body was approximated by a dependence of the form:

$$\lg(\rho/t)=A + Bd^C \qquad (1)$$

It was earlier shown (Alexeev, 2004) that the curves characterizing the change in $\lg(\rho/t)$ on the depth in the calculations (Bhattachrja et al., 1973) can be described with high accuracy (up to several %) by the equation of the form (1). The coefficients A, B, and C were calculated according to the program developed for this purpose, which makes it possible to minimize the sum of the squared deviations of the values of $\lg(\rho/t)$ calculated from formula (1) from corresponding data in the work (Bhattacharya et al., 1973).

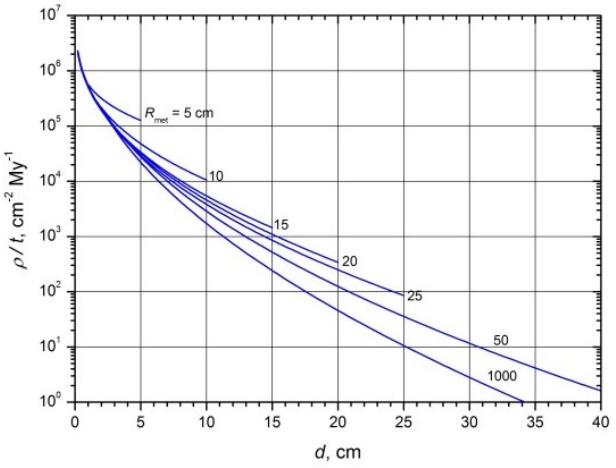

Fig. 1. The track formation rate of cosmic-ray VH-nuclei (ρ/t) as a function of depth (d) in olivine of pallasites of a pre-atmospheric radius R.

The dependences of the A, B, and C parameters of the approximating curves on the pre-atmospheric radius of the pallasites R allowed us to calculate the

depth distributions of the of track formation rates in pallasites for the chosen values of R = 5, 10, 15, 20, 25, 50 and 1000 cm. The dependences obtained are shown in **Fig. 1** and can be used to estimate the interval of values of d in pallasites of different pre-atmospheric sizes. A similar recalculation procedure was performed for the depth dependence of ρ/t in the interval d = 0.001-1 cm for R = 5 cm (**Fig. 2**).

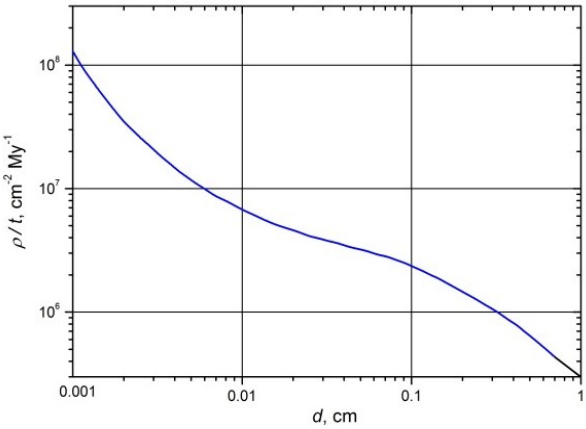

Fig. 2. The same (see Figure 1) for values of d <1 cm.

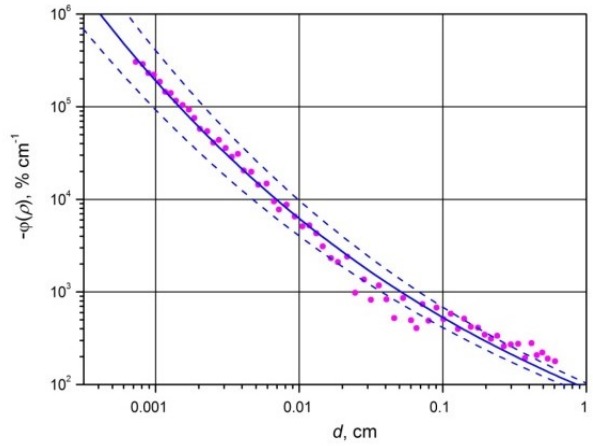

Fig. 3. Gradient of the rate of track formation in olivine crystals from pallasites as a function of depth d (for d < 1 cm). The points correspond to the gradient values for the individual sections of the curve in Fig. 2. The solid curve is an approximation by the equation $\varphi(\rho) = 10^{1.97 \cdot \exp(-0.330 \cdot \lg d)}$. The dashed line is ± 2σ.

On the basis of the obtained data, the changes in track density, $\varphi(\rho)$ as a function of depth were calculated for d = 0.001-1 cm. The results of the calculations are shown in **Fig. 3**. The points correspond to different sections of the curve in Fig. 2. The value of the gradient was calculated by the formula characterizing the relative changes in the track density in the intervals $d_1 \div d_2$ corresponding to the values of track density ρ_1 and ρ_2:

$$\varphi(\rho) = \frac{\frac{(\rho 2 - \rho 1)}{(\rho 2 + \rho 1)/2}}{d2 - d1} \times 100, \% \, cm^{-1} \qquad (2)$$

It can be seen from the presented estimates that the gradient of the VH nucleus track formation rates varies from ~100% cm^{-1} at a depth of about 1 cm up to ~10^5 % cm^{-1} for d ~0.001 cm. Such a high gradient of tracks for small values of d can be formed when the irradiating the crystal surface by cosmic-ray VH-nuclei during solar flares. Cases of such irradiation are observed, in particular, in pyroxene crystals of stony meteorites in the early stages of the formation of parent bodies (Goswami et al., 1984). In this case the gradient is manifested only for a small thickness of the shielding layer, less than ~500 μm. The gradients calculated in the same way for the depth dependences of the track formation rates in the olivine of pallasites of different sizes shown in Fig. 1 were less than 100% cm^{-1} for values of d > 1 cm.

Analysis of olivine samples of Marjalahti pallasites. In the process of searching for tracks of super heavy nuclei, we have studied in this work about 300 olivine crystals of Marjalahti pallasite. The distribution of track densities in these crystals accounts on a wide range of values: $\rho = 1.0 \cdot 10^3 \div 6.3 \cdot 10^6$ cm^{-2}. At the same time, the most of the crystals (about 90%) have the track densities in the smaller range: $\rho = 6.3 \cdot 10^5 \div 6.3 \cdot 10^6$ cm^{-2} with a maximum in the interval $(2.5 \div 4.0) \cdot 10^6$ cm^{-2}. According to the previous studies, the pre-atmospheric size of Marjalahti is ~ 20 cm (Kolesnikov et al., 1977, Perelygin et al., 1975), and its exposure age t was found to be about 200 million years. In subsequent calculations, the value t = 185 ± 17 Ma is used (Herzog et al., 2015). Taking these values into account, the depth of location of most of the olivine crystals studied in this work, according to Fig. 1, is d = 9 ± 2 cm. This value is close to the values of d obtained by other researchers (Perelygin et al., 1975) for this meteorite.

Fig. 4. Fragment of a micrograph of the surface of an olivine crystal (pallasite Marjalahti) with a high gradient of track density. The image size is 284 × 226 μm.

In the overwhelming majority of the crystals studied, a practically uniform distribution of tracks is observed, without any noticeable gradient (within ± 20% of the density). In this connection, a sample with a very high gradient of track density (crystal M-L-11-10) is of particular interest. The small surface area of this crystal with a high track density is shown in **Fig. 4.** On the surface of the crystal two adjacent areas (1 and 2) of 200×800 μm sizes each were allocated, the track density on distance of 800 μm varies by two orders of value: from $3 \cdot 10^6$ up to $4 \cdot 10^4$

cm^{-2}. For each region over the entire length with a step of 20 μm the track densities were calculated. The results are shown in **Fig. 5**.

Both received distributions are characterized by the presence of a line part in the interval of values l = 0.017÷0.051 cm, where l is the distance from the edge of the area with a high track density. Data in this interval were approximated by regression lines of the form $\rho = a + bl$.

On the basis of this linear dependence, the gradients for both distributions were obtained by the formula (2). The average track density gradient, calculated with the use of all data approximated by the linear dependence of ρ on l, was amounted to ~ $5 \cdot 10^3$ % cm^{-1} for both areas.

To verify the data obtained, in the same sample M-L-11-10 after removing the surface layer of the crystal with located on it the etched tracks and subsequent etching, the track densities were repeatedly measured (see the insert in Fig. 5). The resulting average value of the track density gradient practically did not change and was ~ $4 \cdot 10^3$ % cm^{-1}. From the obtained dependence of the tracks formation rate versus the depth of the crystal (Fig. 3) we can assume that this crystal was irradiated not only by high-energy GCR (this contribution to the gradient is negligible) but also by cosmic rays with a high fraction of low-energy nuclei (particles of solar cosmic rays, nuclei of solar flares) at the thickness of the shielding layer no more than a few hundred microns.

In addition to the M-L-11-10 crystal, two more olivine crystals (M-L-20-8 and M-L-21-1) were found with a clearly expressed density gradient of the cosmic ray VH-nuclei tracks. The average values of the track density gradient for these two crystals were found to be ~ $3 \cdot 10^3$ and ~ $5 \cdot 10^3$ % cm^{-1}, respectively. These values are comparable with those for the crystal M-L-11-10 that indicates on the irradiation of the surface of these crystals also under the conditions of low shielding.

It should be noted that the crystals with a track density gradient that are often found in stony meteorites (achondrites, carbonaceous meteorites, ordinary chondrites of low petrological types) carry in them the tracks of pre-accretionary irradiation and preserved at low temperatures both during the formation of the parent bodies of these meteorites, and also during the subsequent space history. For pallasites such scenario is unacceptable because of the high temperatures. The substance of meteorites of this class was at the very high temperatures during the formation of a mixture of olivine and liquid metal in the parent bodies.

In the case of the Marjalahti pallasite the following scenario of its space history can be proposed. Shortly before falling to the Earth (~ n10^6 years) the meteorite was destroyed in space after a collision. As a result the surface of olivine matter with ML-11-10, ML-20-8 and ML-21-1 crystals became open and was further irradiated in the space before the entering across the Earth's atmosphere. A stabilized flight through the earth's atmosphere of a cone-shaped fragment (Kolesnikov et al., 1977) and/or the specificity of the pre-atmospheric meteoritic surface (with caverns and cavities) helped

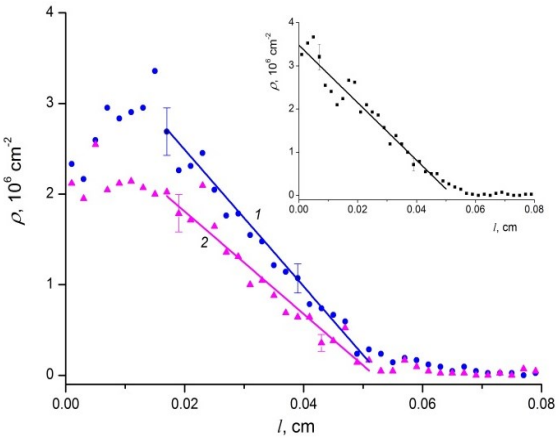

Fig. 5. The track density ρ on the surface of the crystal M-L-11-10 in depending on the distance l from the edge of the high-density region for two adjacent areas of 200×800 μm^2 (circles and triangles). 1 and 2 are the regression lines for linear parts. Insert is the same relationship after the surface of the crystal with etched tracks was crumbled and re-etched.

to preserve the exposed olivine surface and made it possible to detect ML-11-10, ML-20-8 and ML-21-1 crystals with a high gradient of track density.

The following fact proves the truth of the proposed hypothesis. As was noted above, the overwhelming majority of Marjalahti olivine crystals has the track density corresponding to the depth d = 9 ± 2 cm. However, about 10 % of the crystals have the track density comparable to the minimum value of ρ ~10^4 cm^{-2} in the ML-11-10, ML-20-8 and ML-21-1 crystals. These crystals (with the low values of ρ) were close to the center of the pre-atmospheric body before it destroyed into fragments and these crystals could be near the newly formed surface with an shielding layer thickness of less than ~ 500 μm. As a result the high density gradient of the tracks could be formed.

The value of information obtained with the ML-11-10, ML-20-8 and ML-21-1 crystals, among other things, is that all tracks were obtained in the etching process under identical conditions, which excludes the influence of uncertainties onto the obtained results.

Conclusion. The track formation rates of the cosmic ray VH-nuclei in olivine crystals versus depth in the pallasites of the different pre-atmospheric sizes are calculated. The obtained dependences were used to analyze the data on the track density in olivine

crystals from the Marjalahti pallasite. In three crystals the distribution of tracks with a high density gradient was found, which suggests a complicated exposure history of the meteorite.

The work was partially supported by the Program No. 28 of the Presidium of the RAS.

References:

Aaloe A.O. et al. (1979) On the preatmospheric sizes of the Yamyshev pallasite // Communications of the Joint Institute of Nuclear Research. Dubna. P14 – 12937 (*in Russian*).

Alexeev V.A. (2004) Meteorite Ablation Evaluated from the Data on the Density of Cosmic-Ray Tracks // Solar System Research. Vol. 38. No. 3. P. 194–202.

Bagulya A.V. et al. (2013) Search for superheavy elements in galactic cosmic rays // JETP lett. Vol. 97. No. 12. P. 811-824.

Bhattacharya S.K., Goswami J.N., Lal D. (1973) Semiempirical rates of formation of cosmic ray tracks in spherical objects exposed in space: pre- and post-atmospheric depth profiles // J. Geophys. Res. Vol. 78. No. 34. P. 8356-8363.

Goswami J.N., Lal D., Wllkening L. (1984) Gas-rich meteorites: Probes for particle environment and dynamical processes in the inner solar system // Space Science Reviews. Vol. 37. P. 111-159.

Herzog G.F. et al. (2015) Cosmic-ray exposure ages of pallasites // Meteoritics Planet. Sci. Vol. 50. No. 1. P. 86–111.

Kolesnikov E.M. et al. (1977) On the determination of preatmospheric size of the Marjalahti pallasite // Meteoritika. Vol. 36. P. 82-86 (*in Russian*).

Perelygin V.P., Viik Sh.B., Otgonsuren O. (1975) On determination of preatmospheric dimensions of Marjalahti meteorite // Communications of the Joint Institute of Nuclear Research. Dubna. P13 – 8359 (*in Russian*).

Badyukov D.D.[1], Bezaeva N.S.[2] Experimental shock metamorphism of the Chinga iron meteorite.

[1]V.I. Vernadsky Institute of Geochemistry and Analytical Chemistry RAS, Moscow, [2]Institute of applied physics of Ural Federal University, Ekaterinburg. (badyukov@geokhi.ru)

Abstract. A sphere made from the iron meteorite Chinga was shocked by a shock wave converging to its center. Calculated peak pressures at the edge and at the center of the sphere were 40 and > 200 GPa, respectively. Three zones of progressive shock metamorphism are distinguished that are characterized by the degrees of shock effect development. The main observed shock features are shear bands and associated with them metal shock melt veins. We suggest that the metal veins were formed by melting due to intense plastic deformation.

Keywords: *iron meteorites, shock metamorphism, shock experiments, Chinga, melting, shear bands, shock veins*

Introduction. Shock recovery experiments on rocks and minerals are used for laboratory simulation of shock metamorphism like identification of its diagnostic criteria, studying of changes in physical and physic-chemical characteristics of matters (so called diaplectic transformations), synthesis of high-pressure phases, development of shock stage schemes, and constructing "shock barometers". However, practically all investigations on this direction used as targets silicates and, more rarely, other compounds that are widely distributed in the Earth and Moon crusts and meteorites. Fe-Ni metal is a rock-forming mineral in meteorites; whole asteroids consist of the metal or it constitutes a main part of some asteroids. Numerous works have been considered shock-induced transformation in iron or different steels. However, it is wonder that there are a few works on meteorite metal (the authors know only two studies). For this reason we studied a sample of the Chinga iron meteorite that was loaded by a converging spherical shock wave. For the shock experiment the Chinga meteorite was chosen due to its homogeneous structure with lack of large mineral inclusions, and a relative large number of available samples. In this work we pay the attention to macro- and micro-deformations of the metal mainly.

Shock experiment and methods. The experiment was performed using Chinga sample # 108-15435 from the Meteorite collection of RAS (V.I. Vernadsky Institute). The sample was covered by regmaglypts that indicate the sample belongs to individual fragments decelerated in the atmosphere but not to meteorite shrapnel fragments formed by an impact on the ground. The sphere with the radius of 56 mm and the density of 7.92 g/cm^3 was made from the sample. This meteorite specimen was putted into a spherical stainless steel container The last was enveloped by a spherical high explosive layer that was detonated simultaneously on its outer surface. Initiated by this way a converging shock wave propagated inward the sample to its center. After focusing of the shock wave in the center a second

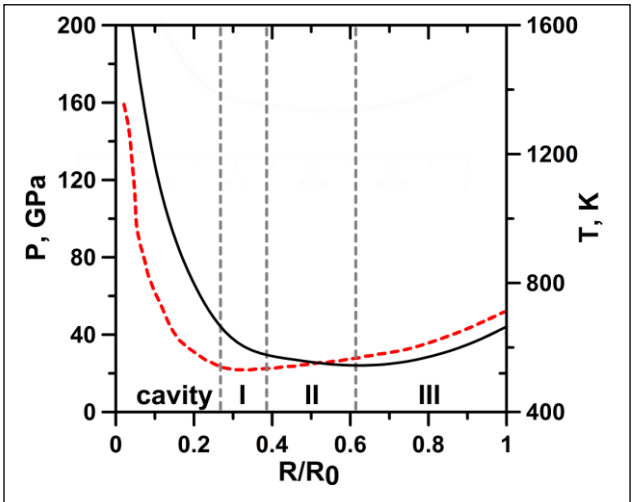

Fig. 1. Profiles of peak pressure (solid line) and temperature (dashed line) distributions along the reduced radius of the meteorite sphere.

compression wave came outward accompanied by material flow from the focusing area. Details wave propagation patterns can be found in (Kozlov, Zhukov, 1994) and (Kozlov, Petrovtsev, 2015).

The profile of pressure – temperature distribution along the sphere radius (Fig. 1) was produced using calculations of Kozlov and Zhukov (1994) for pure iron by the assumption of a minor difference between shock compressibility of iron and the Chinga metal. The profile is characterized by the sharp rise of P and T at an ~ 8 mm distance from the sphere center. Peak pressure can reach 200 GPa or, may be, higher in the focusing area that was a few mm in size. The sphere was retrieved from an outer steel container and sectioned through its center. A slab along an equatorial section with thickness of 4 mm was made. A part of the slab was polished and etched in 3% nital (HNO_3 solution in ethanol) for optical and SEM studies. For the study we used an optical petrographic microscope Leica and scanning electron microscopes coupled with an X-ray energy dispersive spectrometer used for determination of mineral compositions. Bulk compositions of areas of interest (usually 200 – 300 μm^2) were produced by their scanning. The accuracy of concentration measurements of Fe and Ni is 4 rel.%.

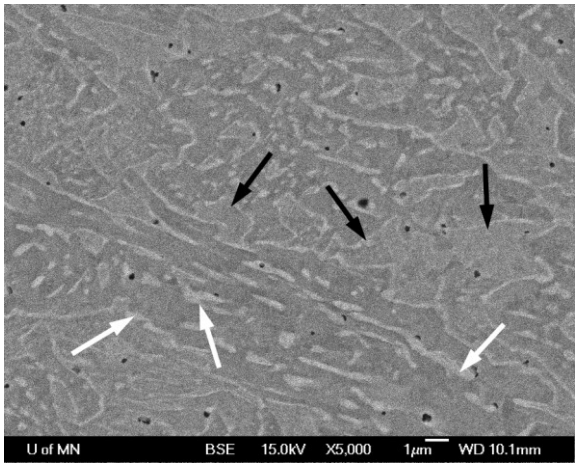

Fig 2. BSE image of Chinga duplex plessite matrix in the unshocked material. Taenite rods (light grey, marked by white arrows) is present as strips or worm-like precipitates in kamacite (dark grey). Areas (marked by black arrows) possible richer in Ni relative to kamacite are bordered by taenite precipitates. Black dots are defects of polishing.

Original material. The ungrouped Ni-rich Chinga iron meteorite belongs to ataxites. In the polished slide prepared from the sample we observed rare inclusions of kamacite and schreibersite in a plessite matrix. The duplex plessite matrix consists of fine-grained intergrowth of kamacite and taenite (Fig. 2). Taenite rods form worm-like or stripped tiny precipitates in kamacite (Fig. 2). The taenite precipitates have some preferred orientation. Also there are areas seem to be richer in Ni relative to kamacite (Fig. 2), the areas are delineated by taenite. Small sizes of kamacite and taenite grains prevent from accurate measuring of their chemical composition. Average Ni and Co contents in the plessite and are 15.7 wt% and 0.9 wt%, respectively. Rare spindle-like inclusions of kamacite (6.5 – 7.0 wt. % Ni) of 40 – 100 μm in length and 10 – 20 μm in width are bordered by taenite with 16 - 20 wt. % of Ni. There are very rare separate large euhedral crystals of schreibersite 0.5 - 1.5 mm in size. Besides these phases daubreelite - troilite intergrowths and natural Cu have been observed in other Chinga samples too. (Tertichnaya, Semenenko, 1995).

Shock effects. After the experiment the sphere had ~ 57 mm in diameter. The central part of the sample contained a 20 mm in size central cavity of a roughly spherical shape. The cavity has the ragged surface due to formation of numerous metal bulges of irregular shapes. One can suggest that the cavity formed due to spallation of the metal in a spherical rarefaction wave diverging outward from a point of a shock wave focus (a center of a sample) (Kozlov and Petrovtsev. 2015).

Three zones of shock deformation can be distinguished: 1 – zone of cracks, intense plastic deformation, textureless taenite veins , and cracks; 2 – zone of intense development of shear bands; 3 – zone of the separate shear bands and one metal vein (Fig. 1 and Fig. 3). The zone boundaries are not sharp and their positions were determined with the accuracy of ± 1 mm. The 3 – 4 mm wide zone 1 is adjacent to the central cavity and its outer border is 18 mm from the sphere edge. It is characterized by

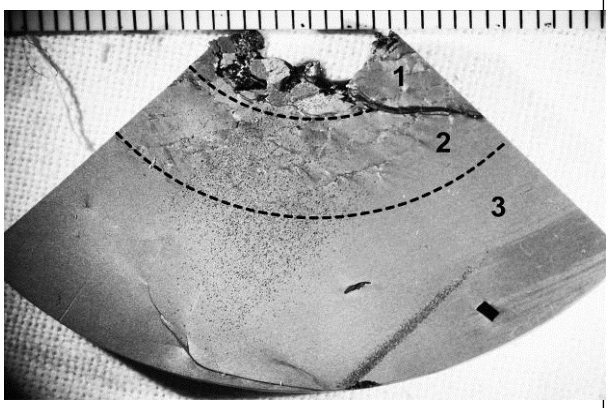

Fig. 3. Polished and etched section of the shocked Chinga meteorite sphere. Three zones of different stages of shock deformations are marked according to intensities of the deformations (see text). Zone 3 contains one taenite vein that is a curved thin line at a bottom of the image. The black rectangle at the bottom on the right side is a shreibersite crystal. Streak and diffuse bands at the right side of zone 3 and dots at the image center are defects of sectioning and polishing. Division value of the ruler is 1 mm.

intense plastic deformations, veins of taenite, and open cracks. The plastic deformation are present as i) narrow curved shear bands ~ 10 - ~100 μm in thickness and ii) relative large areas of disturbance of the intact duplex plessite texture contacting with shear bands. Some of the large plastic deformation areas have a vortex structure. Regions between the shear bands seem to retain their intact texture. Shear bands often accommodate the taenite veins located at their axial lines. These veins are texturally homogeneous and have sharp boundaries with the kamacite – taenite host matrix (Fig. 4). Their thickness varies from 150 to 5 μм. Some of the veins along their spreading are thinning and degrade to shear bands (Fig. 4) whereas other are interrupted at open spaces and voids. The open cracks are developed mostly along the shear bands and associated with them the textureless taenite veins, that are bordered edges of the cracks. Metal of the tanite veins is slightly heterogeneous and its Ni content is 13.2 – 17.5 wt% what roughly corresponds to an average Ni content in the plessite matrix.

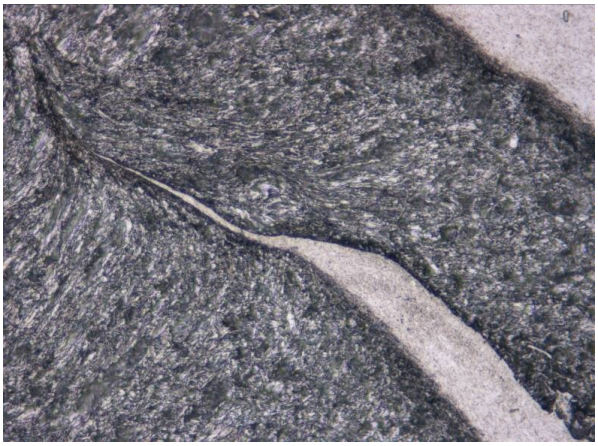

Fig. 4. Microphotography of of an area of zone 1, reflected light. Shear band accommodates a taenite vein (from down right to upper left), the last is thinning and wedging out. Etched in nital. Field of view is 0.22 mm.

The 6 mm wide second zone (from ~18 mm to ~11 mm from the sphere edge) is characterized by shear bands (Fig. 5) sometimes with thin taenite veins. The bands are slightly curved and dissect main mass of the sample on regions of a few mm in size. The regions have an undisturbed duplex plessite texture.

The 11 mm wide third area contains only very rare separate shear bands accommodate sometimes thin taenite melt veins <3 μm in thickness. The thickest (~ 30 μm) melt vein starts to develop from the same edge of the sample and is thinned approximate toward the sample center. The structure of the main mass is the same as the one of the precursor matter.

Discussion. The kamacite has the body centered structure or the structure of α-iron and is transformed diffusionless to the more dense hexagonal close-packed ε-phase at shock pressures >13 GPa. The transition is reversible and in a rarefaction wave the ε-phase is transformed back to the α-phase. The resulting structure is distorted and appears hatched in large kamacite crystals or recrystallized in steels (Buchwald, 1975). According to the pressure developed in the sample (Fig. 1) all kamacite grains had to experience the reversible transition. However, we did not observe any traces of the α-phase - ε-phase - α-phase transition in the kamacite grains using optical microscopy and SEM. We suppose that the lack of visible traces is due to small sizes of the kamacite grains (< 3 μм) and other methods (e.g. TEM) can show the distortion.

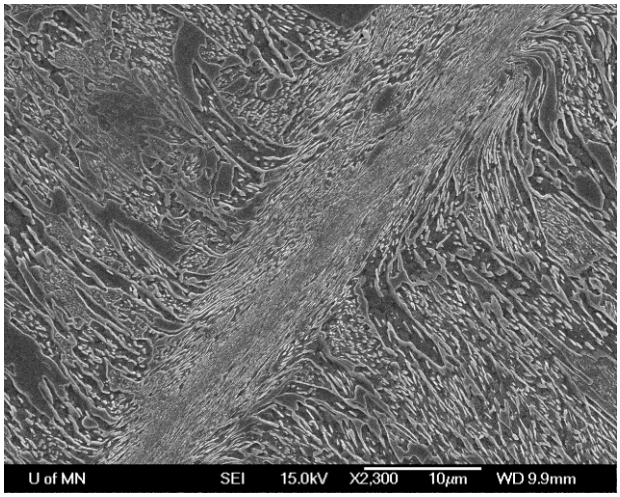

Fig. 5. SE image of shear band, zone 2. Slide surface etched in nital

Sharp boundaries of the taenite veins with the host kamacite – taenite matrix, homogeneity of their texture and structure as well as the compositions close to a bulk compositions of Chinga meteorite metal are evidences of their formation due to melting and following quenching of the melt. The observed absence of melting traces on a surface of the inner cavity denotes that "equilibrium" bulk melting due to high post-shock temperatures did not occur. Further, the calculated shock temperatures (Fig. 1) that are always higher post-shock temperatures are not enough for metal melting even at normal pressure. Thus, the taenite veins con not be formed by impregnation of the "equilibrium" melt into open cracks. Taking into account locations of the taenite veins along central axe lines of the shear bands we suggest that high rate plastic flow in the shear bands resulted in very high local temperature and melting of central parts of the shear bands. Very fast quenching with formation of the homogeneous metal was due to heat exchange with the relatively cold

host matrix. For this case we can estimate the initial temperature of the melt in ~ 2500ºC. Formation of shock melt veins containing high-pressure phases in chondrites and martian meteorites occurs by this mechanism (Sharp, DeCarli, 2006). It is possible that formation of shock melt zones in the iron meteorite Elga is connected with local high rate plastic deformations (Khisina et al., 2017).

Acknowledgments. D. Badyukov was supported partly by project 28 of Presidium RAS.

References:

Khisina N.R., Badyukov D.D., Wirth R. (2016) Microtexture, nanomineralogy, and local chemistry of cryptocrystalline cosmic spherules. *Geochemistry International* **54(**1), 68–77

Buchwald, V. F. Handbook of iron meteorites: Their history, distribution, composition, and structure. V.1. 1975, Arizona: State University, Center for Meteorite Studies, and Berkeley: University of California Press, 243 p.

Kozlov E. A., and Zhukov A. V. (1994) Phase Transitions in Spherical Stress Waves. Proceedings. High Pressure Science and Technology-1993. The American Institute of Physics Conference Proceedings 309: 977-980, doi:10.1063/1.46497

Kozlov E. A. and Petrovtsev A. V. (2015) Cumulation of a spherically converging shock wave in metals and its dependence on elastic-plastic properties, phase transitions, spall and shear fractures. International Journal of Modeling, Simulation, and Scientific Computing, Vol. 6, No. 1 (2015), 1550001(13 pages)

Sharp T.G., DeCarli P. (2006) Shock effects in meteorites. In: Meteorites and the Early Solar System II, Lauretta D. S. and McSween Jr. H. Y. Eds., University of Arizona Press, Tucson, Arizona, , P. 653-677

Tertichnaya B. V.; Semenenko V. P. (1996) The Mineralogy of the Ancient Ataxite Chinga (IVB-Anom) Meteoritics & Planetary Science, vol. 31, page A141

Barenbaum A.A. Complexing the data of astronomy, geology and meteoritics at development of the adequate spiral model of Galaxy.

Oil and Gas Research Institute RAS, Moscow
(azary@mail.ru)

Abstract. It is shown that adequate spiral Galaxy model can be constructed only based of astronomical observations in combination with geology and meteoritics data. This model is dynamic ones. According to this model the Galaxy spiral structure are simultaneously formed by two interacting systems of branches, one with a logarithmic one, and other with an Archimedean type of spirals. At that if four logarithmic arms can be identified based on astronomy data, then two Archimedean jet streams are established exclusively based on geology data. To solve this task, the theoretical model of Sun's motion in Galaxy is used, uniquely linking main events in geological history of Earth and Solar System with Galaxy influence at moments then Sun intersected jet streams and galactic arms. The constructed model of Galaxy proved its adequacy in solving a number of key problems of geology, meteoritics and astronomy.

***Keywords**: Dynamic model of Galaxy spirality, Geological time scale of Phanerozoic and Precambrian.*

Introduction. The study of the structure of spiral galaxies is a very difficult task (Vorontsov-Velyaminov, 1978). First of all, it is caused by a large variety of galaxies, a lack of understanding of their physical nature, as well as low accuracy and resolving power of astronomical methods. Especially great difficulties arise in the study of the spiral structure of our Galaxy. Due to the location of the Sun in the galactic plane, where large amounts of light absorbing dust are concentrated, this task is still far from the solution (Melnik, 2011). The difficulties are so great that even the question of how many and which spiral sleeves are in our Galaxy has, is open for the time being. For a long time it was believed that our Galaxy has two logarithmic sleeves (Marochnik, Suchkov, 1984). Today it is established (Vallee, 2016) that it has four logarithmic sleeves. At the same time, there are evidences of two more branches in the Galaxy (Efremov, 2005), which do not coincide with the universally accepted ones.

The situation with the Sun distance to the Galaxy's center RO is no better. In the last half-century, its magnitude has been repeatedly reviewed, varying within the range of R_o = 6.5÷10.5 kpc. In 1985, the General Assembly of IAU officially recommends R_o = 8.4 kpc. However, later R_O returned to value of 7.1 kpc, and now is adopted 8.5 kpc. The situation with remoteness of Sun from Galaxy center is complicated so much that a number of authors, while exploring different objects, in parallel use two different scales of distances: “short” with R_o = 7.5 kpc and “long” with R_o = 8.5 kpc (Zabolotskikh et al., 2002).

New approach to the problem. This approach to the solution of problems of astronomy and geology has been developing by the author for the last 25 years after the discovery of an astrophysical phenomenon – the jet flow of gas-dust matter from the spiral galaxies center (Barenbaum, 2002). As result of the discovery of this phenomenon, it turned out that spiral galaxies along with the usual logarithmic arms have a system of jet streams twisted in the Archimedes spiral. In particular our Galaxy has four identical arms and two jet streams. At this the presence of jet streams has been established thanks to the author's development of a dynamic model that revealed a close connection of the phenomena on the Earth and in the Solar system with cosmic processes in the Galaxy. According to this model, when the Sun is moving along its galactic orbit, it quasiperiodically intersects the jet streams and spiral arms of the Galaxy, and at such times the Earth and other planets are subjected to powerful cosmic influences. This fact allows us to study the spiral structure and physical processes in the Galaxy

from geological data, as well as solve the urgent problems of geology, using the results of astronomical observations (Barenbaum, 2010).

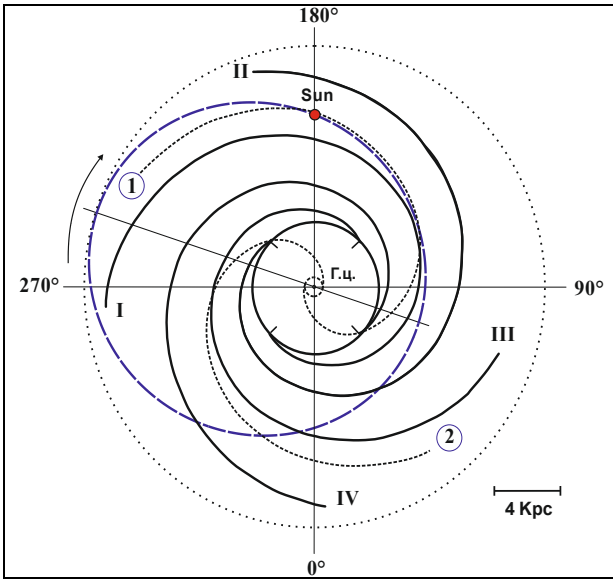

Figure 1. The current Sun position in the galactic orbit (ellipse) with respect to the four logarithmic arms of Galaxy (Roman numerals) and to the two Archimedean jet streams (Arabic numerals in circles) in the projection onto galactic plane. The solar orbit is shown for the last Sun turnover around the Galaxy center (G.c.). The dashed circle in center denotes nuclear gas-dust disk, from which two jet streams expiry radially into diametrically opposite sides. Circle of radius R_o = 3.9 kpc, where galactic arms begin, determines size of Galaxy's isothermal core. Outer dotted ring characterizes the Galaxy's corotation radius. Arrow indicates direction of the Sun's motion along the orbit, which coincides with Galaxy rotation and rotation of line of the apsides (straight line) of solar orbit.

Dynamic model. In Figure 1 shows the spiral design of the Galaxy proposed by author and the orbit of Sun's motion in the Galaxy, which best satisfy astronomical observations and geological data as of beginning of 1990s, when this model was actively developed.

In this model, the Galaxy has four logarithmic arms, which described by to the formula $R(\varphi) = R_o \{\alpha[\varphi+(2k-1)\pi/4]\}$, where: k = 1 – 4 is arm number; R_o = 3.9 kpc is radius of the Galaxy's isothermal core; α = 0.202 rad^{-1} is parameter characterizing the angle swirling of arms of 78°. System of arms rotates uniformly around the Galaxy center with period T_φ = 222.23 million years.

There are also 2 jet streams described by equation of Archimedean spiral $R(\varphi) = V_s \cdot (t + \varphi/\omega_d) = V_s \cdot t + \rho\varphi$, where V_s = 300 km/s is expiration velocity of gas-dust matter from nuclear disk; t is the time; ω_d is angular velocity of disk rotation corresponding to its rotation period T_d = 50 million years; $\rho = V_s/\omega_d$ = 2.5 kpc/rad is a parameter characterizing the degree of twist of jet streams. Jet streams expiry from two diametrically opposite points of nuclear disk. Nuclear disk is inclined to the plane of logarithmic arms at an angle of 20° (Space Physics, 1976) and probably precesses with a period close to the rotation period.

The value $R = \alpha/\rho$ determines the so-called corotation radius of the Galaxy, at which, according to our dynamic model, the radii of curvature of logarithmic arms and jet streams are the same. This parameter can be independently established according to astronomy and geology data (Barenbaum, 2010), which allows using it to verify the adequacy of the constructed spiral model of the Galaxy.

Figure 1 also shows the calculated Sun orbit in the Galaxy. The orbit is an ellipse with an eccentricity of 0.36 and a major semi axis of 10.17 kpc, which slowly rotates in the galactic plane in the direction of the Sun's motion with an angular velocity of $3.14 \cdot 10^{-9}$ years $^{-1}$. The Sun rotation period around the Galaxy center in this orbit is 250 million years. At the same time the Sun performs vertical oscillations with respect to galactic plane with a period of ~ 50 million years and amplitude of 10 pc (Barenbaum, 2002).

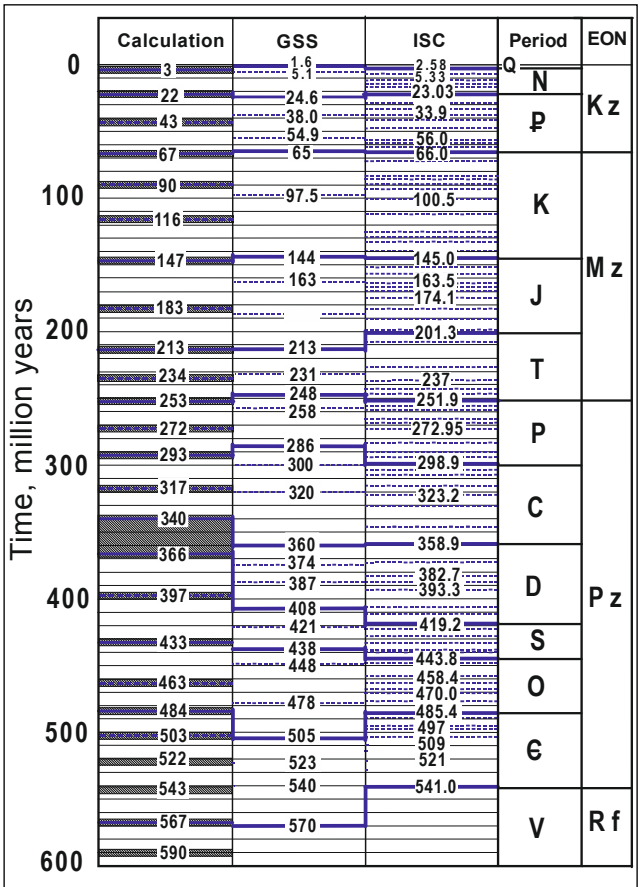

Table 1: The age of Phanerozoic scale boundaries

Due to the different rotation speeds of nuclear disk and galactic arms, as well as the Sun's motion along galactic orbit, their mutual position changes with time. At that the Sun quasi-periodically intersects the spiral arms and jet streams of the Galaxy, and at this periods of duration ~2 ÷ 5 million years the Earth and other planets, according to the geological data are subjected to powerful bombardments by galactic comets (Barenbaum, 2010). These events in the Earth's geological history are marked as epochs of global natural catastrophes: biotic, climatic and tectonomagmatic. At present, their times are reliably fixed by geologists as the boundaries of stratons of the Phanerozoic geochronological scale.

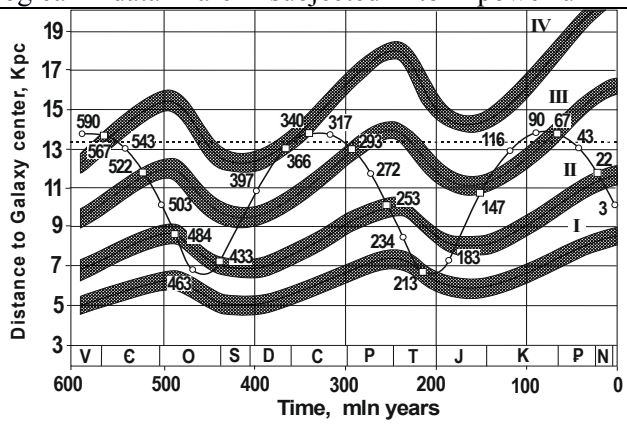

Figure 2. The Sun removal of galactic center and four Galaxy arms for the last 600 million years. Roman numerals are arm number; sinusoidal curve is the Sun's orbit; circles and squares on the orbit are the moments of Sun intersection of jet streams and star formation regions in galactic arms, respectively. The dashed line shows magnitude of Galaxy's corotation radius. Below are the boundaries of periods of Phanerozoic geochronological scale (Khain, 1978)

In Figure 2, the calculated times of galactic impacts are compared with the empirically established boundaries of periods and departments of the Phanerozoic scale.

The model allows us to calculate the times of these boundaries, as well as to reveal the physical principle of constructing the Phanerozoic scale itself (Barenbaum et al., 2002). It is shown that the boundaries of scale departments are explained to the times of Sun finding in jet streams, the boundaries of periods – in the regions of star forming of galactic arms, and boundaries of the eras (Paleozoic, Mesozoic and Cenozoic) – in the same zones, but at a distance of the corotation radius from Galaxy center, where processes of star formation in galactic arms are most intense (Marochnik, Suchkov, 1984).

Discussion of dynamic model. We note a number of consequences of our model that are important for solving, at least, two problems of the Earth's geological history. The first consequence relates to the Phanerozoic, and the second – to the earlier period of Earth and Solar System development.

In Table 1 the calculated times of borders of stratons in the Phanerozoic Time Scale (Barenbaum et al. 2002) are compared with the age of borders of Systems and Series in latest version of the General Stratigraphic Scale (GSS) adopted in Russia (Zhamoyda, 2015) as well as with borders of Ages (Stages) in the International Chronostratigraphic Shart (ISC) (www.stratigraphy.org).

The thick lines denote boundaries of the Periods (Systems), and the dashed lines indicate bounders of the Ages (Stages). In Column 1, the calculation of boundaries of the Epochs is marked separately with dashed lines, and the possible range of errors in our calculation is shown by hatching.

From Table 1 it can be clearly seen that the absolute age of same borders of both scales does not always coincide. This discrepancy of times is a major unsolved problem of stratigraphy. Its consideration is beyond the scope of this article. We only note that according to our model, the main reason for the discrepancies is that many events caused by Sun hits into jet streams are fixed in the GSS as the Sections boundaries, whereas in the ISC this is not.

The table also discovered a significant deviation of the calculation results from geology data for Devonian (D) and Carbon (C). It is significant that in this time interval the Sun was on the corotation radius and moved along arm IV (see Fig. 2). Difference between calculation results and actual data can be explained as by an inaccurate specification of parameters of the arms and/or the Sun's orbit, or due to changes in trajectory of the Sun when moving along galactic arms (Space Physics, 1976). The second assumption seems to us more correct.

In this regard, it should be noted that in development of the dynamic model the author has been assumed that due to the Galaxy evolution the parameters of galactic branches and the Sun orbits vary with time. Moreover these changes can be notice from geology data (Barenbaum, 1991, 2004). However, later at the analysis of meteoritic data, a conclusion was drawn (Barenbaum, 2015) that during the time of the Solar system existence neither the Galaxy nor the Sun's orbit in it practically changed.

In this regard, it should be noted that in development of the dynamic model the author has been assumed that due to the Galaxy evolution the parameters of galactic branches and the Sun orbits vary with time. Moreover these changes can be

notice from geology data (Barenbaum, 1991, 2004). However, later at the analysis of meteoritic data, a conclusion was drawn (Barenbaum, 2015) that during time of the Solar system existence neither Galaxy nor Sun's orbit in it practically changed. This conclusion was made on the grounds that the times of main events in the Earth and Solar system history of discover a peculiar regularity (Fig. 3).

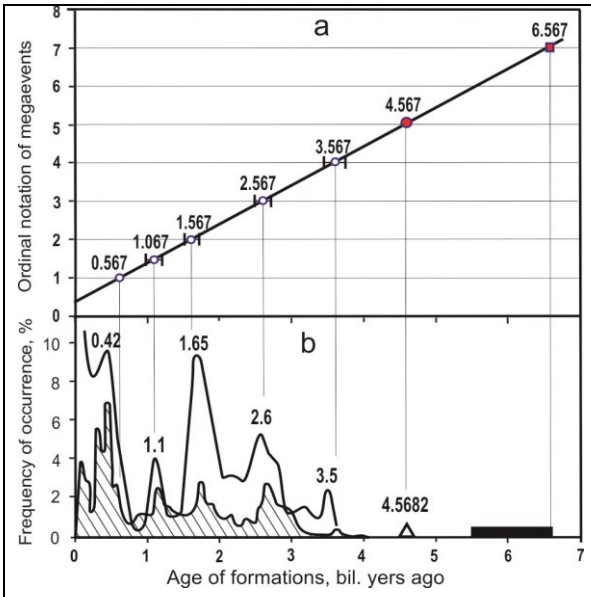

Figure 3: a) Mega-events in Earth history that define boundaries of Precambrian Geochronological scale (Plumb, 1991):
0.567 billion years ago – beginning of Phanerozoic;
1.1 billion years ago – boundary of Neoproterozoic ;
1.6 billion years ago – boundary of Mesoproterozoic;
2.6 billion years ago – boundary of Proterozoic;
3.1 billion years ago – boundary of Mesoarchean;
3.6 billion years ago – boundary of Archean.
Mega-events under numbers 5 and 7 refer to both Earth and Solar system as a whole.

b) Evidence supporting Fig. 3a: Curve is the intensity of the processes of magmatism and ore formation (shaded) in Earth history (Pushkarev, 1990); triangle is generally accepted time of Solar system formation (Wikipedia); parallelepiped is age of iron meteorites FeII, which are 0.9-2 billion years older than meteorites of all other types (Sobotovich, 1974)

This pattern is that the four most significant historical events: the boundaries of Phanerozoic and Proterozoic and the two main cycles of the Solar system formation (Barenbaum, 2002) are following each other with an interval of 2 billion years. The same period is observed for two paired events of "lesser geological significance". This are the borders of Mesoproterozoic and Archean, as well as of Neo-proterozoic and Mesoarchean.

The fact is that in our dynamic model the cycle lasting 2.0 billion years exactly corresponds to 8 full revolutions of the Sun in orbit and 9 full revolutions of the Galaxy itself. Therefore, all these mega-events consistently happen in different galactic arms, but at identical distance from Galaxy center. This distance corresponds to the corotation radius of Galaxy (Fig. 1 and 2).

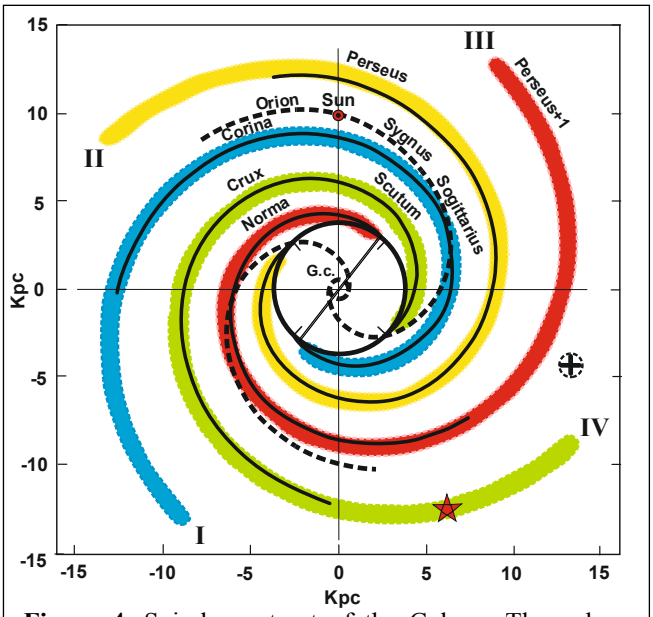

Figure 4. Spiral construct of the Galaxy. The color shows the different logarithmic arms established in the Galaxy by J. Valle (2016)

In Figure 4 the locations of galactic arms are compared in our model and in the model of astronomers (Valle, 2016). The distance of the Sun from the Galaxy center in astronomical model is taken to be equal to RO = 10 kpc, as in our calculation. The oblique line in the center of Fig. 4 shows the position of the galactic bar. The bar in our model is the line of intersection of nuclear disk plane and galactic plane, which in our Galaxy form an angle ≈ 20°. In the disk plane the jet stream closest to the Sun, well known as the spiral branch of Orion – Cygnus also is located. The presence of Orion – Cygnus branch the model (Valle, 2016) does not take into account.

We see that the spiral design of galactic arms is almost identical in both models. In our model, the arms system rotates uniformly around the center with a period T_φ = 222.23 million years. The Sun also rotates and after 8 full revolutions along galactic orbit the Sun hits to the same point on the corotation radius in each arm where it was 2 billion years ago.

The place in arm IV, where Solar system has been formed is shown by an asterisk. The cross in a coterie in Fig. 4 denotes the projection of this point onto galactic plane at the time of this event.

Despite a formal similarity the different Galaxy arms are not quite the same. The most significant events associated with the two epochs of Solar system formation, as well as at borders of

Proterozoic (2.567 billion years ago) and Phanerozoic (567 million years ago), occurred in the arm IV. Less significant events occurred at the borders of Archean (3.567 billion years ago) and Mesoproterozoic (1.567 billion years ago) in the arm II, and events of even less significance at the borders of Mesoarchean (3.067 billion years ago) and Neoproterozoic (1.067 billion years ago) in the arm III. While in hand I, according to geological data, there was not a single mega-event in Precambrian.

Conclusions. The results of this article indicate that the construction of an adequate spiral model of the Galaxy requires compulsory integration of the results of astronomical observations with data from geology and meteoritics. Such integration allows:

- discover existence in Galaxy of two previously unknown jet streams;
- clarify Sun's distance to Galaxy center, and also determine the Galaxy rotation speed;
- prove that Galaxy structure and its rotation speed have not changed since of the Solar system formation;
- to establish that logarithmic arms in our Galaxy are not identical. The main events in history of the Solar system associated with the Sun and planets formation occurred in the arm IV (Crux-Scutum) whereas events of less geological significance in arm II (Perseus) and arm III (Norma).

References:

Barenbaum A.A. Megacyclicity of geological processes and evolution of the Galaxy. *Tsikly prirodnykh protsessov, opasnykh yavleniy i ekologicheskogo prognozirovaniya*. Moscow. Publishing House of Russian Academy of Natural Sciences. 1991. Issue. 1. P.27-47.

Barenbaum A.A. *Galaxy, Solar system, Earth. Subordinated Processes and Evolution*. Moscow. Publishing House: GEOS. 2002. 393 p.

Barenbaum A.A., Gladenkov Yu.B., Yasamanov N.A. Geochronological scales and astronomical time. *Stratigrafiya. Geologicheskaya korrelyatsiya*. 2002. V.10. №2. P. 3-14.

Barenbaum A.A. The reason for the "biotic revolution" in Vendian-Cambrian from the standpoint of cometary-galactic hypothesis. *Doklady Akademii nauk*. 2004. T.398. №4. P. 513-515.

Barenbaum A.A. *Galactocentric Paradigm in Geology and Astronomy*. Moscow. Publishing House: LIBROKOM. 2010. 546 p.

Barenbaum A.A. Position of Sun in Galaxy in the epoch of Phaethon's destruction. Conference Proceedings *"Shestnadtsataya mezhdunarodnaya konferentsiya «Fiziko-khimicheskiye i petrofizicheskiye issledovaniya v naukakh o Zemle"*. Moscow: IGEM RAS, 2015. P. 39-42.

Vorontsov-Velyaminov B.A. *Extragalactic Astronomy*. Moscow. Publishing House: Nauka, 1978. 480 p.

Zabolotskikh M.V., Rastorguev A.S., Dombis A.K. Kinematic parameters of the young subsystems and the rotation curve of the Galaxy. *Pis'ma v Astronomicheskiy zhurnal*. 2002. V.28. №7. P. 516-528.

Yefremov Yu.N. Zvezdnyye ostrova. Fryazino. Publishing House: «Vek-2». 2005. 272 p.

Marochnik L.S., Suchkov A.A. *Galaktika*. Moscow. Publishing House: Nauka, 1984. 392 p.

Melnik A.M. *Kinematics of external pseudo-rings and spiral structure of the Galaxy*. Dis. Doktor fiziko-matematicheskikh nauk, GAISH. Moscow. 2011. 164 p.

Pushkarev Yu.D. *Megatsikly v Evolyutsii Sistemy Kora – Mantiya*. Leningrad. Publishing House: Nauka. 1990. 217 p.

Sobotovich E.V. *Izotopnaya Kosmokhimiya*. Moscow. Publishing House: Atomizdat, 1974. 208 p.

Space Physics. Little encyclopedia. Ed. by S.B. Pikel'ner. Moscow: Publishing House «Sov. Encyclopedia». 1976. (in Russian)

Khain V.Ye. (red.) *Geokhronologicheskaya Tablitsa*. Leningrad. Publishing House: VSEGEI. 1978.

Plumb K.A. New Precambrian time scale. *Episodes*. 1991. V.14. №2. P.139-140.

Valle J.P. A guided map to the spiral arms in the galactic disk of the Milky Way https://arxiv.org/ftp/arxiv/papers/1711/1711.05228.pdf.

Bezmen N.I.[1], Gorbachev P.N.[1], Zinov'eva N.G.[2] Experimental modeling of the chondritic structure.

[1]Institute of Experimental Mineralogy RAS, Chernogolovka Moscow district (bezmen@iem.ac.ru),
[2] M.V. Lomonosov Moscow State University, Department of Geology, Moscow

Abstract. The chondritic structure was experimentally obtained with the example of forsterite meteorites, which formed as a result of the interaction of oxides mixture and gas components at 1250°C and a pressure of 50 MPa. The starting composition of the runs corresponded cosmic abundance of the elements. The composition of the fluid phase (C-O-H-S system) was controlled by three independent parameters: mole fraction of hydrogen, the presence of atomic carbon (crucible with the initial sample), and the fugacity of sulfur in equilibrium of the sulphide melt with iron. The composition of the fluid phase at 1250 °C and 50 MPa was calculated using a special program. The presence of hydrogen in the melts leads to the rupture of Si-O-Si bridging bonds in the silicon-oxygen anions, with a part of silicon in fluid-saturated melts become a state of modifiers which cause the formation of glasses as the forsterite composition chondrules during quenching.

Keywords: *Experiment, meteorites, cosmic abundance, chondritic structure, red-ox conditions.*

Introduction. The chondrites form a compact group of meteorites in which MgO, SiO_2 and Fe (±FeO) play an equally important role, while the remaining elements belong to secondary or impurities. According to the composition of petrogenic elements, they approach the composition of the Sun, i.e. to cosmic abundance. With the exception of carbonaceous chondrites, there are no fluid components in them, the presence of which during their formation is fixed in minerals in the form of gas inclusions. Structurally, the chondrites consist of glassy chondrules placed in a finely granular matrix. They are divided into equilibrium and nonequilibrium chondrites by the ratio of glass and crystals. Chondrules are depleted in iron, nickel,

carbon and differ from the total composition of chondrites and correspond to the achondrites chemistry. A fragment of the diagram Mg- (Si + Al) - (Fe + Ni) with a comparison of the compositions of chondrites of various types is shown on the figure:

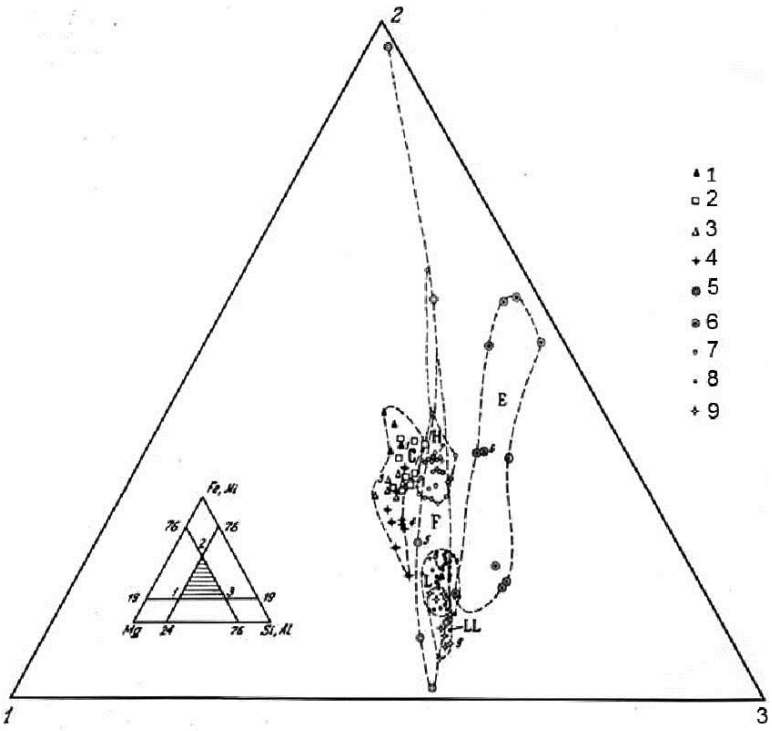

1-4 - carbonaceous: 1-C1, 2-C2, 3-C3 (O), ornans type, 4-C3 (V), vigarana type; 5 - F (forsterite); 6 - E (enstatite); 7-9 - ordinary, 7 - H, 8 - L, 9 -LL.

Experimental method. A hydrogen cell for a high-pressure gas vessel was developed on basis of the "Shaw membrane" technique use. It consists of W or Re reactor in the high temperature zone and in the cold zone from the equalizer-separator which separates the internal volume of the cell (120 cm^3) from the external pressure of the argon medium. W and Re do not react with hydrogen and are not permeable to hydrogen. The cell was placed in a vessel of high gas pressure (diameter 50 mm, volume 1.5 l) with internal heating. The mole fraction of hydrogen in the fluid phase was controlled by Ar-H_2 mixtures of purity-specific gases in the hydrogen cell. The experimental procedure is based on the permeability of H_2 through the welded Pt capsule, which was used as a container for the sample.

Argon-hydrogen mixtures, X_{H2} = 0.6, were prepared in a special device, and then were pumped into the reactor at a total pressure of 10.1 MPa. The hydrogen cell was inserted into the heater into a gradientless temperature zone. The temperature gradient was controlled by two independent windings of the heater and determined by two thermocouples placed in a reactor near the reaction capsule. The gradient did not exceed 0.1°C / cm. The thermocouples were calibrated for the melting point of pure gold the accuracy of the temperature determination was ± 5°C. The pressure was measured with an accuracy of ± 5 MPa by a Bourdon manometer. The experiments were quenched by switching off the power supply.

The contents of gases in the H-C-O-S system were controlled by carbon and Fe-FeS association, which always present in meteorites. We used the coupling reactions between gases of different compositions, calculated on the assumption of an ideal mixture of real gases (the Lewis-Rendall rule): X_{H2} = 0.6, X_{H2O} = 0.005, X_{CO2} = 0.0, X_{CO} = 0.011, X_{CH4} = 0.391, X_{H2S} = 0.003, $\log f_{O2}$ = -15.32, $\log f_{S2}$ = -5.6.

The starting sample corresponding to the cosmic abundances of the elements was prepared from oxides of petrogenic elements, metallic Fe and Ni, sulfur, the amount of carbon was introduced in the form of oxalic acid. The water content corresponded to the calculated oxygen content obtained after weakening its cosmic abundance in the charged oxides. The experiments were held for 168 hours. After the experiment the sample was a column of glass without a noticeable reaction with the graphite crucible, from which polished section was prepared for subsequent analysis on the microprobe.

Results of the experiments.

Physico-chemical parameters of formation of chondrites.

Temperature regime of formation of chondrites. Chondrules contain glass or would be crystallized completely. Crystallization temperatures of the chondrules vary considerably. They can be higher than the temperature of incongruent melting of enstatite (1300-1400°C).

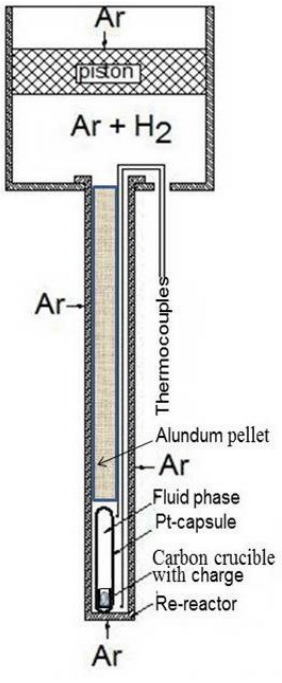

There is a reason to believe that the chondrules crystallized before the matrix. The matrix is enriched in iron and sulfur. On the basic of an experimental study of the distribution of Ni between Fe-metal and troilite depending on the temperature (Bezmen et al., 1979) it was found that the minimum temperatures of this association for all

chondrites are located near 500°C - 800°C. The results reflect a complex temperature history of differentiation, crystallization and subsequent cooling of the chonrites, during dissipation of fluid components occurred.

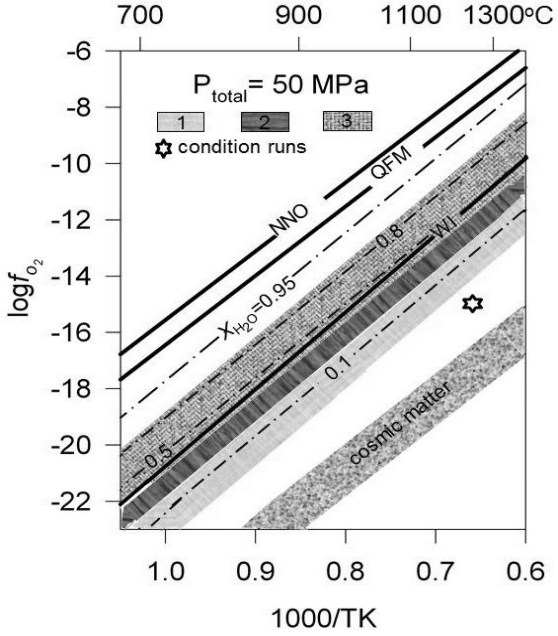

Oxidation-reduction conditions for the formation of chondrites. The diagram shows the oxidation-reduction conditions for the formation of chondrites of various types: 1- ordinary chondrites, 2 - carbonaceous chondrites and achondrites, 3- forsterite and enstatite chondrites.

Pressure. Petrological data based on the absence of formed at high pressures minerals show that the crystallization of chondrites took place at low pressures below 500 MPa.

Chondritic structure of meteorites. In previous works (Bezmen et al., 2005; 2011), which based on the analysis of photoelectron spectra of hydrogen-containing aluminosilicate glasses, it was shown that the presence of hydrogen in the melts leads to the rupture of Si-O-Si bridging bonds in the silicon-oxygen anions and the replacement of some oxygen atoms by hydrogen ions the following scheme:

$$- Si\text{-}O\text{-}Si + H = Si\text{-}O + Si\text{-}H,$$

with a part of silicon in fluid-saturated melts becomed a state of modifiers which cause the formation of glasses as the forsterite composition chondrules during quenching. Clear interphase boundaries between the chondrules and the matrix indicate the liquid immisibility nature of their relationship.

A fragment of the sample obtained as a result of modeling the chondrite structure at a pressure of 50 MPa and 1250°C in *X*-ray radiation of Kα-Mg, Kα-Si, Kα-Fe (20kV, 20nA) is shown on the figure. The mapping was performed over an area of 200x200 μm^2 with an accumulation time of 100 s.

The physicochemical conditions for the formation of a chondritic structure would arise as a result of the ordinary accretion of cosmic matter in the form of segregations of melts enriched with petrogenic and fluid components, which placed in a predominantly hydrogen-methan gas medium in the early stages of protosun formation, as well as accretion in the planetesimals and in the planets of the protosolar system.

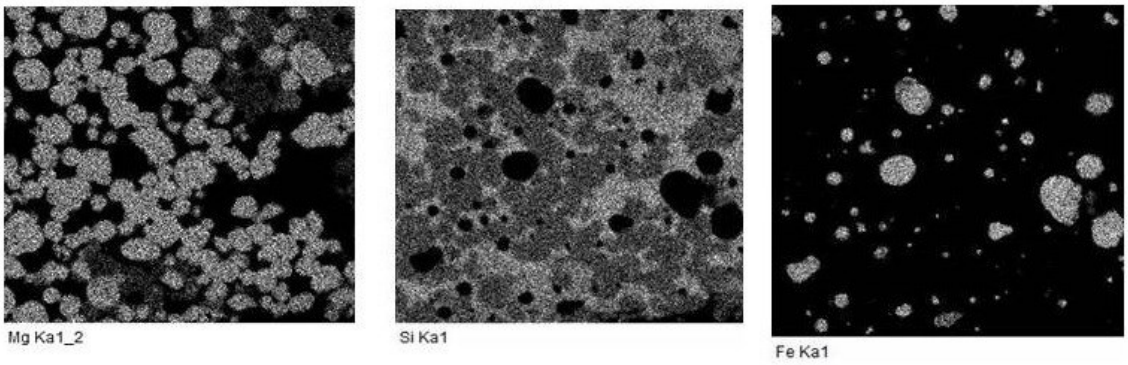

References:

Bezmen N.I., Lu'tov V.S., Osadchij E.G. (1979) Distribution of Ni between troilite and metallic iron as mineralogical thermometer // Geochem. Internat. V. 16. No 3. P. 3-12

Bezmen N.I., Zharikov V.A, Zavelsky V.O, Kalinichev A.G. (2005) Melting of alkali aluminosilicate systems under hydrogen-water fluid pressure (Ptotal = 2 kbar). Petrology 13(5): 407-426

Bezmen N.I., Zavelsky V.O., Salova T.P. (2011) Solubility water-hydrogen fluid in gaplogranite, albite and sodium disilicate melts, depending on the hydrogen content in the fluid phase and ^{1}H NMR study ($P_{total.}$ = 200 MPa). Petrology 19(2): 185-199. DOI: 10.1134/S0869591111020044

Demidova S.I.[1], Badekha K.A.[1], Kononkova N.N.[1] Modelling of P-bearing fayalite crystallization conditions in lunar mare basalts. UDC 551.14:554.015.4

[1]V.I. Vernadsky Institute of Geochemistry and Analytical Chemistry RAS, Moscow, Russia (demidova.si@yandex.ru, *ksenia_uimina@mail.ru*, *nnzond@geokhi.ru*)

Abstract. Rare grains of P-bearing fayalite (< 0.4 wt % P_2O_5) has been recently found in late-stage mesostasis of olivine basaltic fragment in Dhofar 287 lunar meteorite, in Fe-rich rock fragment of Luna-16 soil sample and in two

fragments of Luna-24 olivine basalts. Fayalite is a common late-stage product of mare basalt crystallization. Equilibrium and fractional melt crystallization modeling of Dhofar 287A and Luna-16 low-Ti (LT) basalts and Luna-24 very low-Ti (VLT) basalts were performed using the modified version of METEOMOD program (Ariskin et al., 1997). It was established that equilibrium crystallization of LT and VLT basalts may not produce late-stage fayalites while residual melt can contain up to 2-3 wt.% P_2O_5. Meanwhile fayalite may be produced under fractional crystallization of low-Ti and very low-Ti basalts at 985-1040ºC from a melt containing up to 1-2 wt % of P_2O_5. Model calculations suggest that fayalite quantity in LT and VLT basalts should not be significant in this case.

Keywords: *lunar rocks, lunar meteorites, phosphorus-bearing olivine.*

Rare grains of P-bearing olivine (< 0.5 wt.% P_2O_5) have been recently found in a list of lunar samples and meteorites. It is presented as Mg-rich and Fe-rich varieties - fayalites. The recent is a common late-stage product of mare basalt crystallization (see e.g. Papike et al., 1991). Modelling of crystallization processes for lunar basaltic magmas will enable us to estimate the conditions of fayalite formation and set some restrictions for the parent melt composition.

Samples and methods. Standard optical microscopy methods were used for detailed observation of polished thin and thick sections of Dhofar 287 lunar mare meteorite and some fragments of Luna-16 and Luna-24 regolith. The chemical composition of mineral phases was determined using Cameca SX-100 (Vernadsky Institute, Moscow, University of Vienna) and SX-FIVE (University of Vienna) and JEOL JXA-8530F (Natural History museum, Vienna) microprobe at an accelerating voltage of 15 kV and a beam current of 10 nA.

Computer simulation of equilibrium and fractional crystallization of bulk compositions of Dho 287A olivine basalt and some mare basalts of Luna-16 and Luna-24 was carried out through the modified version of METEOMOD program (Ariskin et al, 1997). This program was specially calibrated relatively to the experimental data on crystallization of mare-basalt melts (see e.g. Demidova et al., 2003). Crystallization modeling was carried out at an oxygen fugacity (fO2) buffer equivalent to iron-wüstite (IW) and 1 atm pressure.

Results. P-bearing fayalite (Fo_{2-4}) was revealed in the late-stage mesostasis of Dhofar 287 lunar mare meteorite and in the fragment of Luna-16 Fe-rich rock and in two fragments of Luna-24 olivine basalts (Fig. 1).

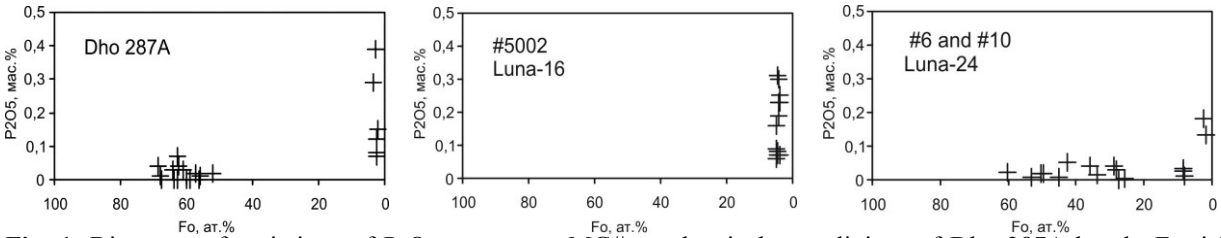

Fig. 1. Diagrams of variations of P_2O_5 content vs MG# number in lunar olivines of Dho 287A basalt, Fe-rich rock fragment #5002 of Luna-16 sample and fragments #6 and #10 of Luna-24 olivine dolerites.

Dhofar 287 meteorite consists of two parts: main meteorite mass (95%) is represented by a low-Ti (LT) basalt (Dho 287A), with the attached small portion of a regolith breccia (Dho 287B). Dho 287A is a coarse-grained olivine-ilmenite basalt, that contains olivine (1-2 mm) (Fo_{44-72}) and pyroxene (up to 0.5 mm) ($En_{2-56}Wo_{7-42}$) phenocrysts in a fine-grained plagioclase-pyroxene matrix with an ophitic structure. This fragment is significantly enriched with late-stage mesostasis (>3%), that mostly consists of fayalite (Fo_{0-14}), Si,K-rich glass with rare fluorapatite and merrillite grains. The accessory phases are ilmenite, spinel group minerals, troilite, Fe-Ni metal (Anand et al., 2003).

The fragment #5002 of 1639 Luna-16 sample has a coarse subophitic structure and a Fe-rich composition. Fayalite Fo_{4-5} (<0.31 wt.% P_2O_5), silica phase and Ca-Fe pyroxene En_2Wo_{35} fill the interstices between the large lath-shaped plagioclase crystals An_{87-93}. Round inclusions of inhomogeneous K-Si-glass (from 5 to 20 μm in size) present in fayalite. Fe-Ni metal, troilite, ilmenite, apatite and K-Si glass occur in accessory quantities.

Two fragments of Luna-24 rocks (#6 and #10) have a VLT basaltic composition (the size from 400x900 to 450x950 mkm). They are presented by olivine dolerites and have ophitic structure. Plagioclase is represented by anorthite An_{90-96}. Pyroxene significantly varies in composition $En_{7-47}Wo_{9-36}$. Single olivine phenocrysts are zoned and vary in composition from Fo_{60} to Fo_2, fayalite contains 0.13-0.18 wt.% P_2O_5, whereas Mg-rich areas do not contain phosphorus in the detectable quantities. Silica, troilite and armalcolite present as accessory minerals.

Discussion. Olivine is a common liquidus phase of mare basalts. Fe-rich olivine along with Ca-Fe-pyroxene and silica is a product of late stage crystallization of mare basalts (e.g., Papike et al., 1991). Recent experimental work suggests that the distribution coefficient of P in olivine can significantly increase while the melt is being fractionated, that leads to a compatible behavior of P in olivine (Grant, Kohn, 2013). This, apparently, explains the presence of P-bearing fayalites on the edges of olivine phenocrysts in Luna-24 dolerites and in the late-stage mesostasis of Dho 287A mare basalt. A Fe-rich mineral association similar to that observed in fragment #5002 of Luna-16 is a late-

stage product of mare basalt crystallization. It is important to note that Mg-rich olivines of mare basalts do not contain phosphorus above detection limits (Fig. 1).

Only the composition of Dho 287A meteorite fragment is known among the studied basalt fragments (Anand et al., 2003). As shown earlier, the meteorite may represent the composition of the primary melt (Demidova et al., 2003). Dho 287A meteorite is enriched with incompatible elements, P_2O_5 content is 0.21 wt.%. The studied rock fragments with P-bearing fayalite of Luna-16 and -24 have inequigranular structure and their composition cannot be reliably determined, therefore the known compositions of typical basalts of this region are used in the modeling of equilibrium and fractional crystallization (Table 1). P_2O_5 content in Luna-16 basalts is 0.13-0.15 wt.%, and in Luna-24 basalts is 0.02-0.04 wt.%.

The order of mineral appearance at the equilibrium crystallization of Dho 287A olivine basalt is the following: olivine ⇒ olivine + plagioclase ⇒ olivine + plagioclase + pigeonite ⇒ olivine + plagioclase + pigeonite + augite + ilmenite (Fig. 2a). Similarly, olivine crystallizes first in some melts of Luna-24 VLT basalts, pigeonite and plagioclase crystallize later or almost simultaneously with olivine, followed by augite, and ilmenite appears at the later stages of crystallization, which is comparable to the previously obtained model calculations for the Mare Crisium lunar samples (Ariskin et al., 1990). On the contrary, if equilibrium crystallization of more Al- and Ti-rich basalts of Luna-16 takes place plagioclase crystallizes first, followed by either olivine or ilmenite and pigeonite.

Table 1. Bulk composition of Dho 287A and Luna-16 and-24 mare basalts

	Dho 287A	Luna-16 basalts						Luna-24 basalts					
		1	6	8	10	13	15	6	10	11	12	18	21
SiO_2	43.2	43.8	43.0	46.3	46.3	43.2	45.6	45.0	43.9	45.3	46.6	44.3	44.2
TiO_2	2.76	4.90	5.50	1.02	2.16	4.80	3.50	1.44	0.74	1.16	0.86	0.09	0.62
Al_2O_3	8.35	13.7	13.9	20.2	19.3	14.3	14.2	6.2	19.0	12.4	12.9	11.6	7.7
Cr_2O_3	0.65	0.28	0.26	н.а.	н.а.	н.а.	н.а.	0.56	н.а.	н.а.	н.а.	н.а.	н.а.
FeO	22.1	19.4	20.2	11.1	12.9	16.4	17.3	19.0	16.6	20.3	17.4	20.5	21.6
MnO	0.29	0.20	0.20	0.17	0.20	0.27	0.25	0.25	0.19	0.27	0.20	0.30	0.43
MgO	13.2	7.05	6.05	2.32	3.80	4.90	5.20	16.9	5.20	7.50	6.3	7.6	18.2
CaO	8.74	10.4	10.8	14.8	15.0	13.4	13.3	7.9	14.0	12.2	13.3	12.7	7.0
Na_2O	0.53	0.33	0.23	0.83	0.52	0.47	0.34	0.02	0.50	0.37	0.31	0.36	0.15
K_2O	0.19	0.15	0.16	0.44	0.19	0.21	0.24	0.07	0.06	0.03	0.04	0.04	0.05
P_2O_5	0.21	0.15	0.14	0.23	0.05	0.06	0.11	0.02	0.11	0.02	0.04	0.05	0.03

Dho 287A (Anand et al., 2003); Luna-16: 1,6 – (Vinogradov et all., 1974); 8,10,13,15 – (Kurat et al., 1976); Luna-24: 10, 11 – (Barsukov et all., 1980); 6, 12, 18, – (Ryder et al., 1978); 21 – (Taylor, 1978)

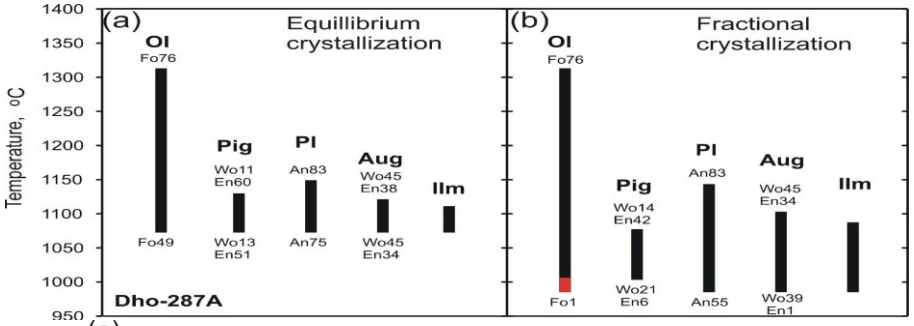

Fig. 2. Results of equilibrium (a) and fractional (b) crystallization modeling of Dho 287A bulk composition (Table 1), using the modified METEOMOD program of Ariskin et al. (1997)

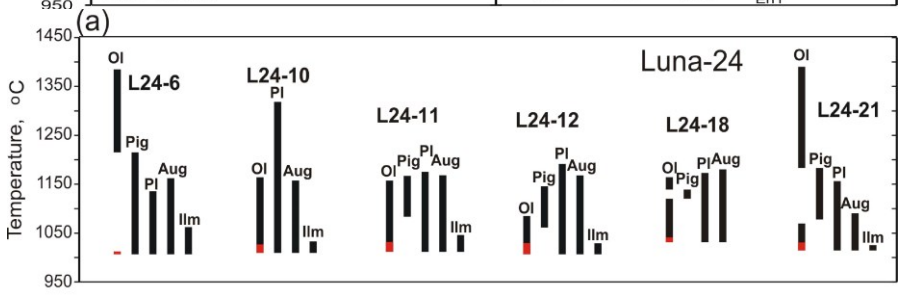

Fig. 3. Results of fractional crystallization modeling of some Luna-24 (a) and Luna-16 (b) basalts bulk compositions (Table 1), using the modified METEOMOD program of Ariskin et al. (1997)

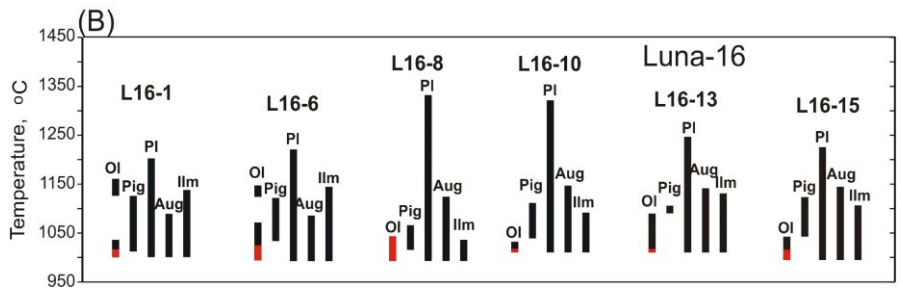

Computer simulation of crystallization of Dho 287A basalt and some Luna-16 and -24 basalts enables us to find out that the equilibrium crystallization does not lead to the formation of

fayalite, at least until 95% of the melt has crystallized. However, earlier modeling of the equilibrium crystallization of mare basalts showed that in some cases, for example, during the crystallization of 15065 Apollo-15 sample and single samples of Luna-24 alumina basalts (Ariskin et al., 1990), late olivine may appear on liquidus repeatedly (after reactive substitution by pigeonite) at the temperatures ~1100°C and ~1140°C, respectively. However, the above-mentioned authors point out that real relations between phases in the low-temperature equilibrium of the melt with the olivine-pigeonite-augite association are not sufficiently studied experimentally and are difficult to model (Ariskin et al., 1990). It should be noted that this model does not take into account the possibility of apatite or merrillite crystallization and suggests that residual melt accumulates phosphorus during crystallization. P_2O_5 content reaches 2-3 wt.% in the late stages. In fact, phosphates are present as late-stage phases in mare basalts (e.g., Papike et al., 1991). They are thought to be crystallized after 95% of the melt solidification (McCubbin et al., 2010).

Fractional crystallization of VLT Luna-24 basalts produces pigeonite (and/or augite), plagioclase, when olivine disappears from the sequence (Fig. 3a). When fractional crystallization of high alumina basalts of Luna-16 takes place, plagioclase that crystallizes first is followed by olivine that disappears from the sequence at the onset of pigeonite and augite (Fig. 3b). Another possibility is realized when olivine occurs after crystallization of pyroxenes and at the end of crystallization it is represented by fayalite (Fig. 3b). Fe-rich olivine occurs on the liquidus when 79-85% of the melt has already crystallized. For Luna-16 basalts it starts to crystallize at the temperature of 1000-1040°C, and ends at 990-1020°C, the residual melt contains 0.3-1.6 wt.% P_2O_5. In Luna-24 basalts fayalite occurs at the temperature of 1030-1050°C, and its crystallization ends at 1010-1030°C, herewith the residual melt contains 0.1-0.5 rarely up to 1.3 wt.% P_2O_5.

Fractional crystallization of Dho 287A also leads to the formation of fayalite in the late stage of crystallization. The fayalite appears at 1012°C, when 81% of the melt has crystallized, and ends at 985°C when 88% of the melt has been solidified (Fig. 2b). The residual melt contains 1.0-1.8 wt.% P_2O_5. The phosphorus distribution coefficient between olivine and the melt was calculated on the basis of real olivine compositions and the corresponding model melt compositions. The phosphorus distribution coefficient was 0.1-0.3, that is higher than the equilibrium value (<0.1).

Conclusion. Computer modelling of crystallization sequence of the melt composition of Dho 287A and LT basalts of Luna-16 and VLT basalts of Luna-24 enabled us to find out that the equilibrium crystallization does not lead to the formation of fayalite, although on the late stage P_2O_5 content in the melt can reach 2-3 wt.%, while fractional crystallization on the late stage truly leads to the formation of fayalite. Corresponding residual melt may contain up to 1-2 wt.% P_2O_5. The crystallization temperature of fayalite is from 985 to 1040ºC. However, model calculations demonstrate that the fayalite content in the LT and VLT basalts should not exceed 1%, and likely significantly less.

The work was supported by RFBR grant №16-05-00695.

References:

Anand M., Taylor L.A., Misra K.C. et al. KREEPy lunar meteorite Dhofar 287A: A new lunar mare basalt // Meteorit. Planet. Sci. 2003. V. 38. P. 485-499.

Ariskin A.A., Barmina G.S., Frenkel M.Ya Thermodinamic modeling of lunar basaltic melt crystallization // Geochemistry international. 1990. №10. P. 1476-1485.

Ariskin A.A., Petaev M.I., Borisov A.A., Barmina G.S. METEOMOD: A numerical model for the calculation of melting-crystallization relationships in meteoritic igneous systems // Meteorit. Planet. Sci. 1997. V. 32. P. 123–133.

Barsukov V.L., Dmitriev L.V., Tarasov L.S. et al. Geochemical and petrochemical peculiarities of regolith and lithic classts from Mare Crisium // In «Lunar soil from Mare Crisium». Moscow «Nauka». 1980. P. 158-166.

Grant T. B., Kohn S. C. Phosphorus partitioning between olivine and melt: An experimental study in the system Mg_2SiO_4-$Ca_2Al_2Si_2O_9$-$NaAlSi_3O_8$-$Mg_3(PO4)_2$ // Amer. Mineralogist. 2013. V. 98. P. 1860-1869.

Demidova S.I., Nazarov M.A., Anand M., Taylor L.A. Lunar regolith breccia Dhofar 287B: A record of lunar volcanism // Meteorit. Planet. Sci. 2003. V. 38. P. 501–514.

Kurat G., Kracher A., Keil K. et al. Composition and origin of Luna 16 aluminous mare basalts // Proc. 7th Lun. Sci. Conf. 1976. P. 1301-1321.

McCubbin F.M., Steele A., Hauri E.H. et al. Nominally hydrous magmatism on the Moon // Proc. Nation. Acad. Sci. USA. 2010. V. 107. 11223-8.

Papike J., Taylor L., Simon S. Lunar minerals. In Lunar sourcebook: A users guide to the Moon, edited by Heiken G. H. et al. 1991.Cambridge University Press. P. 121–182.

Ryder G., Marvin U. On the origin of Luna 24 basalts and soils // In Mare Crisium: The view from Luna 24, Pergamon Press (New York). 1978. P. 339-355.

Taylor G.J., Warner R.D., Wentworth S. et al. Luna 24 lithologies: Petrochemical relationships among lithic fragments, mineral fragments, and glasses. // In Mare Crisium: The view from Luna 24, Pergamon Press (New York). 1978. P. 303-320.

Vinogradov A.P., Chupakhin M.S., Shevaleevskiy I.D., Belyaev Yu.I. Chemical composition of the lunar regolith from Luna-16. // In «Lunar soil from Mare Fertility». Moscow «Nauka». 1974. P. 264-278.

Dorofeeva V.A., Devina O.A. Evaluation of the mass fraction of water ice in the rock-ice planetesimals for cosmochemical data. UDC 523.64

Vernadsky Institute of Geochemistry and Analytical Chemistry, *Moscow* dorofeeva@geokhi.ru

Abstract. The ratio of the mass of the refractory component and water ice (M_{dust}/M_{ice} H_2O) in the rock-ice planetesimals formed in the early Solar system is an important parameter in the construction of models of the internal structure of satellites of external planets, trans-Neptunian objects, comet nuclei and etc. It is also necessary when calculating the time of accumulation of cores of the giant planets and in the construction of models for the formation of their atmospheres. However, until now there is no certainty in the value of this parameter. This paper presents a numerical evaluation of possible intervals of values of Mdust/Mice primary rock-ice bodies as a function of the ratio of the molecules CO and CO2, as well as the percentage of carbon contained in the refractory organic compounds in the primary disc material (Nebula). The calculations are based on modern observational data and model estimates, the results are compared with the available literature data.

Keywords: *ice-rock planetesimals; comets; dust-to-ice mass ratio; comet nucleus; comet ices*

The ratio of the mass of the refractory component and water ice ($M_{dust}/M_{ice\ H2O}$) in the primary rock-iceplanetesimals that formed in the early Solar system and was the building material for all objects of the external Solar system is an important parameter in the construction of models of the internal structure of satellites of external planets, TRANS - Neptunian objects, comet nuclei, etc. The value of this parameter is also important at the calculation of the accumulation time of the giant planets nuclei and at the modeling of their atmospheres. However, until now it was not possible to determine definitely the numerical value of this parameter. Note also that it is necessary to distinguish between the $M_{dust}/M_{ice\ H2O}$ ratio, which is discussed in this paper, and the M_{dust}/M_{ice} ratio, which in the English literature corresponds to the concept of "dust-to-ice mass ratio". Water ice is not the only kind of ice in the composition of primary rock-ice bodies, although its share can reach ~ 80% of the total ice mass (Krankowsky et al., 1986), so $M_{dust}/M_{ice\ H2O}$ will always be more than M_{dust}/M_{ice}. Although M_{dust}/M_{ice} is often understood as $M_{dust}/M_{ice\ H2O}$, ignoring the presence of such ice as CO, CO_2, CH_4, NH_3, *etc*. (Lorek et al., 2016, *etc*.).

The total and component composition of the primary rock-ice planetesimalsis similar to the composition of comet nuclei. Comet nuclei hasthe maximum water ice content (Ewine et al., 2014)in comparison with other bodies in the Solar system. In addition they do not bear traces of any secondary processes which could significantly change their total composition from the moment of formation.

Several attempts have been made to determine the values of M_{dust}/M_{ice} and $M_{dust}/M_{ice\ H2O}$ in comet nuclei based on theoretical models as well as on experimental data on the composition of cometary gas and dust (gas-dust) comas, duringwhich were used as ground-based observations, and observations with spacecrafts (SC) were used. It should be noted thatthe observations of the intensity of gas sublimation from cometary nuclei can be correctly carried out both by devices installed on spacecrafts and under favorable conditions from the Earth, but the determination of the total mass of the dust component flow from the Earth is difficult due to the problems at observation oflarge (> 1 cm) particles.

One of the first models of the composition of cometary nuclei has been proposed (Whipple, 1950), so-called Dirty snowball model, according to which the comet nucleus is homogeneous in composition and has a mass ratio of ice and dust component is M_{dust}/M_{ice} = 1. This estimationis widespread and was further used in the construction of models of cometary nuclei (Tancredi et al., 1994; Kossacki et al., 1999; Cohen et al., 2003; de Sanctis et al., 2005; Lasue et al., 2008; Prialnik et al., 2008; Marboeuf, Schmitt, 2014, etc.). In addition, it did not contradict the tables of cosmic (solar) abundance, starting with the tables Camiron (1968), and up to the tables Lodders (2003), according to which, the mass of the Z-component (i.e., the mass of all elements except H and He) was ~ 2 mass % of the total mass of the preplanetary gas-dust disk (nebula). Besides, M_{dust}/M_{ice} = 1 coincided with results of radar observations of comets 2P/Encke and 26P/Grigg-Skjellerup, and later with the results of the space missions of VEGA and Giotto, which investigated Halley's comet (McDonnell et al.(1987). It should be noted that, for example, the fraction of water vapor in Halley's comet was ~ 80% (Eberhardt et al., 1986; Meier et al., 1994; Eberhardt et al., 1994), $M_{dust}/M_{ice\ H2O}$ value > 1 ~ 1.25. The composition of the dust component in these investigation was not discussed.

However, further corrections of the possible mass of large dust particles led to a revision of this estimate and to the conclusion that in the coma of Halley's comet M_{dust}/M_{ice} =2 (Green et al., 2004), and the upper limit has a value of 3 (McDonnell et al.(1991). Moreover, in the paper (Fulle et al., 2015) the authors believe that due to the inability to obtain a correct distribution of dust particle sizes from 1 g and above, it cannot be excluded that the M_{dust}/M_{ice} value for Halley's comet is even higher. This conclusion is consistent with the results of the work (Sykes, Walker, 1992), in which by combining data on the rate of loss of the dust component by the nuclei of eight short-period comets (Sykes, Walker, 1991) with data on their gas mass loss (Kresak, Kresak, 1987) it was possible to obtain an estimate of M_{dust}/M_{ice} in the range of 1 to 4.6, with an average

value of $M_{dust}/M_{ice} \approx 2.9$. It was concluded that the water ice content in cometary nuclei was close to 50% by volume and to ~ 25% by mass, i.e. by the composition of the comet nuclei is not a lump of dirty snow ("dirty snowball"), and a lump of frozen mud ("frozen mudballs"). The values of M_{dust}/M_{ice}which are significantly greater than 1 were also obtained in the analysis of the composition of the plume, caused by a blow to the nucleus of comet 9P/Tempel 1 during the Deep Impact experiment (Küppers et al., 2005).

The results of the study of thecomet 67P composition of the coma using of MIRO and ROSINA instruments installed on board the spacecraft Rosetta showed that the ratio of the dust and gas components in it is unstable and depends on the heliocentric distance of the comet, so the resulting value of M_{dust}/M_{ice} had a large range - from 2 to 6 with an average value of $M_{dust}/M_{ice} = 4\pm2$ (Rotundi et al., 2015). In the paper (Fulle et al., 2017) authors made even more radical assumption that for all TRANS-Neptunian objects, including the nuclei of comets, the relationship of the dust mass to the mass of the ice is ≈ 7.5, i.e. even lower than in CI chondrites, where it is up to 20 mass. % (Wiik, 1956).

It was also obtained some estimates of the value of M_{dust}/M_{ice} in the nuclei of comets by indirect way, on the basis of their physical characteristics. For example, (Lamy et al., 2015) the proportions of ice and dust in cometary nuclei were made estimations based on the magnitude of their dielectric permittivity which were determined by ground radars in the study of the properties of the nuclei of eight comets at the depth of the first few meters. The probability interval of permeability values (2-3.1) according to the model laboratory experiments carried out by the authors, the mass fraction of ice from 0.1 to 0.2, dust from 0.2 to 0.5 and the porosity interval from 35 to 75% is the best. In the paper (Lorek et al., 2016) M_{dust}/M_{ice} values were obtained by using theoretical and experimental modeling of the formation of cometary nuclei by the gravitational collapse of a cloud of rock-ice particles (pebble clouds) of characteristic size ~ 1 cm of different composition. It was found that in a wide range of changes in the values of the initial parameters of the model (cloud mass, porosity of the initial particles, etc.), cometary nuclei with the actually observed value of the average density (~ 0.5 g/cm^3) are formed if the M_{dust}/M_{ice} value in both the initial particles and in the formed comet nucleus is not less than 3, but higher values are possible, up to 9. Models of high-M_{dust}/M_{ice} cometary nuclei have also been considered in a number of other papers, for example (Fulle et al., 2016; Hu et al., 2017).

Such a large spread of estimates of M_{dust} / M_{ice} values in the comet nuclei could be explained by many factors, not least by their heterogeneity. As shown by the resent results obtained, the composition of comets, which are judged on the composition of the volatile components of comet nuclei, in particular for comets 8P/Tuttle, 9P/Tempel 1, 103P/Hartly and 67P/C-G, comet nuclei are heterogeneous in composition at characteristic sizes of ~ 100 m (Bonev et al., 2008; Feaga et al. 2007; A'hearn, 2011; Combi et al., 2012; Fougere et al., 2014; Marboeuf, Schmitt, 2014; Hassing et al., 2015; Luspay-Kuti et al., 2015; Hoang et al., 2017, etc.). It follows that it is hardly possible to obtain an unambiguous estimate of the value of M_{dust}/M_{ice} and M_{dust}/M_{iceH2O} as a result of direct measurements. Therefore, we considered it appropriate to obtain it basing on the experimental data on the composition of the dust and gas components of cometary nuclei, taking into account the data of the tables of cosmic abundance Lodders, 2010, in which, unlike all previous tables, the mass of Z-components is estimated at ~ 1%. It should be noted that the decrease in the mass of the Z-component was mainly due to a decrease in the relative abundance of C and O, while maintaining the values of the relative abundance of the main rock-forming elements almost unchanged. In our calculations, we proceeded from the generally accepted position that comet nuclei formed at ~ 25K in the TRANS-Neptunian region of the gas-dust near-solar protoplanetary disk, the elemental composition of which corresponds to the tables (Lodders, 2010).

The water content in the solar composition system is determined by the distribution of oxygen between its individual components: a refractory component that includes both mineral and organic fractions, water ice and ice more volatile compounds such as CO, CO_2, CH_3OH, *etc*.Consider these components in more detail.

The mineral component corresponds to the composition of interstellar dust and, according to most researchers, the abundance of rock-forming elements in it is close to the gross composition of CI-chondrites, and the main forms of their presence are iron sulfide, Mg-Fe-olivine and pyroxenes (Fulle et al., 2016).

Refractory organic component (CHON) and its mass fraction in comet dust. The composition of CHON in 1P/Halley was described by the formula $C_{100}H_{80}O_{20}N_4S_2$ (Fulle et al., 2016). The ratio of O/C in it=0.2, which is close to that in the insoluble organic matter (IOM - Insoluble organic matter) of Murchison O/C ≈ 0.2 meteorite, although its elemental composition is given in different works different: $C_{100}H_{70}O_{18}N_3S_3$ (Gardinier et al., 2000; Alexander et al., 2007); $C_{100}H_{155}O_{20}N_3S_3$ (Quirico-14). Since for us the most important value is the ratio in CHON O/C, we take its elemental composition corresponding to the formula $C_{100}H_{80}O_{20}N_4S_2$.

The mass fraction of CHON in the refractory component (M_{min}/M_{org}) can only be measured *in situ* and, to date, only two comets 1P/Halley and 67P/C–G. For 1P/Halley the ratio of elements $(C/Si)_{dust}$=4.4 ± 1.3 (Jessberger et al., 1988) has been determined

and the mass fraction of CHON in the dust component was estimated ≈ in 36 mas. %, and for 67P/C-G $(C/Si)_{dust} = 5.5^{+1.4}_{-1.2}$ and the mass fraction of CHON in the dust component is estimated in ≈45 mas. %.

Another source of information on the significance of $(C/Si)_{dust}$ in comets is dust, presumably of comet origin, and Arctic micrometeorites (UCAMMs), in which the carbon content is much higher than the usual content even in primitive meteorites, and its form is close to that in comets. In them, the carbon content can be from 26±6 to 58±14 mas. % (for more details see Wooden et al., 2018).

Given the uncertainty of the values of the ratios of the masses of mineral and organic component in comet dust (M_{min}/M_{org}), use a value $(C_{opr}/\Sigma C)_{dust}$ as a model parameter by varying it in the range from 0 to 0.7.

The ice component of comet nuclei. It is judged by the composition of comet comas; data on the content of maternal molecules for 15 comets of different dynamic types with respect to the mass of water were generalized in (Dorofeeva, 2016). Its bulk is water ice, but CO and CO_2 ice also have high abundance commensurate with the abundance of H_2O. The abundance of most other oxygen-containing compounds does not exceed 1 mass. %. Exceptions are methyl alcohol and formic aldehyde, the average relative content of which is ~ 1 mass. % and molecular oxygen O_2: in comas of two comets (Halley and 67P) its content was 3.7 and 3.8 mass. %, respectively (Rubin et al., 2015; Bieler et al., 2015). Given these data, due to the large spread of values of the relative contents of CO_2 and CO in comet comas, and the fact that the atomic ratio of these molecules $(n_{CO2}/n_{CO})_{neb}$ in the gas phase of nebula is unknown, we take it as a model parameter, varying it from 0.1 to 0.5.

The calculation results are shown in Fig.1, where the model estimate $M_{dust}/M_{ice\ H2O}$in the nuclei of comets and other TRANS-Neptunian objects that have not experienced significant evolution of gross composition postaccretion stage shown depending on $(n_{CO2}/n_{CO})_{neb}$ values $(C_{opr}/\Sigma C)_{dust}$.

The results presented in Fig. 1, allow us to draw the following conclusions.

1. Both parameters- $n_{CO2}/n_{CO}$and $C_{opr}/\Sigma C$ – significantly affect the value of $M_{dust}/M_{ice\ H2O}$.

2. The smaller is the C share in CHON, the more is M_{H2O} and the less is $M_{dust}/M_{ice\ H2O}$.

3. The available experimental data (are marked by a square in Fig. 1) best meet the following composition of the solids formed in the outer region of the nebula: $M_{dust}/M_{ice\ H2O} \approx 1.5 – 2$ in $n_{CO2}/n_{CO} = 0.2 – 0.3$, the ratio of the mass of mineral and organic components and $M_{min}:M_{org} = 60:40$ to 90:10.

With regard to the composition of cometary nuclei, the following can be said. Low relative values of the masses of CO and CO_2 observed, as a rule, to perihelion, giving high values of $M_{dust}/M_{ice\ H2O}$ in the comet coma. High relative value of the masses of co and CO_2 observed after perihelion, resulting in low $M_{dust}/M_{ice\ H2O}$. Perhaps this explains the observed the comet 67P such a high scatter of the values of $M_{dust}/M_{ice} = 4±2$ (Rotundi et al., 2015).

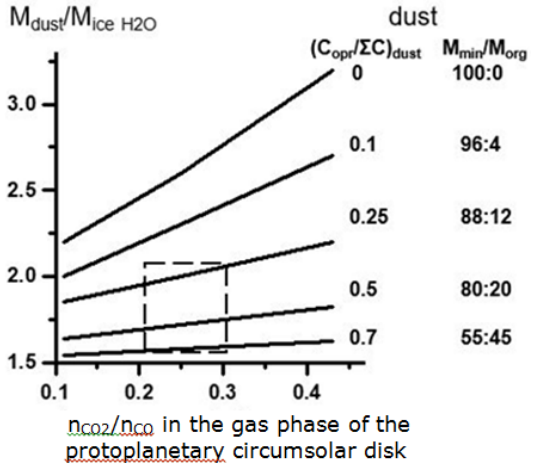

Fig.1. Estimation of the mass ratio of refractory components and ice of water in rock-ice bodies formed in the outer zone of the solar protoplanetary gas-dust disk. The square is the most probable intervals for changing the parameters

The work was partially supported by the Program № 28 of the RAS Presidium.

References:

Дорофеева В.А. Проблемы интерпретации экспериментальных данных по составу вещества комет // Труды ВЕСЭМПГ-2016. ISBN 978-5-88918-041-8.М., 2016.−С. 86-87.

A'Hearn, M. F. EPOXI at Comet Hartley 2/ M. F.A'Hearn [et al.]// Science. −2011.−Vol. 332, Issue 6036. −P. 1396-*1400.*

Bonev, B. P. The peculiar volatile composition of Comet 8P/Tuttle: A contact binary of chemically distinct cometesimals /B. P.Bonev [et al.] // Astrophys. J. −2008, −Vol. 680. − L61.

Feaga, L. M. Asymmetries in the distribution of H_2O and CO_2 in the inner coma of Comet 9P/Tempel 1 as observed by Deep Impact/ L. M.Feaga [et al.] // Icarus.−2007.−Vol.190. – P. 345-356.

Hoang, M.The heterogeneous coma of comet 67P/Churyumov-Gerasimenko as seen by ROSINA: H_2O, CO_2, and CO from September 2014 to February 2016/M.Hoang [et al.] // Astronomy & Astrophysics. −2017. −Vol. 600, id. A77.−13 p.

Lodders, K. Solar system abundances of the elements. In: Astrophysics and Space Science Proceedings. Berlin: Springer, 2010. − P. 379–417.

Rotundi, A. Dust measurements in the coma of comet 67P/Churyumov-Gerasimenko inbound to the Sun. /A.Rotundi [et al.] // Science.−2015, −Vol. 347, Issue 6220.– aaa3905-1–3905-6.

Sykes, M.V. Cometary dust trails. I. Survey /M.V.Sykes,R. G.Walker // Icarus.−1992. −Vol. 95, −P. 180-210.

Dorofeeva V.A.[1], Makalkin A.B.[2] Possible mechanism of depletiob of water atmospheres of Jupiter and Saturn. UDC 523.64

[1]- Vernadsky Institute of Geochemistry and Analytical Chemistry, Moscow, dorofeeva@geokhi.ru

[2]- Moscow,Schmidt Institute of Physics of the Earth, Moscow, an.makalkin@yandex.ru

Abstract. We set forth our ideas about the possible mechanisms of the observed water depletion in the atmospheres of Jupiter and Saturn at their enrichment with volatile elements heavier than neon (Ar, Kr, Xe, C, N, S, P), that was experimentally established during the space missions *Pioner-10, -11, Voyager-1, -2* and *Galileo*. The proposed scenario consistently takes into account the current data on the gas removal from the protoplanetary disks around young solar-type stars, the evolution of the thermodynamic conditions in the disks, and the model of the giant planets formation. The considered mechanism of water origin in the atmospheres of Jupiter and Saturn makes it possible to explain the significant deficit of water in comparison with the abundances of other volatiles.

Keywords: *Jupiter; Saturn; atmosphere; ice-rock planetesimals; volatiles, nebula; gas phase dissipation*

The features of the Jupiter and Saturn atmospheres largely reflect the conditions in the circumsolar gas-dust protoplanetary disk (Nebula) in the first millions of years of its evolution, and therefore the study of these features provides important information about the early stages of the evolution of the solar system as a whole. Jupiter and Saturn, the largest planets in the solar system; their masses are about 300 and 100 times greater than the mass of the Earth, respectively, and the total mass is about 92.5% of the total mass of the planets. Both planets have powerful atmospheres, the mass of which many times exceeds the mass of their nuclei. According to modern models, the ice-rock nuclei of Jupiter and Saturn formed in the first millions of years since the beginning of the evolution of the Nebula from the outside of the "snow line". Atmospheres of the planets were formed mainly by accretion of the gas phase of the disk by the nuclei of planets. That is why the main components of the atmospheres of Jupiter and Saturn are molecular hydrogen and helium.

The first data on the structure and composition of the atmospheres of Jupiter and Saturn were obtained by spacecrafts *Pioneer*-10.11 (1973-1974), and then with the help of spacecrafts *Voyager*-1,2 (1979). But the main data were obtained with the help of the Galileo orbiting spacecraft rotating around Jupiter (1995-2003), from which the special explorer (1995) was sent into the atmosphere of the planet. It has reached to the level with P = 22 bar deep into the atmosphere, determining its structure (P, T, ρ), chemical composition, cloud structure, etc. Some data with respect to the atmosphere of Saturn were obtained by the spacecraft Galileo. In 2016-2017 years the atmosphere of Saturn and the system of its rings was studied by the spacecraft *Cassini*, which made 23 overflights between the rings, and 6 overflights around of the planet itself.At the final stage of the experiment (the so-called "grand final"), *Cassini* entered the deep layers of the atmosphere, continuing to transmit information, which, unfortunately, has not yet been published. Since July 2016, the *Juno* spacecraft has went on the elliptical orbit around Jupiter. It is planned that it will make 37 revolutions, approaching for a few hours to the upper layer of the clouds of the planet for a distance of ~ 20 thousand km. In addition to researching the gravitational and magnetic fields of the planet, it is planned to study the composition of Jupiter atmosphere, in particular, the content of water and ammonia in it. By now, 46 articles on the preliminary results of the Juno mission have already been published in the journals "*Science*" and "*Geophysical Research Letters*".

By now, it is known that the microcomponents of the atmospheres of Jupiter and Saturn are NH_3, CH_4, H_2S, H_2O, etc. The composition of atmospheres of both planets and their structure is characterized by a number of important features. At the upper levels, some compounds (ammonia, hydrogen ammonium sulfate, etc.) form cloud layers, the P-T conditions for their condensation are shown in Fig. 1a The basic compounds of all elements are the reduced forms - NH_3, CH_4, PH_3, GeH_4, H_2S, although in the gas phase of the Nebula, by accretion of which atmospheres were formed, they were in the oxidized form - CO, CO_2, N_2, etc.

The reason for the reduced state of the atmosphere is that, the excess H_2 at deep levels with high T and P restores all oxidized forms, and then convection takes them upward. This mechanism is also considered in (*Atreya et al.,* 1999), while the coefficient of convective diffusion is determined from the vertical distribution of some carbon compounds: C_2H_2 from *Voyager* data, CH_3 from the data of the satellite ISO (infrared space observatory), as well as NH_3 on Jupiter and PH_3 on Saturn according to the *Hubble Space Telescope* data. The data of the *Juno* spacecraft indicate that ammonia is taken out from the $P \geq 100$ bar levels.

Another characteristic feature of the atmospheres of both planets is that they are enriched by all the chemically active and inert volatile elements heavier than Ne in comparison with solar proportions. For the Jovian atmosphere, this enrichment averages from 2 to 4 (Figure 1b), and for the atmosphere of Saturn it is even higher (*Atreya et al*, 1999). The only exception is oxygen. For the Jovian atmosphere, the global value of O / H = 0.033 ± 0.015 from solar value, and at the level P = 19 bar near the red spot 0.35. Preliminary data from the Juno spacecraft also indicate that the atmosphere of Jupiter is dry (*Orton et al.,* 2017).

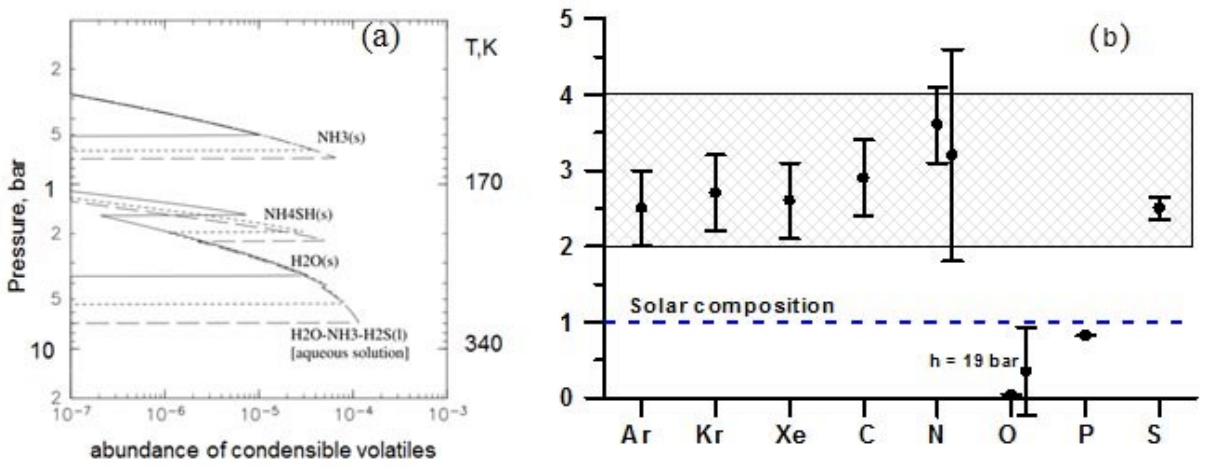

Fig. 1. The structure of the cloud layer (a) and elemental composition (b) of the atmosphere of Jupiter (according to Atreya et al, 1999 and Taylor et al., 2007)

The main hypothesis, explaining the enrichment of the atmospheres of Jupiter and Saturn with volatile elements, is based on the assumption that, at the final stage of atmosphere formation, giant planets accreted a large mass of ice bodies that contained volatiles not in the form of ice, as we suppose for primary ice-rock bodies, for example, comets, and in the form of clathrate hydrates: X • $5.75H_2O$ - for CH_4, CO, Xe, H_2S and X • $5.66H_2O$ - for N_2, Kr and Ar (*Kouchi et al., 1994; Mousis et al., 2000*;*Iro et al., 2003*; *Gautier et al.,* 2001a; *Hersant et al.,* 2004; *Alibert et al*., 2005 and etc.). As for the depletion of the Jovian atmosphere with water, no mechanism was proposed. We would like to note, however, that the enrichment mechanism involving clathrate hydrates has 2 significant drawbacks. First, the formation of clathrate hydrates of CO and N_2 - the main C and N-containing components of the gas phase of the disk - occurs in the interval T = 50-40 K, and the condensation of H_2O at $T \approx$ 140 K. So we can assume that during the cooling of the disk to 100 K H_2O_{ice} accumulates in the bodies. In this case the reaction surface sharply decreases and the heterogeneous reactions of formation of clathrate hydrates in the system containing of gases and solids will be largely kinetically inhibited. And, secondly, if their role was so great, then the atmosphere should be enriched with water, at least not less than other volatiles, and probably 4-5 times higher (*Helled, Lunine*, 2014).

We suggest a mechanism for depletion of the atmosphere of Jupiter, and probably Saturn, by water, which is based on the assumption that the atmospheres of these planets were formed as a result of the accretion of the gas phase of the nebula, enriched by all volatiles, heavier than neon, but practically free of water.

According to the standard model (Pollack et al., 1996), accumulation more than 60% of the mass of the giant gas planets occurs against the background of dissipation of gas from the disk. The mechanism of dissipation could be various. One of the most likely processes leading to gas loss is the scattering of the disk as a result of photo-evaporation of the gas by the ultraviolet radiation of the young Sun (*Gorti et al*, 2015). Another effective mechanism for gas loss and disk scattering is the magnetohydrodynamic wind (*Bai et al*, 2016). Both of these mechanisms ensure the outflow of gas from the disk in the hydrodynamic regime, those without the separation of heavy and light elements and their compounds. However, there are scenarios describing the local enrichment of the volatile gas phase of the nebula. One of them was proposed in the work (*Guillot, Hueso*, 2006) to explain the enrichment of the atmosphere of Jupiter and Saturn with the noble gases Ar, Kr and Xe, and then developed for chemical active volatiles in work (*Gorti et al*, 2015).Following the scenario proposed in these works, one can imagine the following scheme for the formation of atmospheres of giant planets. In the first million years from the beginning of the formation of the Solar system, the gas-dust substance continued to drop out onto the surrounding solar disk from the surrounding shell - the remaining part of the protosolar nebula, with a significant part of the substance falling onto the end of the disk, where the temperatures, especially on its surface, were extremely low, $T <\sim$ 20-30K (*Dorofeeva, Makalkin*, 2004). The dust particles of the protosolar nebula contained all the volatiles except H and He, in the form of ices, but, getting into the disk, it was possible to lose the most volatile of them, for example, neon. The particles descended to the middle plane of the disk, some of them formed aggregates that had a fluffy structure, and moved to the Sun during the radial drift. Getting to the warmer zones of the disk,

the ices of the most volatile compounds evaporated and passed into the gas phase. Further transport and diffusion of gas in a viscous accretion disk lead to an increase in their content in the formation zone of Jupiter and Saturn.

It is assumed that there is no thermal convection in the disk; otherwise, the gas (and fine dust) would mix in the vertical direction along the entire thickness of the disc, which would prevent enrichment of the volatile in this zone. The only volatile compound that could not evaporate at r ≥5 AU was ice H_2O, since the beginning of the accumulation of the rocky-ice core of Jupiter is the attainment in the equatorial plane of the disk by r_{Jup} = 5 AU. $T = T_{condH2O} \approx 150$K (at $P \sim 10^{-5}$ bar). And this gas, enriched with heavy elements, but practically free of H_2O_{gas} (in the gas phase, the partial pressure of water corresponded to $p_{H2O,\ T}$ in the gas-ice system) was accreted by growing Jupiter and Saturn. Water was accreted by protoplanets only in the form of H_2O_{ice} together with the refractory component, in the form of rock-ice planetesimals or dust, which could also include the highest-temperature condensed phases of the volatile - $NH_3 \cdot H_2O_{solid}$ and $CO_{2\ ice}$. It should be noted, however, that the share of carbon and nitrogen concluded in these compounds was not more than first percents of their total content (*Dorofeeva*, 2016). Thus, the atmosphere formed by the accretion of the gas phase of the near-solar disk will contain all the components, but in proportions above the solar one.

Thus, the atmosphere formed by the accretion of the gas phase of the near-solar disk will contain all the components, but in proportions above the solar ones. As for water, although it was almost absent in the accreted gas, but as a result of evolution it got into the atmosphere and its total content will consist of several sources. 1 - this is water, which was in the form of ice in the core of the planet; 2 - water, which came in the form of ice with rock-ice bodies of various sizes and dust, accreted by Jupiter during growth; 3 - water formed due to the reactions (1-2).

Oxygen in the gas phase is present only in the form of CO, CO_2, CH_3OH, etc. According to the latest results of the *Juno* mission (Orton et al., 2017) the vertical distribution of NH_3 indicating that there is vertical mixing in the Jovian atmosphere (convection). Due to this convection, atmospheric gases from the inner hotter zones with P ≥ 100 bar enter the upper levels, where some macrocomponents condense forming a dense cloud layer.

The main carbon and nitrogen compounds of the gas phase of the protoplanetary disk were CO, CO_2, CH_3OH and N_2. In the same forms they were accreted and due to intense convection, reaching lower, hotter levels are reduced by an excess of H_2 to CH_4 and NH_3, condensation which are observed in the upper atmosphere. Calculations show that the reduction reactions

$$CO + H_2 = CH_4 + H_2O \quad (1)$$

$$CO_2 + 2H_2 = CH_4 + 2H_2O \quad (2)$$

$$N_2 + 3H_2 = 2NH_3 \quad \text{et al} \quad (3)$$

in the conditions of excess H_2 pass efficiently already at the level $P \sim 200$ bar and $T \sim 500$ K. The mass of the water which formed by the reactions (1) and (2) will be determined by the ratio CO/CO_2 in the gas phase of the disk and $C_{organics}$ / ΣC in the dust component of the disk (*Dorofeeva, Devina*, 2018). So, if we assume that the mole ratio CO / CO_2 = 2 and $C_{organics}$ / ΣC = 0.5 the relative content of water in the atmosphere will be (H_2O/H_2) 3 times lower than according the solar proportions. This conclusion is supported by data from the Galileo probe. They indicated a slight increase in H_2O / H_2 at levels below 19 bar, where were recorded a 5-fold depletion of H_2O / H_2 (*Niemann et al.,* 1998).

The proposed scenario does not contradict the new models of the internal structure of Jupiter, obtained from the *Juno* spacecraft data. Measurements of the gravitational field of Jupiter obtained by *Juno* made it possible to obtain unprecedentedly accurate data on even (zonal) gravitational moments of low order J_2–J_8. New models of the internal structure of Jupiter (*Wahl et al*., 2018) better satisfy these gravitational data than other models. According this model, Jupiter contains a very large nucleus (with a radius of 0.3-0.5 R_{Jup}), weighing 10-24 masses of the Earth. But in this nucleus the most of the weight falls on hydrogen-helium mixture in which a heavy substance (ice + rocks) is dissolved.

Such a nucleus could be formed by eroding a primary dense core consisting only of ice and refractory components (ice and rocks). In order to satisfy the gravitational data, these preliminary models require a lower content of heavy elements Z (and helium Y) in the outer (molecular) shell than obtained according to spacecraft Galileo data. The best models satisfy the gravitational data, having in the outer shell Z ≤ 0.01. This estimate corresponds to the solar (*Lodders*, 2010) or even lower water content, even if it is assumed that all heavier and more refractory substances are situated lower, and in the outer shell the value of Z is determined by water only. This is consistent with some scenarios for the formation of Jupiter, for example (*Mousis, Lunine*, 2012).

The work is partially supported by the grant RFBR 17-02-00507

References:

Дорофеева В.А., Макалкин А.Б. Эволюция ранней солнечной системы// Космохимические ифизические аспекты. М.: ЕдиториалУРСС, 2004.–288 с.

Dorofeeva, V.A. Genesis of Volatile Components at Saturn's Regular Satellites.Origin of Titan's Atmosphere// Geochemistry International.–2016.–Vol. 54, No. 1.–P. 7–26.

Dorofeeva V.A., Devina O.A.Evaluation of the mass fraction of water ice in the rock-ice planetesimals for cocmochemical data.–2018.ibit.
Atreya, S.K. A comparison of the atmospheres of Jupiter and Saturn: deep atmospheric composition, cloud structure, vertical mixing, and origin /S.K.Atreya [et al.] // Planetary and Space Science.–1999.–Vol.47.–P. 1243-1262.
Bai, X-N., Ye, J., Goodman, J., Yuan, F.Magneto-thermal Disk Winds from Protoplanetary Disks //Astrophysical Journal.–2016.–Vol.818, Issue 2.–article id. 152. 20 pp.
Gorti, U., Hollenbach, D., Dullemond C. P.The impact of dust evolution and photoevaporation disk dispersal // Astrophysical Journal.–2015.–Vol. 804. Issue 1, article id. 29.–21p.
Guillot, T., Hueso, R. The composition of Jupiter: sign of a (relatively) late formation in a chemically evolved protosolar disc // Mon. Not. R. Astron. Soc.–2006.–Vol.367, –L47–L51.
Helled, R., Lunine, L. Measuring Jupiter's water abundance by *Juno*: the link between interiorand formation models // MNRAS.–2014.–Vol.441.–P. 2273–2279.
Mousis, O.Nebularwater depletion as the cause of Jupiter'slow oxygen abundance /O.Mousis[et al.] // Astrophys. J. Lett.–2012.–Vol.751.–L7.
Orton, G. S.Multiple-wavelength sensing of Jupiter during the Juno mission's first perijove passage /G.S. Orton [et al.] // Geophysical Research Letters.–2017.–Vol. 44, Issue 10.–P. 4607-4614.
Taylor, F.W.The Composition of the Atmosphere of Jupiter / F.W. Taylor [et al.] In: Jupiter, Fran Bagenal (ed.) [et al.], Cambridge. UK: Cambridge Univ. Press,2007.–P.59-78.
Wahl, S.M.Comparing Jupiter interior structure models to Juno gravity measurements and the role of a dilute core / S.M. Wahl[et al.] //2018.Geophysical Research Letters.–2018.–Vol. 44, Issue 10.–P. 4649-4659.

Dunaeva A.N., Kronrod V.A., Kuskov O.L. Main constraints on the chondritic component composition in partially differentiated Titan.

V.I. Vernadsky Institute of Geochemistry and Analytical Chemistry RAS, Moscow (dunaeva.an@gmail.com)

Abstract. In this paper, the models of partially differentiated Titan consisting of the ordinary (L/LL) or carbonaceous (CI/CM) chondrites have been considered. The models were made in the range of the satellite's moment of inertia $0.32<I/MR^2<0.35$ and with different degree of the chondritic substance hydration. It has been shown that the region of the hydrous phases existence in the Titan core does not exceed ~30 vol.% of the core at a satellite core radius of about 1000 km and reaches up to ~70 vol.% at the small radii (~500 km). At the moment of inertia $I/MR^2=0.35$, it is impossible to build Titan with CI/CM chondrites. In this, the L/LL-chondritic models lead to the satellite core radius less than 700 km, which appears to be unrealistic for the large ice satellites. Thus, the high moment of inertia in the partially differentiated Titan seems to be unlikely.

Keywords: *Titan core, CI/CM chondrites, L/LL chondrites, hydrous silicates, moment of inertia.*

According to the contemporary theories, the formation of the regular satellites of gas giant planets has continued in gas–dust circumplanetary accretion discs during the final stage of central planets formation, i.e. 4-8 Myr after meteoritic Calcium-aluminum-rich inclusions (CAI) occurrence (Makalkin, Dorofeeva, 2014). Simulated results of accretion process in gaseous subnebulae (Kronrod, Makalkin 2015) revealed that satellites like Titan and Callisto were accumulated from the small (less than 10-15 m) rock-ice particles (planetesimals) consisting of H_2O ice and rock-iron components. Models of the internal structure of Jupiter and Saturn large satellites (Kronrod, Kuskov, 2001, 2005; Castillo-Rogez, Lunine, 2010) impose the restrictions on the satellites rock composition in accordance with the substance of ordinary (L/LL) or carbonaceous (CI) chondrites. In this case chondritic substance is generally represented by ferromagnesian silicates (olivine and pyroxene) or hydrous minerals (serpentines, smectites) with an admixture (up to 30%) of secondary minerals (iron compounds + Fe^o, sulfates, carbonates, feldspars, spinels, phosphates). An insignificant amount (up to 5%) of organics and up to 20-22% of water, being a part of water-bearing minerals, is also present in carbonaceous chondrites.

The satellites' iron-silicate substance can be partially or completely hydrated. Hydration/serpentinization reactions relatively quickly occur, both on the scale of geological time and in comparison with the rate of satellites' accretion (Castillo-Rogez, Lunine, 2010). These reactions can occur at different stages of evolution of the rocky-ice objects, leading to formation of low-density hydrated phases (hydrous silicates). Given the fact that both small particles and large volumes of planetary bodies can be involved in the hydration reaction, hydrous silicates become a significant component in their composition. The presence of hydrated minerals affects the density of the chondritic substance, and also imposes certain limitations on the satellites thermal history, which should be taken into account during constructing models of their composition and internal structure.

The formation of Titan occurred within the protosatellite Saturnian disc according to the main pattern formation of the regular satellites of gas giant planets. The Titan accretion from small rock-ice particles occurred for a continuous period of time $\approx 10^6$ years (Makalkin and Dorofeeva, 2014), which has made it possible to form Titan, initially consisting of a homogeneous ice and rock mixture (Barr et al., 2010). During the last stages of accretion, as a result of impactors action, the temperature of the near-surface Titan's regions increased sufficiently to initiate the ice melting. This leads to the separation of the rock-iron component and its migration to the satellite center accompanied

by formation of inner rock-iron core. Surface water and ice formed an outer water-ice shell. Between the water-ice shell and the inner core a homogeneous rock-ice mixture (the rock-ice mantle) remains. This model of Titan partial differentiation (incomplete substance separation into ice and rock) is similar to the model (Barr et al., 2010), where the ice melting is caused by late heavy bombardment, which occurred 4.1-3.8 Gyr ago. The energy of the satellite gravitational differentiation is partially used for the rock-ice mantle heating, but is generally spent on increasing the temperature and the phase transitions in the rock-iron core. Hereafter the core is heated by energy of radioactive sources, such as long-lived isotopes ^{238}U, ^{232}Th, ^{40}K.

Radiogenic heating of the Titan silicate rocks may lead to the temperature increasing to the level at which the reverse reactions of hydrous silicates dehydration occurs. Such reactions are irreversible (i.e. no repeated transition of silicates to hydrosilicates occurs) as it is assumed that water released from dehydration is rapidly removed. The temperature line of stability of the hydrous silicates (the boundary of the hydrous silicates/silicates phase transition) under Titan conditions is equal to about 900K and is achieved at the depths of the inner core of the satellite.

The main task of the paper aims to determine the region of hydrated phases stability in the Titan structure. Degree of the satellite silicate core hydration is assessed, depending on the satellite core size, moment of inertia, and type of chondritic substance. The most appropriate compositions of the Titan's chondrite substance are discussed which correspond to the model of a partially differentiated satellite.

Tabl. 1. Model compositions of chondritic substance in Titan, wt%.

Type of chondrite	Silicates (olivine + pyroxene)	Hydrous silicates (serpentines, smectites)	Minor minerals	H_2O
L/LL	70	0	30	0
CM	15	75	10	15
CI	0	85	15	22

The model of the partially differentiated Titan (Barr et al., 2010; Dunaeva et al., 2016) assumes the following structural layers in the satellite: 1) outer water-ice shell composed by the ices Ih, III, V, VI + aqueous or water-salt ocean, 2) rock-ice mantle (rock-iron component + high pressure water ice VI, VII), 3) central silicate core. Composition of the silicate component of the mantle and the core is modeled by L/LL or CI/CM chondrites substance. Based on the mineral composition data of different types of chondrites, the average compositions of the chondritic substance were chosen for modeling (Table1).

The density of a chondritic substance is determined in proportion to the amount of hydrated and anhydrous (purely silicate) phases in it composition. This proportion depends on the type of chondrites and degree of chondritic substance hydration (variable parameter of the model). The density of the chondrite component is calculated using the silicates and hydrous silicates equations of states. The average density of minor minerals, obtained in this paper on the basis of published experimental data, is estimated at the values of 3.9-4.6 g/cm3. The density of water ice Ih, III, V, VI, VII and liquid water in the water-ice shell and in the Titan's ice-rock mantle was calculated using the individual H_2O phase's equations of state. According to the references data, the value of the surface heat flux of Titan was assumed to be 5 mW/m^2. The calculations were made at the moments of inertia $0.32<I/MR^2<0.35$.

The model of the Titan rock-ice mantle was constructed on the assumption of existence of the global convection in the mantle reservoir. The ice/rock ratio in the rock-ice mixture is one of the main constrains of such model. Apparently, the content of rock in mantle should not exceed the certain limit values, as this may restrict the substance convection, leading to the ice melting and, as a consequence, to the complete differentiation of Titan into rock and ice. Taking this constrain into account leads to excluding some results from the interpretation. In this study, however, the results obtained are shown in full, as for the purpose of this paper, such restriction is not essential and does not affect the general conclusions.

The temperature distribution in Titan was estimated using the following models: within the outer ice crust composed by ice Ih and in the inner satellite core - by conductive heat transfer model; in the internal ocean, in high pressure H_2O ices and in ice-rock mantle - according to convective model.

The thermal model of the Titan core was developed for the conditions of stationary thermal regime, assuming spherical symmetry and uniform distribution of radioisotope heat sources in the core. In this case, the thermal balance of the core is expressed by the equation:

$4/3\pi R^3 \cdot H = -4\pi R^2 \cdot dT/dR \cdot k$, where

H – heat production rates of radioactive sources in Titan's core, $W\ m^{-3}$,

k – the thermal conductivity: $k = 2.95\ W \cdot m^{-1}K^{-1}$ и $k = 4.2\ W \cdot m^{-1}K^{-1}$ for hydrated and anhydrous silicates, respectively (Neveu, Rhoden, 2017; Abramov, Mojzsis, 2011).

By integrating equation (1) with respect to R and substituting the boundary conditions for the temperature at the upper boundary of the core (T_0)

and the lower (T_i) boundary of each i-layer inside the radii R_0 and R_i, respectively, a general equation for the stepwise calculation of the temperature in inner Titan core is derived: $T_i = T_0 + 1/6\ H/k\ (R_0^2 - R_i^2)$.

To estimate the current temperature distribution in Titan, the heat production rate of radioactive sources (H) is assumed to be $4.242 \cdot 10^{-12}$ W/kg and $4.5\text{-}4.7 \cdot 10^{-12}$ W/kg for water-containing (CI/CM) and ordinary (L/LL) chondrites, respectively (Mueller, McKinnon, 1988; Spohn, Schubert, 2003). It is assumed that the phase transitions of hydrous silicates/silicates in the core occurred and were basically completed in the period of ~ 1Gyr after CAl formation, at which point the heat of radioactive sources was significantly higher than the present values. Therefore, the determination of the region of hydrous silicates existence (the depth of the 900K isotherm location in the core during maximum core warming) was performed with allowance for the earlier H values, that exceeded the present H values by 5.6-6 times: $2.545 \cdot 10^{-11}$ - $2.834 \cdot 10^{-11}$W/kg (Mueller, McKinnon, 1988).

The summarized results on the calculations of extent of Titan core hydration are shown in Fig. 1. The data shown indicate that size of the hydrous silicates stability region in the core ($\frac{Rc - Rsil}{Rc}$, where R_c is the core radius, R_{sil} is the radius of the silicate part of the core) are almost independent on the chondrites type, but inversely depend on the core radius. Taking into assumption that in the given model the size of Titan core is equal to ~1000 - 1100 km (Barr et al., 2010; Dunaeva et al., 2016), i.e. small sized cores are unlikely, then the expected sizes of the hydrated part of the core will not exceed 10% Rc or ~30% of the core volume. In this case, small sized cores (Rc = 500-600 km) may be hydrated for the maximum of up to 70% of its volume (for the experimentally measured moment of inertia I/MR^2=0.342).

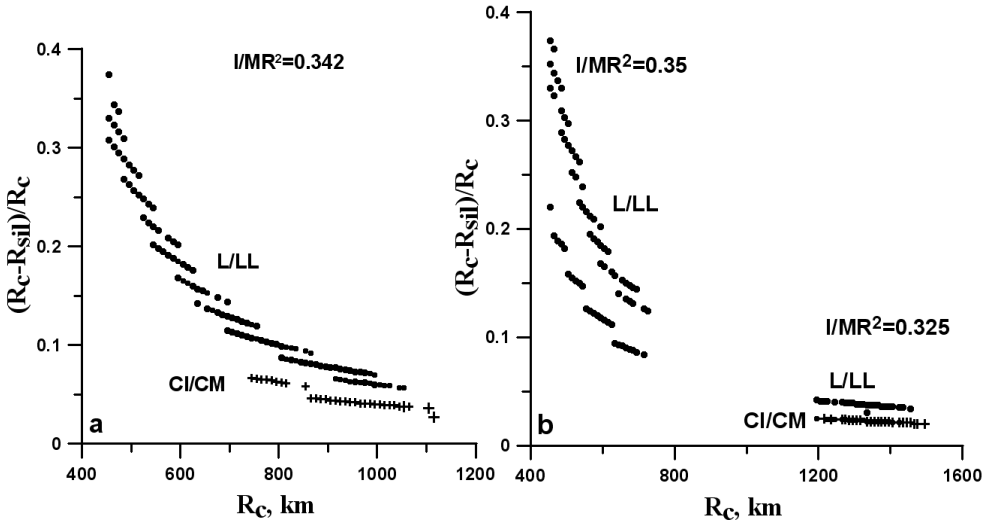

Fig. 1. The region of Titan's core hydration, depending on core size and the type of chondritic substance. Calculations are shown for the experimentally measured moment of inertia I/MR^2=0.342 (a) and for the moments of inertia I/MR^2=0.325, I/MR^2=0.35 (b). Points and crosses - calculations for L/LL and CM/CI chondrites, respectively.

The size of Titan inner core substantially determines the satellite moment of inertia value. In general, the regularity is such that, with the moment of inertia increasing, the maximum permissible value of the core radius decreases (Dunaeva et al., 2016). Calculations showed (Figure 1) that for the heat flux of 5 mW/m^2 and the moment of inertia 0.342, the maximum radius of the Titan core composed by L/LL-chondritic substance is 1050 km, and in case of carbonaceous CI/CM chondrites - 1100 km. For the moment of inertia 0.325, the maximum core sizes are respectively equal to 1430 and 1490 km. For high moment of inertia values (I/MR^2 = 0.35), it could not be possible to build a Titan model using the substance of CI/CM chondrites, and for a satellite composed of L/LL chondrites, the maximum core radius does not exceed 720 km, which is much less than the expected core size in Titan. Therefore the high values of the moment of inertia in the partially differentiated Titan seem to be unlikely.

Conclusions:

1. A study of the possible compositions of rock-iron substance in partially differentiated Titan was conducted. Composition of the satellite silicate component was modeled by the substance of ordinary (L/LL) and carbonaceous (CI/CM) chondrites at different degrees of chondritic substance hydration. Calculations were performed in the interval of satellite moments of inertia I/MR^2 = 0.32–0.35. Based on the proposed stationary thermal model of the Titan core, estimates of the temperature distribution in the satellite core were obtained and regions of the hydrated phases existence in the core were determined.

2. It is shown that the region of the hydrous silicates stability in the Titan core does not exceed ~30% of the core volume at a core radius Rc ~1000 km and reaches up to 70% of the volume for the small cores (Rc ~500 km).

3. At high values of the Titan moment of inertia (I/MR^2 = 0.35) it is impossible to build a satellite from the carbonaceous CI/CM chondrites substance. For a satellite composed of L/LL chondrites, only models with small sized cores are possible, which are not typical for the model of partially differentiated Titan.

This research was supported by the RFBR grant (№ 18-05-00685).

References:

Dunaeva A.N., Kronrod V.A., & Kuskov O.L. (2016). Physico-chemical models of the internal structure of partially differentiated Titan. *Geochemistry International*, *54*(1), 27-47.
Kronrod V.A., Makalkin, A.B.. (2015). Capture of material by the protosatellite disks of Jupiter and Saturn due to interaction of the in falling planetesimals with the gaseous medium of the disks, Experiment in GeoSciences, 2015, in russian.
Makalkin, A. B., & Dorofeeva, V. A. (2014). Accretion disks around Jupiter and Saturn at the stage of regular satellite formation. Solar System Research, 48(1), 62-78.
Barr A.C., Citron R.I., Canup R.M. (2010) Origin of a partially differentiated Titan. Icarus, 209(2), 858-862.
Castillo-Rogez J.C., Lunine J.I. (2010) Evolution of Titan's rocky core constrained by Cassini observations // *Geophys. Res. Lett*. 37, L20205.
Kuskov O.L., Kronrod V.A. (2001) Core sizes and internal structure of the Earth's and Jupiter's satellites // Icarus, V. 151, 204-227.
Kuskov O.L., Kronrod, V.A. (2005) Internal structure of Europa and Callisto, Icarus, V. 177, 550–569,
Mueller, S., & McKinnon, W. B. (1988). Three-layered models of Ganymede and Callisto: Compositions, structures, and aspects of evolution. Icarus, 76(3), 437-464.
Neveu M., & Rhoden, A. R. (2017). The origin and evolution of a differentiated Mimas. Icarus, 296, 183-196.
Spohn T. and Schubert G. (2003) Oceans in the icy satellites of Jupiter? // Icarus. 161, 456– 467.

Ivanov A.A., Sevastyanov V.S., Voropaev S.A., Dnestrovskiy A.Y., Galimov E.M. Experimental modeling of microsphere formation process in organic broth during pneumatic impact. UDC 550.47

Vernadsky Institute of Geochemistry and Analytical Chemistry RAS, Moscow (*aiva@geokhi.ru*)

Abstract. Method for producing microspheres during pneumatic impact in aqueous-protein solution, imitating the similar natural processes on abrasive shores along the World Ocean line and modeling a possible mechanism for the formation of the cell membranes of the first probionts has been developed.

Keywords: *pneumatic impact; microspheres; abrasive shore; organic broth; probionts.*

Comprehensive scientific research shows that chemical basis of life was originally present at early stages of formation of the Earth, not only in the form of required chemical elements, but also in the form of low molecular organic compounds that regularly come in with cosmic dust and other extraterrestrial substance. In conditions of early Earth, thanks to the rapid geological events, as well as UV-radiation from the Sun, atmospheric electric discharges, meteor impact, natural decay of radioactive elements and many other sources of energy, synthesis of organic compounds not only continued, but also moved to high-molecular region, enhancing accumulation and conversion processes of prebiological components. Experimental modeling of the proposed processes confirmed the real probability of the development of such events, and was described in a variety of works (Miller, 1953, Miller et al, 1959, Lupatov et al., 2006). Therefore, for today, in science there is understanding of experimental and theoretical problem of nature and appearance of the first "bricks" of life on the Earth. But presence of the components of prebiotic substance by itself does not mean the unconditional emergence of life. This is only one of the necessary initial conditions. These bricks had yet to somehow properly be arranged in a separate micro-volume system of the most complex molecular structures that organize metabolism of the first living organisms. Of course, such separation must be accompanied by a certain sign reason, which preceded beginning of the path of the most complex structural self-ordering of substance, which led to the abiogenic self-generation of life. Even if we assume that all constituent cells were in the right amount and proportions, that is completely not enough, since a living organism is not simply a set of all required components. To all this, it was still necessary to start initiating structural formation of the cell, gradually building up the coordinated metabolism. Probably, to begin the implementation of this stage, not only all components, conditions and circumstances are needed. The question of "what can initiate the

Figure of a separately selected cell of the abrasive shore. The basis for the drawing was an image of an abrasive bank taken from the Internet section http://monateka.com/images/1698545.jpg

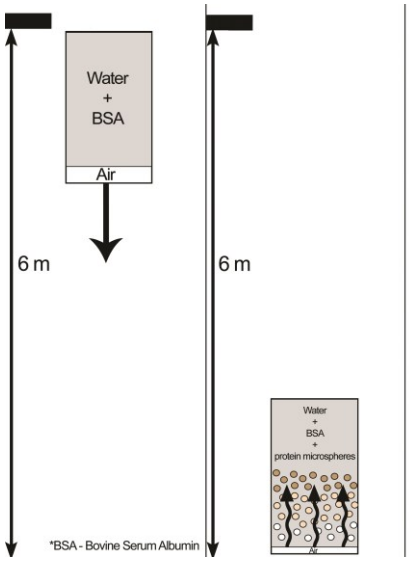

$$\Delta E_{kin} = \frac{m_{liq} \cdot \mathcal{V}_{fin}^2}{2} =$$

$$= m_{liq} \cdot g \cdot H = 72\,J$$

$$\Delta E_{kin} = \Delta U$$

$$\Delta U = \frac{5}{2} \cdot \frac{m_{air}}{M} \cdot R \cdot \Delta T$$

$$\Delta T \approx 200°C$$

Calculation and scheme of the model experiment.

beginning of structural formation of the first living organisms from the prebiotic substance" remains controversial, requires additional research and finding new approaches to the solution of the problem. In this paper, we consider an unaccounted source of energy of tidal waves and surf waves that cause pneumatic impact in cavities of abrasive shores. This source of energy, according to available geological data, appeared 4 billion years ago simultaneously with the formation of the primary ocean of the Earth. Together with other sources of energy, it also contributed to the development and transformation of organic broth. Organic broth, in the conventional sense - is a first-born basis, which served as abiogenic spontaneous generation of life. It was formed on the early Earth in the process of formation of the first water basins. In fact, it is an aqueous solution of simple and complex organic compounds. Long-term exposure to various energy sources has altered the molecular structure of these compounds. Afterwards, it was assumed that not only the composition and concentration changed, but also the complex combination of these dissimilar compounds into separate high molecular formations, which probably had prebiological importance (Oparin, 1957, Galimov, 2001). Following these scientific arguments, it can be concluded that the readiness of the Earth for the spontaneous generation of life took place about 4 billion years ago. However, it was still far away before the appearance of the first living organisms. Something should have happened that later would lead to conversion from chaotic and accidental events to a regular and sustainable process of organizing the order in prebiological structures and forms. Such a turning point could mean the true beginning of the prebiological stage, which lasted until the appearance of the first elementary and minimal-sufficient unit of life-cells! Thus, howsoever and in what conditions life on the Earth or in the Universe would have arisen, it must begin with a cell, since only the cellular structure is capable of providing a homeostasis that predetermines functional stability of metabolism and the regularity of hereditary information transfer. But how was the first cell formed? There is no such complexity in the inanimate nature, in comparison with even the most primitive living organism! After all, even a primitive, but fully viable cell contains millions of components required for independent existence. This is the most important and difficult matter of the origin of life! A correct vision of the order of events of abiogenic self-assembly of the first living organism, as well as understanding how this became possible, is a key to success of the solution of the problem. It is logical to assume that self-assembly of the cell began with a shell that organized a space for inner interactions of all of its future components. Without that shell - a wall that serve as a protection from an aggressive external environment - the cell is not a cell because of lack of joint isolation of all its components. Separation from the external environment, subsequently organizes close interactions of all the necessary constituent components of the cell. Therefore, the cellular structure seems to be the very first organizing structure in the prebiological stage of the abiogenic self-generation of life. The shell of the first cell must be permeable to the structural elements that build the internal compartment. In the subsequent stages, formation of the cell wall, on the inner part of it opened the possibility of forming a phospholipid membrane. Such shell organization is found in the most ancient representatives of life - the archaea, the cell membrane of which consists of proteins, which contain both D and L-amino acids.

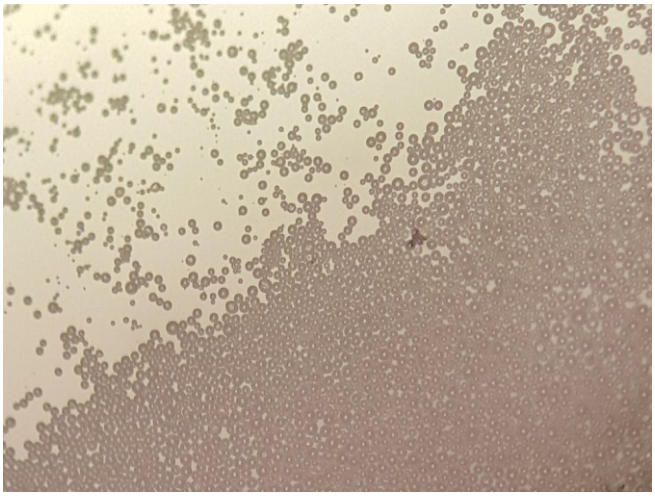

Protein microspheres, in the size from 1 to 10 microns, obtained in the model experiment.

Assuming that cell appeared from the shell, and the phenomenon of the transformation of inanimate substance into living things occurred in the cell, one should also accept that the formation of a cell membrane is the key event in the beginning of the structural formation of living matter, without which everything would remain simply some substance. However, the shell, being the organizing beginning of the first cell, could not have a biological nature in the original cause of its formation. This probably

imposes separate demands not only on structural components, conditions and circumstances, but also on the place of origin for its formation in the primordial environment. But, is it possible to find out what could be such a place? This is a very important question, since to understand the true nature of the mechanism of structural formation of cell membranes means to take the right path to understand the principles of the formation of the first probionts. Probionts are intermediate isolated structures capable of displaying the first individual signs of the living due to external influence. Obviously, the identification of a universal source of energy causally linking the production of organic compounds with the production of cell membranes will help to avoid the false path of research. This predetermines and will bring about a further action - the compulsory initiation of intracellular metabolism of the first probionts. But, such a natural source of energy, meeting all these requirements, should initially be present on the early Earth. Such a source, in our opinion, can be the energy of surf waves, which causes a pneumatic impact in the closed water stopper cavities of abrasive banks, partially filled with coastal water containing organic broth. The resulting pressure and temperature jump during the pneumatic strike set in motion the contents of these cells, making structural transformations of the substance and the formation of shells in the form of polypeptide microspheres. Thus, the nature of structural transformation of matter mechanism is assumed to be as follows.

Continuously rolling waves on the rocks, in the course of time form a rocky abrasive shore. Imagine that the waves hit the abrasive ledge. With each stroke of the waves, the air, closed in cavities of the abrasive shore, previously formed from the same waves, heats up under pressure of water. And, depending on the strength of the shock waves, instantaneous temperature that occurs with such a pneumatic shock, according to mathematical calculations, can reach hundreds of degrees! The waves retreat, and the air in the cavities of the cells, being diluted, cools down. Each cell with the next cycle of compression-decompression, heating-cooling, works like a natural thermal cycler. As is known, the thermocyclic regime can initiate the course of a number of molecular biological processes (Mills et al, 1991; Varfolomeev et al., 2008). With a frequency of several times per minute, the rhythm of the pulsation of the heating and cooling cycles manifested itself immediately with the formation of the first large reservoirs and abrasive shores. For billions of years, this pulse of the Earth is felt all along the coastline of the World Ocean, which today is about 504,000 km. About 4 billion years ago, when the radius of the moon's rotation was much smaller, and day and night at times shorter, the young Earth-Moon system was a powerful source of energy generation for tidal waves. Tidal waves also caused a wide range, an instantaneous burst of thermal energy, which occurs when air impact cavities of abrasive shores. Such a powerful and regular source of energy was able to provide in the entire coastline of the Earth the synthesis and destruction required for the prebiological stage, and organic compounds and microspheres. And so, under the pressure of waves, day and night all year round, myriads of cells of abrasive shores, subject to cyclic action of pressure and temperature, could play the role of thermocyclers able to effectively produce organic compounds and continuously produce a myriad of microspheres. Thus, each isolated cell of abrasive shores could be a cause of the formation of the first probionts, which, to all, would be protected there from the harmful effect of ultraviolet radiation of the Sun, which is excessive in the oxygen-free atmosphere of the young Earth. Based on these considerations, we carried out a number of experiments on the synthesis of microspheres in water-protein solutions with air impact, and also carried out the polycondensation of amino acids and the synthesis of monosaccharides from formaldehyde. The idea of obtaining protein microspheres is as follows. In a closed volume of a vessel simulating a separate cavity of the abrasive shore and partially filled with an aqueous-protein solution, during air blast the air from the sharp compression is heated and the hot bubbles gasses the solution. In this case, under the influence of pressure and temperature, a protein film coagulating at the hot boundary of the bubbles, forming a microsphere. In the first model experiments, small gas cylinders were used, from 0.1 to 1.5 liters, 2/3 by volume filled with a 5% aqueous-protein solution and 1/3 air. Bovine serum albumin (BSA) was used in this experiment. The balloon was dropped into a 6-meter-high pipe, so that the solution was on top of the air portion. With a rigid balloon impact on the Earth, the water-protein solution, falling inertially, worked like a piston, squeezing the air. As a result, protein microspheres were formed in this plural solution.

The mechanism of their formation is the following. The water, which is in the upper part of the balloon, under severe braking, compressed the air, gasifying under pressure a water-protein mixture. Small air bubbles at high speed under pressure penetrate into the liquid and form microspheres, coagulating the protein at their hot verge.

Conclusion Microspheres obtained by this experiment are stable for months. The model of experiment convincingly demonstrates that pneumatic strike, as a regular and universal source of energy, could effectively cope with the task of producing microspheres, which perform a role of the cell membranes of the first probionts in the prebiological stage of abiogenic self-generation of life, where metabolism was initiated by pressure pulsation. In the process of experimental and theoretical studies, we came to the conclusion that abiogenic spontaneous generation of life, with a high probability, occurred precisely in the shoreline of the abrasive ridges of the primary ocean of the Earth.

References:

V.M. Lupatov, V.P. Strizhov, A.A. Ivanov, V.G. Tokarev, V.M. Simakova, E.M. Galimov. // Modeling of fusion reactions of the organic compounds in conditions of a primary atmosphere of the Earth//International symposium on molecular photonics. 2006.St. Petersburg, Russia. June 28-Jule2.

*S.L. Miller (May 1953). «*A production of amino acids under possible primitive earth conditions*». Science (New York, N.Y.)* ***117*** *(3046): 528–9.*

*S.L. Miller, H.C. Urey (July 1959). «*Organic compound synthesis on the primitive earth*». Science (New York, N.Y.)* ***130*** *(3370): 245–51.*

K.B. Mills, F.A. Faloona // Biotechnol. — 1991. — V.155. — P. 335—350.

S.D. Varfolomeev, O.V. Demina, A.A. Khodonov, A.V. Laptev, E.N. Nikolaev, A.S. Kononikhin. Prebiological evolution of macromolecules. The world of peptides. Moscow: Publishing House "LIBROKOM", 2008. - 552 p. (in Russian)

EM. Galimov. The phenomenon of life: between balance and nonlinearity. The origin and principles of evolution - M.: Editorial URSS, 2001. - 256 p. (in Rusian)

AI Oparin. The emergence of life on Earth. Publishing house of the USSR AS. Moscow. 1957. (in Russian)

Kronrod E.V.[1], Kuskov O.L.[1], Kronrod E.V.[1], Nefedyev Yu. A.[2] Calculation of bulk silicate Moon composition on the basis of selenodetic ans seismic data. UDC 550.41:550.42

[1]V.I. Vernadsky Institute of Geochemistry and Analytical Chemistry RAS, Moscow

[2]Kazan Federal University, Kazan (e.kronrod@gmail.com)

Abstract. We have obtained bulk silicate Moon (crust + mantle, BSM) composition from gravity and seismic data inversion. It was shown that abundance of refractory oxides in the mantle depends on thermal state and can be divided into two groups. For cold BSM models Al_2O_3 ~ 3.0-4.6 wt.% is similar to the Al_2O_3 content in the Bulk Silicate Earth (BSE), whereas hot models are enriched in Al_2O_3 (~ 5.1-7.3 wt.%) compared to BSE (Al2O3 ~ 1.2 – 1.7 × BSE). In contrast, both types of models possess almost constant concentrations of FeO ~ 12-13 wt.% and MG# 80-81.5, completely different from those of BSE (FeO ~ 8 wt.% and MG# 89). It can be concluded that for geophysically possible temperature distribution silicate part of the Moon is enriched in FeO and depleted in MgO compared to BSE.

Keywords: *Moon, internal structure, chemical composition, temperature, thermodynamic properties.*

One of the most important tasks of the geochemistry of the Moon is the determination of its bulk composition - the concentrations of the main oxides of SiO_2, Al_2O_3, FeO and MG#, affecting mineralogy, physical properties of the mantle, thermodynamics and dynamics of magmatic processing and crystallization of the lunar magma ocean, LMO). The purpose of this paper is to evaluate these geochemical parameters on the basis of a combined inversion of gravitational, seismic and petrological data by the Monte Carlo method in combination with the Gibbs free energy minimization method in the Na_2O-TiO_2-CaO-FeO-MgO-Al_2O_3-SiO_2 (NaTiCFMAS) system.

Approach We consider the model of differentiated Moon as a result of partial melting of the originally homogeneous Moon - the magmatic ocean model (lunar magma ocean, LMO) (Dauphas et al., 2014). Based on the inversion of selenodetic data (Williams et al., 2014) and seismic data (Gagnepain-Beyneix et al., 2016), self-consistent models of chemical composition, mineralogy, and velocities of the P- and S-waves of the three-layers mantle of the Moon have been constructed.

The chemical composition and physical properties of each mantle zone (i = 1, 2, 3) are determined by solving the inverse problem within the system NaTiCFMAS with solid solutions (Kronrod et al., 2011, Kuskov et al., 2014). Sharp change of composition is allowed only on geophysical boundaries. In each zone, the composition is considered to be constant and equal to the values at some points in the middle of the mantle zone, combined with the natural requirement of no density inversion.

Modeling of the composition and physical properties of the lunar mantle was carried out in the range of oxide concentrations within the wide range of probable lunar compositions (Taylor, 1982, Snyder et al., 1992, Longhi, 2006, Kronrod et al., 2011, etc.) (wt%) : $25 \le MgO \le 45\%$, $40 \le SiO_2 \le 55\%$, $5 \le FeO \le 15\%$, $0.1 \le CaO$, $Al_2O_3 \le 7\%$, (1), with the chondritic relation between concentrations of Al_2O_3 and CaO ($CaO \sim 0.8Al_2O_3$); $Na_2O = 0.05\%$ and $TiO_2 = 0.2\%$ (Dauphas et al., 2014).

The solution to the problem of determining the bulk composition of the Moon, the density, the velocities of the P- and S-waves (V_P, V_S) in each mantle zone, as well as the core dimensions, is performed by the Monte-Carlo method (Kronrod et al., 2011) (uniform distribution). To calculate the equilibrium composition of mineral associations and their physical properties, the method of minimizing the Gibbs free energy, taking into account the equations of state of minerals in the Mie-Grüneisen-Debye approximation, is used based on the THERMOSEISM software package.

Temperature in the lunar mantle The temperature range in the mantle $450 < T_{150km} < 700^oC$, $750 < T_{500km} < 1200^oC$, $1000 < T_{1000km} < 1400^oC$ (1) covers the range of temperatures (Gagnepain-Beyneix et al., 2006; Khan et al., 2007; Kuskov et al., 2014a) (Fig. 1) with a further temperature increase at the core boundary. In calculations of the chemical composition, we consider the entire set of selenoterms lying in a given interval and satisfying the constraints on the derivatives. Each selenoterm additionally satisfies the condition that the temperature gradient decreases with depth $(dT / dH)_{i+1} < (dT / dH)_i$. The maximum value of dT / dH for a zero density gradient decreases monotonically from ~

1.17 deg / km in the upper mantle to ~ 0.5 deg / km at H = 1000 km (Kuskov et al., 2014a).

As an integral characteristic of the thermal state of the Moon, the mean bulk mantle temperature T_{mean} was used, which for our model is calculated from the expression:

$T_{mean} = (T_u V_u + T_m V_m + T_l V_l)/(V_u + V_m + V_l)$, (2),

where T_u, T_m, T_l – mean mantle temperature (°C) in three mantle layers, V_u, V_m, V_l – the volumes of the upper, middle and lower mantle, taking into account the fact that the radius of the core, obtained as a result of solving the inverse problem with an average crustal power of 39 km, is in the range of 260-280 km, which is in a good agreement with Williams et al. (2014). Since in our model the temperature in each zone of the mantle is considered equal to the temperature at some average depth for a given zone, then taking into account the volumes of the three zones of the mantle, T_{mean} can be represented as:

$$T_{mean} = 0.33T_{150} + 0.478T_{500} + 0.193T_{1000} \quad (3)$$

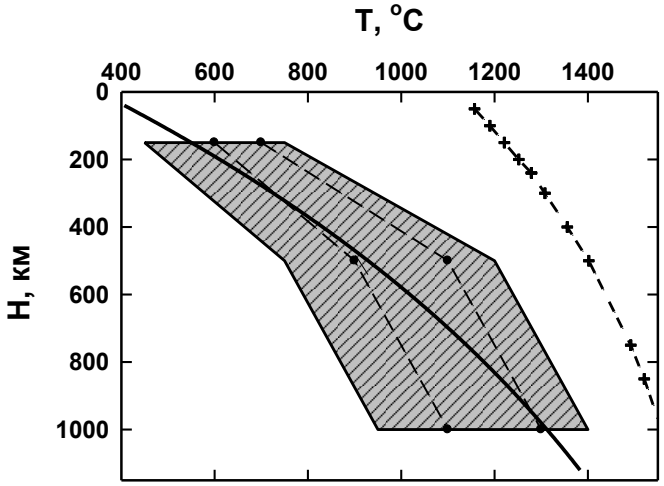

Fig. 1. The distribution of temperatures in the lunar mantle from geophysical models (Hood, Jones, 1987; Kuskov, Kronrod, 2009; Lognonné et al., 2003; Gagnepain-Beyneix et al., 2006; Khan et al., 2006a, b; Kuskov et al., 2014). The profiles of all selenoterms correspond to the condition of increasing temperature with depth, $T_{i-1} \le T_i \le T_{i+1}$. The solid line is the temperature profile by the equation T(°C) = 351 + 1718{1 – exp[–0.00082H(км)]}(Kronrod, Kuskov, 2011). The crosses are the solidus of peridotite (Hirshmann, 2000). The dashed lines show the profiles for the "cold" (T_{150} =600°C, T_{500} =900°C, T_{1000} =1100°C) and "hot" (T_{150} =700°C, T_{500} =1100°C, T_{1000} =1300°C) models.

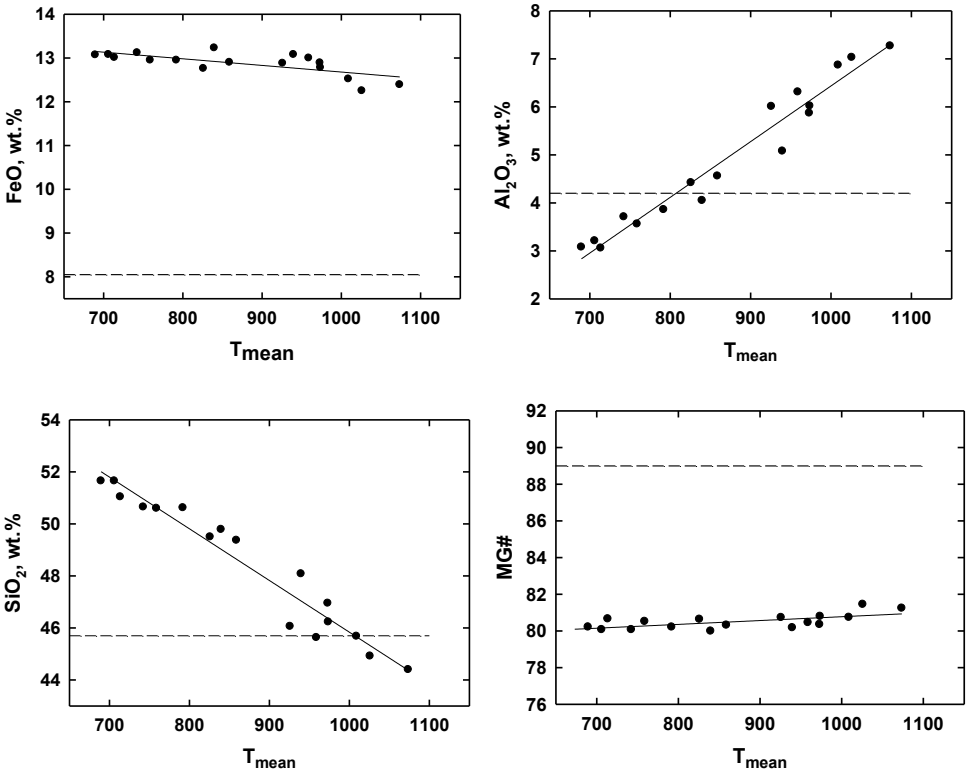

Fig. 2. The contents of FeO, Al_2O_3, SiO_2 and MG# in the silicate portion of the Moon (mantle + crust) calculated from the given geodetic and seismic data (Table 1) as a function of mantle temperature (T_{mean}). The dots represent the mean values of the frequency distributions of the oxide concentrations and MG# under the assumption of a normal distribution. The dashed line shows the parameters for BSE (Ringwood, 1977; McDonough, 1990, Dauphas et al., 2014).

Results According to (1-3), T_{mean} values are in the range of 690-1075°C and can be used as an informative parameter for estimating the effect of temperature variations on the concentrations of the main rock-forming oxides FeO, Al_2O_3, SiO_2 and MG# in the silicate Moon (mantle + crust) (in Fig. 2). In terms of T_{mean}, all thermal models can be conditionally divided into "cold" ones with T_{mean} ~ 690-860°C and "hot" ones with T_{mean} ~ 925-1075°C.

The abundance of refractory oxides in lunar rocks, depending on the thermal state can be divided into two different groups. Al_2O_3 of the cold (earth-like) BSM models (3.0-4.6 wt.%) is consistent with the previous estimates of 3.6-4.5% Al_2O_3 for the Moon (Khan et al., 2007, Kronrod, Kuskov, 2011,

etc.) and are close to 4-4.5 wt% Al_2O_3 for BSE (Dauphas et al., 2014; McDonough WF, 1990). The hot (non-terrestrial) BSM models are substantially enriched with Al_2O_3 ~ 5.1-7.3% by weight (Al_2O_3 ~ 1.2 - 1.7 × BSE) compared to BSE and close to the lunar values of ~ 6% Al_2O_3 from geochemical and geophysical data (Taylor, 1982, Kuskov et al., 2014, Longhi, 2006).

On the other hand, regardless of the temperature distribution of C (FeO), C (MgO), and MG # in the silicate Moon are in the narrow range of 12.2-13.2 wt% FeO, MG # 80-81, 5 (Figure 2) and 29.5-30.5% by weight MgO and are weakly dependent on the thermal state. The values obtained is consistent with other estimates of 12-13% FeO (Khan et al., 2007, Kronrod, Kuskov, 2011, Taylor, 1982), which are 1.5 times higher for BSE (FeO ~ 8%) (Dauphas et al., 2014; McDonough, 1990). MG # estimate (Figure 2) is consistent with most petrological and geophysical estimates (Khan et al., 2007, Kronrod, Kuskov, 2011; McDonough, 1990 and others), but less MG # 85 (McDonough, 1990), and significantly less than MG # 89 for BSE (Dauphas et al., 2014; McDonough, 1990, Ringwood, 1977). This means that for all possible temperature distributions, the silicate fraction of the Moon is enriched in FeO and depleted in MgO relative to BSE.

Thus, for the entire temperature region considered (Fig. 1), the silicate fraction of the Moon is enriched in FeO and depleted in MgO relative to BSE (Fig. 2). Most geochemical and geophysical assessments on these criteria indicate a fundamental difference in the chemical composition of the silicate part of the Moon and the Earth, which rejects the possibility of Moon's forming from the material of the primitive mantle of the Earth.

Acknowledgments This work was supported in part by the Russian Foundation for Basic Research (RFBR) under Grant 18-05-00225 and 17-35-50099 мол_нр, Program 17 of the Presidium of the Russian Academy of Sciences.

References:

Dauphas N., Burkhardt C., Warren P. H., Fang-Zhen T. // Phil. Trans. R. Soc. A. 2014. V. 372, 20130244.
Gagnepain-Beyneix J., Lognonné P., Chenet H., Lombardi D., Spohn T. // Phys. Earth Planet. Inter. 2006. V. 159. P. 140-166.
Khan A., Connolly, J.A.D., Maclennan J., Mosegaard K. // Geophys. J. Int. 2007. V. 168. P. 243–258.
Kronrod V.A., Kuskov O.L. // Izv. Phys. Solid Earth. 2011. V. 47. P. 711-730.
Kuskov O.L., Kronrod V.A., Kronrod E.V. // Phys. Earth Planet. Inter. 2014. V. 235. P. 84-95.
Longhi J. // Geochim. et Cosmochim. Acta. 2006. V. 70. P. 5919–5934.
McDonough W.F. // Earth Planet. Sci. Lett. 1990. V. 101. P. 1-18
Ringwood A.E. // The Moon. 1977. V. 16. P. 389–423.
Taylor S.R. Planetary Science: A Lunar Perspective. LPI. Houston. TX. 1982. 481 pp.
Williams J.G., Konopliv A.S., Boggs D.H., Park R.S., Yuan D-N., Lemoine F.G., Goossen S., Mazarico E., Nimmo F., Weber R.C., Asmar S.W., Melosh H.J., Neumann G.A., Phillips R.J., Smith D.E., Solomon S.C., Watkins M.M., Wieczorek M.A., Andrews-Hanna J.C., Head J.W., Kiefer W.S, Matsuyama I., McGovern P.J., Taylor G.J., Zuber M.T. // J. Geophys. Res.: Planets. 2014. doi: 10.1002/2013JE004559

Kuyunko N.S., Skripnik A.Ya., Alexeev V.A. Thermoluminescent research of samples-finding uncertainty genesis.

Vernadsky Institute of Geochemistry and Analytical Chemistry RAS, Moscow (AVAL37@mail.ru),

Abstract. Information on the thermoluminescent properties of the finds (the intensity of the glow, the position of the maximum and the characteristic features of the glow curve) in comparison with the analogous characteristics of meteorites of different chemical classes were used by us to determine the possibility (or impossibility) of the extraterrestrial origin of the found object. The natural and induced in laboratory thermoluminescence measurements of seven samples of unknown origin were performed to determine the possibility of their extraterrestrial origin.

Keywords: *meteorites, thermoluminescence method, identification of extraterrestrial substance.*

Introduction. Thermoluminescence (TL) is one of the most common methods for studying the substance of meteorites (Sears, 1988). There are two types of TL: natural (TL_{nat}), stored by meteorite in outer space, and induced (TL_{ind}), induced from an external source of ionizing radiation in the laboratory. TL_{nat} measurements are used to estimate the orbits of meteorites (Alexeev et al., 2012), their terrestrial ages, shock metamorphism analysis, and identification of paired samples of meteorites-finds (Sears, 1988). TL_{ind} reflects the changes in the crystalline structure of feldspar as a result of thermal metamorphism induced by impact. Measurements of TL_{ind} are successfully used for studying metamorphism and shock-thermal history of meteorites (Alexeev et al., 2008; 2012). The thermoluminescence method was also used (Kuyunko et al., 2016a; 2016b) to identify extraterrestrial matter. The identification of meteorites falling to the Earth does not cause difficulties in the presence of a melting crust, a characteristic surface relief or a crater at the site of the find. However, often the origin of the find is uncertain and only the involvement of precision methods of analysis makes it possible to establish the nature of the substance. For example, a comparative analysis of the content of cosmogenic and natural radionuclides measured on a gamma spectrometric complex without destroying a sample can with a high degree of reliability answer the question of its terrestrial or cosmic origin (Alexeev, Gorin, 2004). Information on the thermoluminescence properties of the finds (the intensity of the glow, the position of the maximum and the characteristic features of the glow curve) in comparison with the analogous

characteristics of meteorites of different chemical classes were used by us to determine the possibility (or impossibility) of the extraterrestrial origin of the found object.

In this investigation, thermoluminescence measurements of the natural and laboratory-induced by X-ray radiation of seven finds from the GEOCHI meteorites collection of the Russian Academy of Sciences were made to determine the possibility of their extraterrestrial origin.

Measurement procedure. For the study, samples of 0.7-1.0 g were crushed in a jasper mortar under a layer of ethyl alcohol. The magnetic fraction was separated by a hand magnet after air drying for 24 hours. Three samples of 2 mg each were prepared from the non-magnetic fraction of each sample by the quartering method. Each sample was placed in a 6 mm diameter beryllium foil dish and evenly distributed on the bottom with an acetone drop under the binocular. The solvent was removed by air-drying for 24 hours.

Thermoluminescence was recorded on a modified GEOCHI unit. The interface made on the basis of the L154 board made it possible to register the photomultiplier current (FEU-93) on the computer and the sample heating temperature. Discreteness of registration was 1°C. Connecting the installation to the computer increased the sensitivity of measurements and the accuracy of reproduction of the luminescence curves. The performed TL measurements showed that the peak temperature on the luminescence curve is reproduced with an error of not more than 1°C. The average value of three measurements was used to calculate the TL parameters.

Results. The intensity of natural and X-ray induced thermoluminescence in the laboratory was determined from the area under the peak of the glow curve in the temperature range 50-350°C. All TL values were determined in relative units by normalization to the corresponding TL values for chondrite Dhajala H3.8. Characteristics and data of TL-studies of finds used in this work are shown in Fig. 1 and in the table.

From these data it follows that both the value of natural TL (TL_{nat}) and the sensitivity to the accumulation of thermoluminescence (TL_{ind}) vary over a wide range of values – up to three orders of magnitude. At the same time, for most samples of indeterminate origin, the characteristics of TL curves (position of the peak maximum, width, shape of TL curve) differ significantly from the corresponding characteristics of Dhajala chondrite and other meteorites. It should be noted that in the interval 50-350°C, the spectra of natural thermoluminescence of all the samples studied do not have a clearly pronounced maximum – the intensity of TL_{nat} emission increases with increasing temperature (see Fig. 1).

Earlier, we (Kuyunko et al., 2016a, 2016b, 2017) investigated thermoluminescence properties of 47 meteorites of various chemical classes, and a region with positive correlation dependence was identified by the ratio of TL_{nat} and TL_{ind}. Most meteorites hit this area. The exception was meteorites with a small perihelion of the orbit, which caused the loss of TL_{nat} due to heating by the Sun, as well as chondrites found in deserts that lost TL_{nat} due to partial annealing due to their contact with heated sand. The ratios of TL_{nat} and TL_{ind} values for meteorites and samples of uncertain genesis, investigated both in this work and earlier (Kuyunko et al., 2016a) shows in Fig.2. Five of the seven samples are outside the meteorite zone, along with the previously measured pseudometeorites, and uniquely have a terrestrial origin.

Samples P15 and P25 are located on the boundary of meteorites and pseudometeorites (Fig. 2). They are characterized by higher values of the intensity of TL_{nat} and TL_{ind}. However, the shape of the spectrum of natural thermoluminescence (Fig. 1) does not allow them to be attributed to objects of cosmic origin. Higher values of TL_{nat} can be due to the technogenic origin of these samples, and high values of TL_{ind} – a significant content of feldspar.

Table. Normalized to chondrite Dhajala H3.8 values of natural (TL_{nat}) and induced (TL_{ind}) thermoluminescence in the finds of indeterminate origin.

Sample	Characteristic of sample	TL_{nat}	TL_{ind}
P15	Weathered granite (Leningrad region, Lomonosov district, 2017)	1.935	3.064
P23	Vitreous silicate slag (Moldavia, 2016)	0.004	0.015
P25	Type of gabbro-diabase (Yamalo-Nenets AO, found at a depth of 2.5 m in permafrost, 2016)	0.035	0.065
P31	Type of diabase. Oxidized. (Moscow Region, 2016)	0.005	0.001
P94	Type of diabase. Oxidized. (Moscow Region, 2016)	0.003	0.044
P97	Gabbroide type with oxidized crust (Podmoskovye, 2017)	0.010	0.008
PS	Aluminosilicate slag (Samara neighborhood, 2003)	0.009	0.004

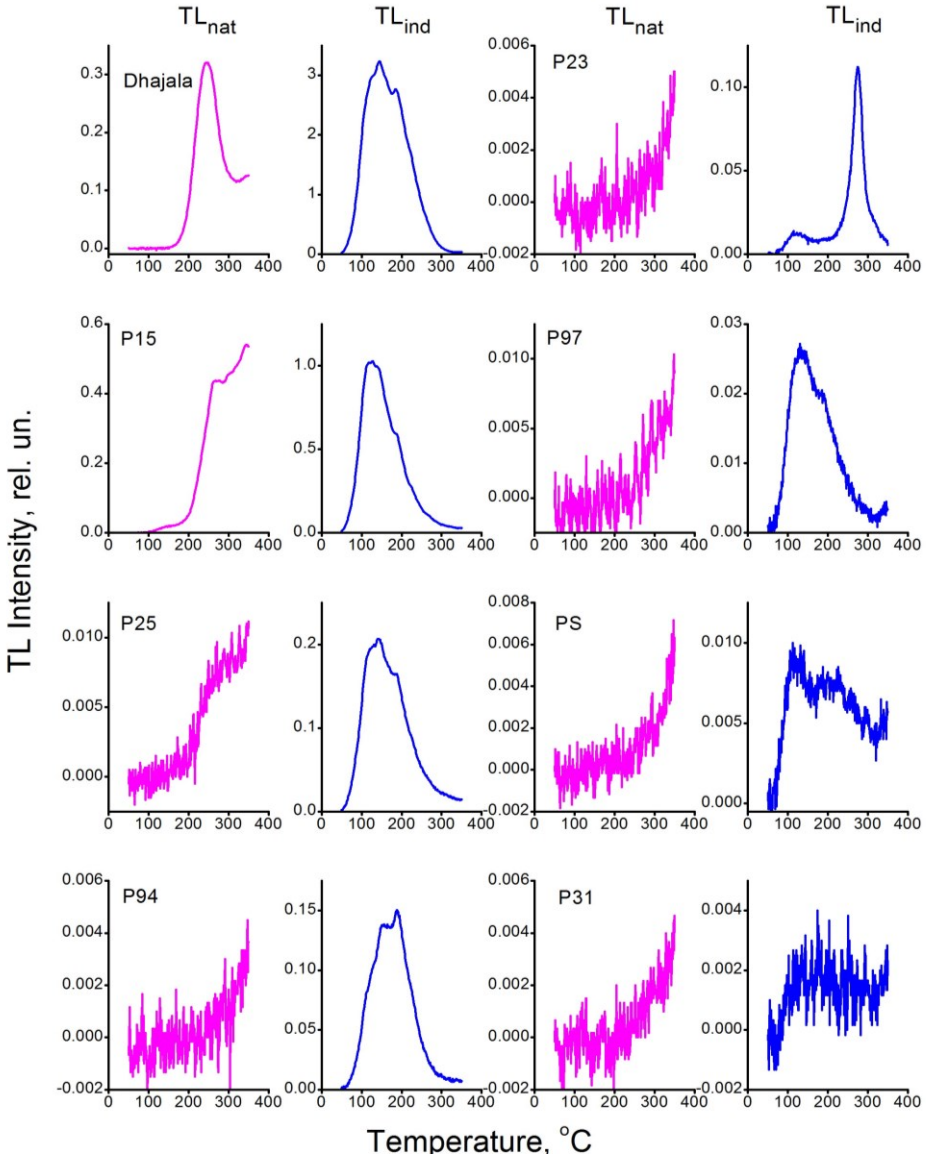

Fig. 1. TL glow curves for chondrite Dhajala H3.8 and samples of indeterminate genesis. The designations of the samples correspond to those in the table.

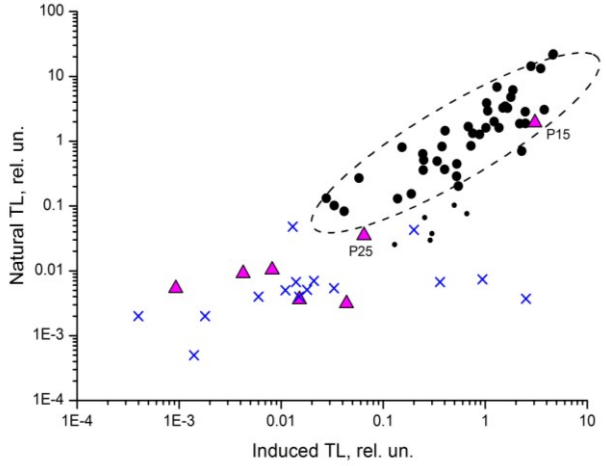

Fig. 2. The ratio of TL_{nat} and TL_{ind} in chondrites (circles) and in samples of indeterminate genesis (crosses - according to (Kuyunko et al., 2016a), triangles - new data. Symbols of small size refer to chondrites with possible losses of natural TL.

Conclusions. The thermoluminescence method was used to establish the possibility of extraterrestrial origin of the found objects. Thermoluminescence measurements of the natural and laboratory-induced by X-ray emission of seven specimen finds suggest that they are all terrestrial rocks. Technogenic origin is supposed for two samples.

The work is partially supported by the Program No. 28 of the fundamental research of the Presidium of the Russian Academy of Sciences.

References:

Alexeev V.A., Gorin V.D. (2004) Identification of Cosmic Matter from the Ratio of Contents of Cosmogenic and Natural Radionuclides // Solar System Research.–V. 38, No. 2.–P. 93-96

Alexeev V.A., Gorin V.D., Ivliev A.I., Kashkarov L.L., Ott U., Sadilenko D.A., Ustinova G.K. (2012) Integrated Study of the Thermoluminescence, Noble Gases, Tracks, and Radionuclides in the Fresh-Fallen Ash Creek L6 and Tamdarkht H5 Chondrites // Geochemistry International.–V. 50, No. 2.–P. 105–124.

Alexeev V.A., Gorin V.D., Ivliev A.I., Kashkarov L.L., Ustinova G.K. (2008) Recently Fallen Bukhara (CV3) and Kilabo (LL6) Chondrites: A Parallel Study of Luminescence, Tracks, and Cosmogenic Radionuclides // Geochemistry International.–V. 46, No. 9.–P. 849–866.
Sears D.W.G. (1988) Thermoluminescence of meteorites: Shedding light on the cosmos // Nucl. Tracks Radiat. Meas.–V. 14, № 1/2.–P. 5-17.
Kuyunko N.S., Skripnik A.Y., Alexeev V.A. (2016a) Application of the thermoluminescent method for identification of extraterrestrial matter // Proceedings of the All-Russian Annual Seminar on Experimental Mineralogy, Petrology and Geochemistry. Moscow, April 19-20, 2016.Moscow: GEOCHI RAS.–P. 98-99 *(in Russian).*
Kuyunko N.S., Skripnik A.Y., Alexeev V.A. (2016b) Thermoluminescence as a method of identification of extraterrestrial matter // Proceedings of the XVII International Conference "Physicochemical and Petrophysical Studies in the Sciences of the Earth", September 26-28, 2016. Moscow: IGEM RAS.–P. 169-171 *(in Russian).*
Kuyunko N.S., Kalinina G.V., Alexeev V.A. (2017) Thermoluminescent and track studies of meteorites Ausson L5 and Doroninsk H6 //Proceedings of the XVIII International Conference "Physicochemical and Petrophysical Studies in the Sciences of the Earth", October 2-6, 2017. Moscow: IGEM RAS.–P. 149-152 *(in Russian).*

Lavrentjeva Z.A., Lyul A.Yu. The unequilibrated Adhi Kot EH4 enstatite chondrite: the peculiarities of trace element composition.

V.I. Vernadsky Institute of Geochemistry and Analytical Chemistry RAS, Moscow (lavza@mail.ru)

Abstract. Based on the study of the features of lithophile and siderophile trace element distributions in the accessory minerals from Adhi Kot EH4 enstatite chondrite a conclusion has been made that these peculiarities probably result from mixing effects of nebular fractionation, thermal metamorphism and shock.

Keywords: *mineral fractions; trace element distributions; enstatite chondrites.*

Enstatite chondrites (EC) are thought to have formed in highly reducing environment. This inference is supported by the high Mg/(Mg + Fe) of olivine and pyroxene, presence of Si in Fe,Ni metal, and occurrence of typically lithophile elements, such as Ca, Mg, Mn and K, in sulfide minerals in enstatite chondrites [Weisberg et al., 2009]. The oxygen fugacity (fO_2), inferred typical EC mineral assemblages (pure En, Si-bearing metal, Mg-sulfides) are several orders of magnitude below those of a system of solar composition [Grossman et al., 2008]. EC are proposed to have formed in the inner regions of the disk, in an environment that was highly reducing (i.e. low oxygen fugacity), in contrast to the oxidizing conditions seen in many other meteorite groups [McSween, 1988; Brearley, 1998]. EC classified into the high-siderophile group EH and lo*w-siderophile group EL [Sears et al., 1982]. Some* EH chondrites and must EL6 chondrites are impact-melt breccias. Relative to ordinary chondrites and most carbonaceous-chondrite groups, EC are enriched in volatile and moderately volatile elements. This work reports data on the composition of mineral fractions on the Adhi Kot EH4 enstatite chondrite which are considered from the viewpoint of cosmochemical history of EH chondrites. The Adhi Kot EH4 enstatite chondrite breccia consist of silica-rich clasts (12+5 vol %), chondrule-rich clasts (55+10 vol %) and matrix (35+10 vol %). The silica – rich clasts are new kind of enstatite chondritic material, which contains more cristobalite (18 – 28 wt%) than enstatite (12 – 14 wt%), as well as abundant niningerite and troilite [Rubin, 1983]. Cristobalite occurs as anhedral grains (<30 μm) in both matrix and clasts. Large rounded grains of cristobalite inside kamacite clasts are associated with clinoenstatites. Pyroxenes are set in a fine-grained matrix and in the metal clasts enclosed euhedral laths and also subhedral to anhedral grains [Leitch, 1982].

Samples and methods. We studied following fractions of accessory minerals: cristobalite (SiO_2), olivine $(Mg,Fe)_2[SiO_4]$, yellow pyroxene $Mg_2[Si_2O_6]$, sphalerite (ZnS), osbornite (TiN) and schreibersite (Fe,Ni,Co)P from unequilibrated Adhi Kot EH4. The mineral fractions were selected by particle – size analysis and handpicking under microscope. The elemental composition of fractions was analyzed at the Central Laboratory of GEOKHI RAS using optimized version of neutron–activation analysis developed for analyzing extraterrestrial material [Kolesov, 2001].

Results and discussion: Under consideration are peculiarities of trace element composition of accessory minerals extracted from unequilibrated Adhi Kot EH4 enstatite chondrite. The analysis of the chemical composition of the obtained data showed that:

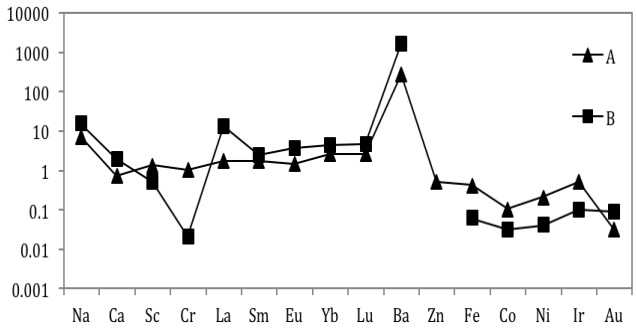

Fig.1. CI chondrite–normalized of trace element abundance patterns in cristobalite from Adhi Kot EH4 enstatite chondrite: 1 – fraction A ("*fine - grained*"cristobalite); 2 – fraction B ("*coarse-grained*"cristobalite).

In cristobalites A and B (Fig 1) are large variations in compositions of lithophile and siderophile elements.

Cristobalite A ("*fine - grained*" fraction) is enriched in REE with the prominent predominance of HREE $[(Lu/La)_A /(Lu/La)_{CI}] = 1.5$ and negative Eu anomalie $[(Eu/Sm)_A/ (Eu/Sm)_{CI}] = 0.8$. Cristobalite B ("*coarse-grained*") is enriched in LREE $[(La/Lu)_B/(La/Lu)_{CI}] = 2.9$ and have positive Eu anomaly $[(Eu/Sm)_A/ (Eu/Sm)_{CI}] = 1.5$. Lanthanum show fractionation to samarium with enrichment La in cristobalite B - $[(La/Sm)_B]/[(La/Sm)_A] = 5.4$. The $[(Ir/Au_{A,B} / (Ir/Au)_{CI}]$ ratio in cristobalites A, B varies from 1.1 to 16.6. This fact supports the opinion that, the main processes controlling of composition cristobalites was nebular fractionation. Cristobalite A ("*fine - grained*" fraction has the ratio $[(Ir/Ni)_A / (Ir/Ni)_{CI}] / [(Au/Ni)_A / [(Au/Ni)_{CI}] = 16.6$, more than cosmic (cosmic is 3.44). The superabundant in Ir to Au witness as to formation of "*fine - grained*" cristobalite by agglomeration of components enriched in refractory metal (Ir) with components enriched in no refractory metal (Au).

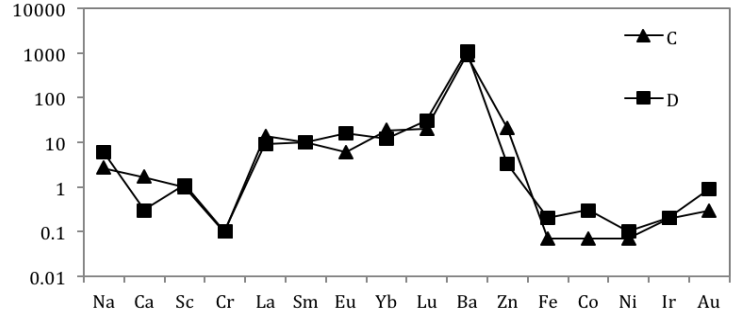

Fig.2. CI chondrite–normalized of trace element abundance patterns in olivine from Adhi Kot EH4 enstatite chondrite: 1 – fraction C (light-green olivine); 2 – fraction D (dark-green olivine).

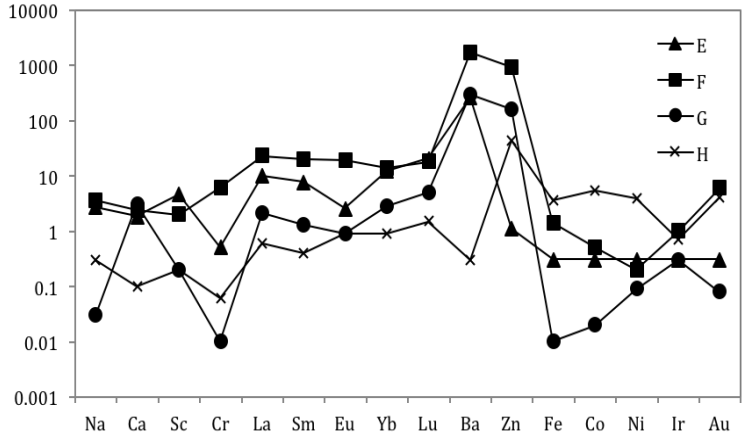

Fig.3. CI chondrite–normalized of trace element abundance patterns in mineral fractions from Adhi Kot EH4 enstatite chondrite: 1 – fraction E (yellow pyroxene); 2 – fraction F (sphalerite); 3 – fraction G (osbornite); 4 – fraction H (schreibersite).

The Ca content in the *light-green* olivine (fraction C) is an order of magnitude higher than that in the *dark-green* olivine (fraction D) (Fig 2.). The siderophile element contents in low-calcium olivine higher than in high-calcium olivine. Perhaps, that the Ca content is indicator of the thermal history of olivines. The fractions C and D are enriched in REE with the prominent predominance of heavy REE $[(Lu/La)_{C,D}/(Lu/La)_{CI}] = 1.4$ and 3.3, respectively, with negative and positive Eu anomalies $[(Eu/Sm)_{C,D} / (Eu/Sm)_{CI}] = 0.8$ and 1.6, respectively. The light-green olivine are characterized more high ration of lanthanium to samarium $[(La/Sm)_C / (La/Sm)_{CI}] = 1.4$, than dark–green olivine – 0.9. The light-green olivine and dark-green olivine D are characterized by LREE depletion in with regard to HREE $[(La/Lu)_{C,D} /(La/Lu)_{CI}] = 0.7$; 0.3 respectively.

Yellow pyroxene (fraction E) (Fig. 3) is the high abundances of scandium relative the calcium in comparison with their content in other accessory minerals. Pyroxene is enriched in REE with the prominent predominance of HREE $[(Lu/La)_E/(Lu/La)_{CI}] = 2.0$ and lowest negative Eu anomalie $[(Eu/Sm)_E/ (Eu/Sm)_{CI}] = 0.3$. One of the feature of yellow pyroxene is characterized by CI chondrite ratio of siderophile elements with different condensation temperature $[(Fe, Co, Ir, Au / Ni)_E] / [(Fe, Co, Ir, Au / Ni)_{CI}] = 1.0$, which indicates the even distribution Fe, Co, Ir, Au, Ni in this fraction.

Sphalerite (fraction F) (Fig. 3) are enriched in refractory lithophile Ca, Sc, REE, Ba and non-refractory Na. One of the feature of sphalerite is characterized the high contents Cr, Au и REE in comparison with their content in other accessory minerals. Sphalerite is enriched in REE with the prominent predominance of HREE $[(Lu/La)_F/(Lu/La)_{CI}] = 2.0$ and negative Eu anomalie $[(Eu/Sm)_F/ (Eu/Sm)_{CI}] = 0.95$. Other feature of

element distribution in the sphalerite is the high abundances Co, Ir and Au relative to Ni - $[(Co,Ir,Au/Ni)_F/(Co,Ir,Au\ /Ni)_{CI}]$ = 2.5; 5.0; 12, respectively.

One of the features of element distribution in *osbornite* (fraction G) (Fig. 3.) is the low contents of Cr, Fe , Ni, Co and Au relative to those in other accessory minerals. The osbornite have the highest refractory siderophile Ir abundance relative to non-refractory siderophile Ni, Co и Au. Other feature of element distribution in osbornite is the high abundance Ca relative to Sc - $[(Ca/Sc)_G/(Ca/Sc)_{CI}]$ = 15.5; Ni relative to Co - $[(Ni/Co)_G/(Ni/Co)_{CI}]$ = 4.5; Ir relative Au - $[(Ir/Au)_G / (Ir/Au)_{CI}]$ = 3.7 and the low abundance Na relative K – $[(Na/K)_G/(Na/K)_{CI}]$ = 0.06; Fe relative Ni - $[(Fe/Ni)_G/(Fe/Ni)_{CI}]$ = 0.09.

Schreibersite (fraction H) (Fig. 3) are enriched in siderophile Fe, Ni, Co, Au and depleted in Ir. In schreibersite from Adhi Kot EH4 have observed negative Sm anomaly where it is associated with negative Eu and Yb anomalies. The similar distributions of Sm, Eu and Yb have been observed in enstatite from unequilibrated enstatite chondrites [Hsu, 1998]. Perhaps, the fraction H has enstatite grains. One of the feature of schreibersite is the fact that the ytterbium to europium ratio corresponds to that in CI chondrites $[(Yb/Eu_H) / (Yb/Eu_{CI})]$ = 1.0.

The enrichment factors of *siderophile* Fe, Ni, Co, Ir and Au in all fractions are less than 1, with exception of sphalerite (Fig. 4). All accessory minerals are enriched in moderately volatile As, Sb and Cu, the enrichment indicate that impact melting events are in the present case the most likely cause of the redistribution of this elements. *Cristobalites* A and B, *yellow pyroxene* (E) and *osbornite* (G) are enriched in refractory Ir relative to more volatile Au - $(Ir/Au)_{A,B,E,G}/(Ir/Au)_{CI}$ = 1.0 - 16.6. This fact supports the opinion that, the main processes controlling of composition these accessory minerals was nebular fractionation. The distribution of these elements (0.17 – 0.66) in olivines (C, D), sphalerite (F) and schreibersite (H) indicate that was fractionation in situ probably result from thermal metamorphism.

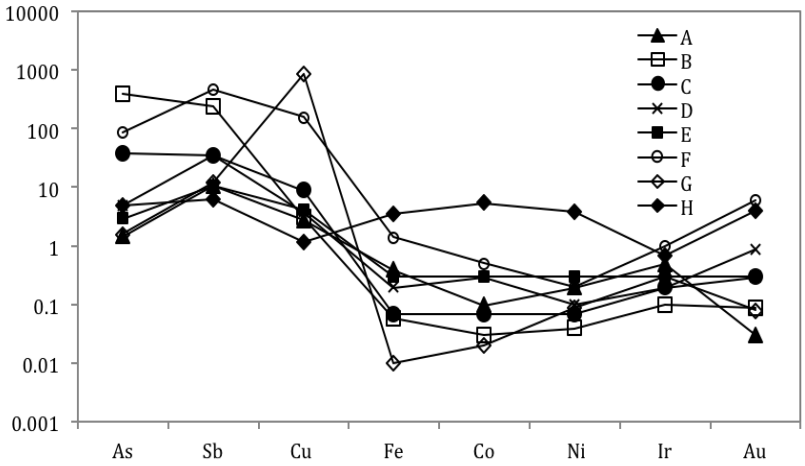

Fig.4. CI chondrite–normalized of trace element abundance patterns in mineral fractions from Adhi Kot EH4 enstatite chondrite: 1 – fraction A ("*fine - grained*"cristobalite); 2 – fraction B ("*coarse-grained*"cristobalite). 3 – fraction C (light-green olivine); 4 – fraction D (dark-green olivine); 5 – fraction E (yellow pyroxene); 6 – fraction F (sphalerite); 7 – fraction G (osbornite); 8 – fraction H (schreibersite).

Conclusions.

Based on the study of the features of lithophile and siderophile trace element distributions in the accessory minerals from Adhi Kot EH4 enstatite chondrite a conclusion has been made that these peculiarities probably result from mixing effects of nebular fractionation, thermal metamorphism and shock.

References:

Brearley A. J. and Jones R.H. Chondritic meteorites. In : Papike J.J. (Ed.). // Reviews in mineralogy, planetary materials. - 1998. - V. 36. - Mineralogical society of America.

Grossman, L., Beckett, J.R., Fedkin, A.V., Simon, S.B., Ciesla, F.J. Redox conditions in the solar nebula: observational, experimental, and theoretical constraints. // Rev. Mineral. Geochem. - 2008. - V.68. - P. 93 – 140.

Hsu W., Crozaz G. Mineral chemistry and the origin of enstatite in unequilibrated enstatite chondrites. //Geochim. Cosmochim. Acta. - 1998. - V.62. - P. 1993 – 2004.

Kolesov G. M., Shubina N.V., Lyul A.Yu. Optimizing instrumental neutron activation analysis of extraterrestrial materials: fragments of lunar rocks, meteorites, chondrules and ultrarefractory inclusions. // J. Anal. Chem. - 2001. - V.56. - P. 1169 – 1172.

Leitch C.A., Smith J.V. Petrography, mineral chemistry and origin of type I enstatite chondrites. //Geochim. Cosmochim. Acta. - 1982. - V.46. - P.2083 – 2097.

McSween H.Y., Sears D.W.G., Dodd R.T. Thermal metamorphism. In: Kerridge J. F and Matthews M. S.(Eds). // Meteorites and the early solar system - 1988. – The University of Arizona Press. Tucson - P. 102 - 113.

Rubin A.E. The Adhi Kot breccia and implications for the origin of chondrites and silica-rich clasts in enstatite chondrites. // Earth Planet. Sci. Lett. - 1983. - V.64. - P. 201 – 212.

Sears D.W., Kallemeyn G. W., Wasson I. T. The compositional classification of chondrites II. The enstatite chondrite groups. // Geochim. Cosmochim. Acta . - 1982. - V. 46. - P. 597 - 608.

Weisberg M. K., Ebel D. S., Connolby Ir., Kita N. T., Ushikubo T. Petrologic – geochemical study of chondrules

in enstatite chondrites. //Lunar Planet. Sci. Conf. XL. - 2009. - # 1886.

Lyul A.Yu., Lavrentjeva Z.A. Lithophile element fractionations in the fine-grained fractions of enstatite chondrites. UDC 542.42

Vernadsky Institute of Geochemistry and Analytical Chemistry RAS, Moscow (ajull@mail.ru)

Abstract. Obtained by the INAA data on the lithophile element contents of the different volatility in a fine-grained fraction of enstatite chondrites EH4 (Abee, Adhi Kot) and EL6 (Atlanta, Pilistfer) groups are discussed. Significant differences in the lithophile element contents in this fraction and in bulk chondrites are revealed. It was found that the fine-grained fractions of enstatite chondrites are enriched in Na, Ca and REE relative to their bulk contents. Simultaneous enrichment in these elements is due to their entry into rare accessory silicate minerals such as plagioclase and tridymite (Na, partially Ca and REEs) and oldhamite (REEs). In despite on the distinction in shock and thermal histories of the EH and EL chondrites, the similarity in the trends of the abundance patterns of lithophile elements in their fine-grained fractions indicates that the lithophile element contents in this chondritic fractions are mainly depend on their mineralogical composition.

Keywords: *enstatite chondrites, fine-grained fraction, lithophile elements, fractionation*

Introduction. The fine-grained, the least thermally altered fraction is both a source of information about the processes of meteorite formation and also a sensitive indicator of the secondary processes occurring in their parental bodies (Scott, 2007). Consequently, the data on the chemical composition of this fraction characterize the processes of primary fractionation of elements in a protoplanetary disc and their secondary redistribution between the individual components of chondrites in their parent bodies. As was shown earlier [Lyul et al., 2017], from the data on the siderophile element contents in the fine-grained fraction of the enstatite chondrites follows that secondary processes in the chondritic parent bodies lead to redistribution of elements between metal and silicate and to a partial melting of the metal. A peculiarity of the enstatite chondrite compositions is the presence in them of numerous sulfides formed by lithophile elements. Consequently, the observed trends of lithophile element fractionations in fine-grained fractions can be a result of their redistribution between the main components of chondrites under shock and (or) metamorphic processes as well as a peculiarity of the mineral composition of the enstatite chondrites. To estimate the influence of secondary processes on the chemical composition of this component of chondrites, data on the lithophile element contents of different volatility in the fine-grained fraction of the enstatite chondrite EH4 (Abee, Adhi Kot) and EL6 (Atlanta, Pilistfer) groups were obtained. The non-magnetic fine-grained fraction was separated out by repeatedly crushing the matter of chondrite, settling and periodic scattering on sieves of different sizes with the subsequent sedimentation of the fraction <45 μm. The data on the lithophile element contents in the isolated fractions obtained by INAA method are given in the table.

Results and discussion

It is possible to note the some features in composition of this component from the enstatite chondrites of different chemical groups: a) lack of noticeable differences in the Ga content in the fine-grained fraction of EH and EL chondrites due to its preferential entry into the Fe-Ni phase; b) lack of differences in the content of Cr in fine-grained fractions of chondrites of each group and a significant enrichment of the EL6 chondrite fractions with this element; In the contrary, there are significant differences in the contents of refractory La, Sm. Yb, Ca and moderately volatile Na in this chondritic fractions. It also can be noted that there is a correlation between the Ca, Na, and La contents in these fractions, possibly due to their partial entry into the same minerals, such as plagioclase and tridymite [Keil, 1968].

For more complete characterization of the fine-grained fraction composition, the data on the content of lithophile elements in this chondritic component and in the bulk chondrites of the corresponding chemical groups are compared (Fig. 1).

Table. Content of the lithophile elements (μg/g), Fe and Se in fine-grained fractions of EH and EL chondrites.

	Abee EH4	Adhi Kot EH4	Atlanta EL6	Pilistfer EL6
Sc	7.4	5.5	8.7	10
La	0.34	0.61	0.33	0.71
Sm	0.19	0.22	0.19	0.31
Yb	0.18	0.29	0.16	0.42
Ca, %	1.7	2.4	1.4	2.8
Fe, %	14.4	7.6	10.2	9.5
Cr	4350	3470	6570	6440
Na	5240	10880	6520	12600
Se	30	22	26	44
Ga	6.9	6.8	5.1	4.9

As follow from data presented in Fig. 1, there are the remarkable differences in the lithophile contents in fine-grained fractions and bulk chondrites. So, the depletion in Fe and Ga points to a low metal content in this component of the chondrites, whereas the enrichment in Se evidenced of the presence in them a significant amount of sulphides. The observed uniform enrichment in Sc, despite the difference in their contents in fine-grained fractions of EH and EL chondrites (Table), is due to the presence of silicate minerals in the isolated fractions. The significant enrichment in Ca, La and Sm indicates the existence of the smallest grains of oldhamite that is also confirmed by the higher Sm and Yb contents in these fractions. It can also be noted that there is no difference in the relative abundance of Sc, Fe, Cr, and Ga in the fine-grained fractions of the corresponding group of chondrites. These elements are concentrated in the main silicate minerals and metal phase of chondrites.

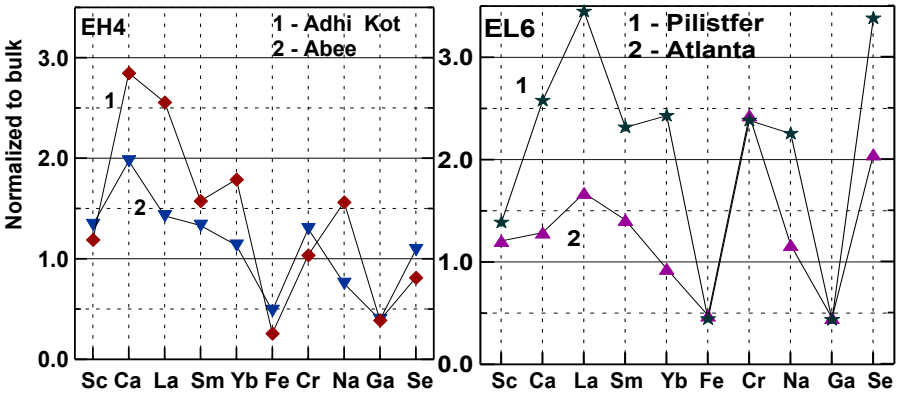

Fig. 1. The lithophile elements, Fe and Se abundance patterns of the fine-fraction normalized to the respective bulk enstatite chondrite compositions [Kong et al., 1997]. Elements are arranged in order of increasing volatility.

More detailed picture of the interelement fractionation of lithophile elements in the fine-grained fractions of chondrites that differ in both volatility and geochemical properties is shown in Fig. 2. As follows from the data in Fig. 2a,b, these chondrite fractions are depleted in Na relatively to refractory La, Sm, Ca and Sc (only in the EH chondrites). Also, there are the significant differences in the Na/Se ratios in fine-grained fractions of EL and EH chondrites due to the geochemical properties of these elements. As Na and Se are concentrated in different minerals, hence the variations in this ratio reflect the relative content of silicate minerals and sulphides in these chondritic fractions.

Variations of the La/Sm and La/Ca ratios (Fig. 2c, d) characterize the distribution features of these elements in oldhamite [Larimer et al., 1987; Chen at al, 1992]. According to their studies, several types of distribution of rare-earth elements are observed in oldhamite of the enstatite chondrites, varying from enrichment in light REE up to their depletion. In addition, oldhamite contains the significant amounts of Se (up to 50 μg/g) [Chen at al, 1992]. The low Ga/Se ratio (fig.2c, d) in the fine-grained fraction of chondrites is due to the high content of Ga in the metal up to 70 μg/g [Lavrukhina et al., 1982] confirm also the presence of selenium. The value of the Fe/Ga=1 (Fig.2d) in the fine-grained fractions of EL6 chondrites indicates to the presence of the smallest metal grains in them whereas in the EH4 fractions Ga partly is included in other minerals (Fe/Ga> 1, Fig 2c).

From the data presented in Fig. 2e,f follows that the interelement fractionation by volatility in the fine-grained fraction of the EH4 chondrites is greater than in the same fraction of more metamorphosed EL6 chondrites.

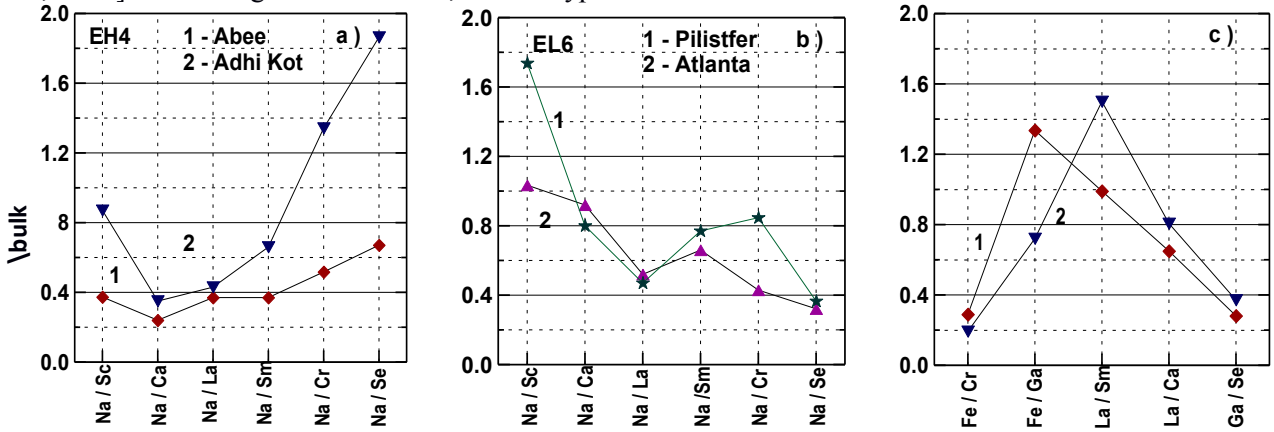

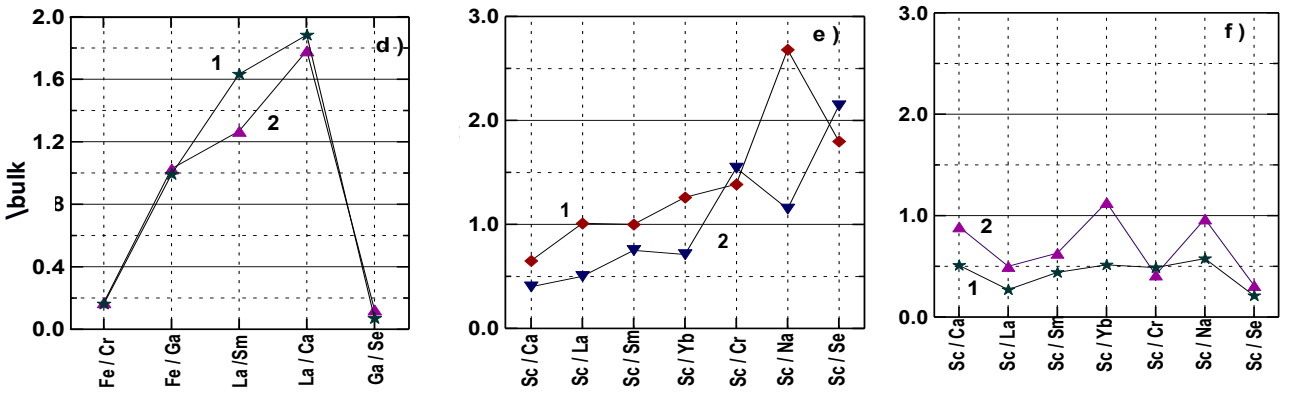

Fig. 2. Variations in the ratios of elements of different geochemical properties in the fine-grained fraction of the EH and EL chondrites normalized to the corresponding values of the bulk chondrites [Kong et al., 1997].

As also follows from Fig. 2e, f, the Sc/La, Sc/Sm and Sc/Ca ratios in fine-grained fraction are lower than the corresponding value for the bulk chondrites, which is an additional evidence of the occurrence of refractory elements in different minerals. The most important feature of the chondritic fine-grained fractions is their depletion in volatile Yb relatively to other REEs. There are two diametrically opposed hypotheses for the oldhamite formation, according to which oldhamite is formed as nebular condensate (Lodders et al., 1995) or it has an igneous origin (Hsu, 1998) .The positive anomaly in the Sc/Yb ratios (Fig. 2e,f) confirms the condensation model of the oldhamite formation in enstatite chondrites.

Conclusion. Analysis of the data on the lithophile element contents in the fine-grained fraction of enstatite chondrites shows that the secondary processes in their parent bodies did not lead to a noticeable redistribution of elements between the major components of meteorites. The observed enrichment of these fractions in REE and Ca is due to the presence in them a significant amount of the tiny oldhamite grains.

References:

Chen Y., Wang D. Pernichka E. REE and other trace element chemistry of CaS in Qingzhen (EH3) chondrite and thei origin implications // Chine. J. Space Sci. —1992. Vol. 12, № 2. — P. 129-138.

Hsu W. Geochemical and petrographic studies of oldhamite, diopside, and roedderite in enstatite meteorites // Met. Planet. Sci. — 1998. Vol. 33. — P. 291-301.

Keil K Mineralogical and chemical relationships among enstatite chondrites // J. Geophys. Res. — 1968. Vol.73. — P. 6945–6976.

Kong P., Mori P., Ebihara T.. Compositional continuity of enstatite chondrites and implications for heterogeneous accretion of the enstatite chondrite parent body // Geochim. Cosmochim. Acta. —1997. V.61. — P. 4895-4914.

Larimer J.W., Ganapathy R. The trace element chemistry of CaS in enstatite chondrites and some implications regarding its origin // Earth Planet. Sci. Lett. — 1987. Vol. 84. — P. 123-134.

Lavrukhina A.K., Lyul A.Yu., Baryshnikova G.V.. On the distribution of siderophile elements in the Fe, Ni-phase of ordinary and enstatite chondrites // Geokhimiya. — 1982. № 5. — P.645-663. *(In Russian*).

Lodders K., Fegley B. // Lanthanide and actinide condensation into oldhamite under reducing conditions // Lunar Planet. Sci. Conf. XXIII. — 1995. — P. 796-797.

Lyul A.Yu., Lavrentjeva Z.A. On the siderophile elements and selenium fractionations in a fine-grained fraction of enstatite chondrites.// Proceeding of the XVIII International conference "Physicochemical and Petrophysical Research in the Earth Sciences, October 2-7. — Moscow, 2017. — P.168-171. (*In Russian*).

Scott E.R.D.. Chondrites and Protoplanetary Disc // Ann. Rev. Earth Planet. Sci. — 2007. V. 35. — P. 577-620.

Pechersky D. M.[1] , Kazansky A.Y..[2], Markov G.P.[1] . Distribution of metallic iron particles inside basaltic lava flow UDC 523.4-36

[1]Schmidt Institute of Physics of the Earth RAS, Moscow, Russia (diamarmp@gmail.com)

[2]Lomonosov Moscow state university, Moscow, Russia (kazansky_alex mail.ru)

Abstract. The results of native iron particles distribution inside lava flow and at various distances from its eruption center are discussed on the base of basaltic rivers of Eastern Sayan and Tuva. The deposition rate of iron particles inside lava flow was calculated according the Stokes law. The estimations of iron concentration were carried out using thermomagnetic analysis. The results obtained show that the concentration of iron in the lower part of the lava flows is appreciably higher than in the upper one. The common picture of changes in iron concentration with depth inside lava flows can be significantly complicated by processes of secondary oxidation and turbulent character of lava flow.

Keywords: *lava flows; native iron; thermomagnetic analysis; Stokes law; particle deposition*

Metal iron in sedimentary rocks is generally represented by interplanetary cosmic dust, i.e. has an extraterrestrial origin. On the contrary, in igneous rocks the origin of iron is undoubtedly terrestrial i.e. has a magmatic origin. We have found the presence of native iron in mantle xenoliths from basalts of various regions, in Siberian traps; oceanic basalts and basalts of lava rivers from Siberia (Pechersky, 2015, Pechersky and others, 2017). Although the fine particles of metallic iron are widespread in the

basaltic lavas, the study of such particles is considerably hampered by conventional mineralogical methods because of their extremely low concentration. But such study is easier with the help of thermomagnetic measurements. This work is devoted to the thermomagnetic study of the distribution native iron particles inside the lava flow versus depth and at various distances from the eruption center using basaltic valley eruptions in the eastern Sayan and Tuva as an example. An estimate of the concentration and composition of native iron in basalts was carried out in the Laboratory of the Main Geomagnetic Field and Petromagnetism at the IEP RAS (Moscow) on the basis of thermomagnetic analysis (TMA) using a thermovibromagnetometer designed by N.M. Anosov and Yu.K. Vinogradov. The methodology of these studies is described in detail in previous works (Pechersky, 2015, Pechersky et al., 2017 and others).

Let us consider the behavior of metallic iron particles in a basaltic melt. According to modern concepts, metallic iron in the form of small rare particles appears in the basalt melt at a high temperature even before it's eruption onto the surface as a lava flow. This can be seen, for example, in the relatively high contents of metallic iron in volcanic bombs up to ~ $0.5x10^{-3}$%, reflecting the state of the melt at the time of the eruption.

In liquid basalt lava, heavy metal iron particles should be sinking. Let us estimate the deposition rate of iron particles for a simple case of settling a spherical iron particle in a laminar flow of liquid basaltic lava according to Stokes law:

$$V_{oc} = g d^2_p(\rho_p - \rho_c)/18\mu_c \quad (1)$$

where: V_{oc} - is precipitation rate of the particle, g - is the gravitational acceleration, d_p - is the particle diameter, , ρ_p , ρ_c - are the particle and liquid density, respectively, and μ_c - is the viscosity of the liquid medium. At the temperature of 1200°C (Yarmolyuk et al., 2003), the viscosity of lava without water is 220 Pa s, with water - 165-60 Pa s (Balkhanov, Bashkuev, 2015; Lebedev, Khitarov, 1979; Persikov, 1984). For calculation, we use: g = 10 m / s^2, d_p = 1, 10 and 100 μm, $\rho_p = 7.8\times10^3$ kg / m^3, the density of the lava is $\rho_c = 2.6\times10^3$ kg / m^3, the viscosity of the lava is μ_c = 100 Pa s. Substituting those values into formula (1), we obtain the precipitation rates of iron particles of different sizes in basaltic lava. It is known that the most common size (mode) of iron particles in both sediments and magmatic rocks is 10-20 μm, and the upper limit of size is 100 μm (Pechersky et al., 2018). Let us take for a rough estimate the limiting particle precipitation rate of 1 mm / h (Table 1).

Table 1. Precipitation rates of iron particles of different sizes in basaltic lava

(d_p)μm	V_{oC} mm/h
1	~0,0001
10	~0,01
100	~1

For iron particles with such precipitation rate it needs 21 days to sink from the flow surface to a depth of 0.5 m. How far will the lava flow away from the eruption center during three weeks? For example, lava from the volcanoes of Biliukai (eruption of 1938) and Kilauea (eruption of 1954) moved near the center of the eruption at a speed of 5-6 m / min; lava of the Great Tolbachik eruption (1975-1976) - 2 m / min (Fedotov, 1984). Far from the center, the speed of the lava is likely to be less than 1m / min, for example, the flow from the Bilyukai volcano moved more than 1 km from the center of the eruption at a speed of 0.6 m / min. In the latter case, the iron particles will descend to 0.5 m approximately 18 km from the center of the eruption.

Let's compare the results of our calculations with natural data on the example of two objects. The first object is the Zhombolok lava river in the Eastern Sayan (Fig. 1).

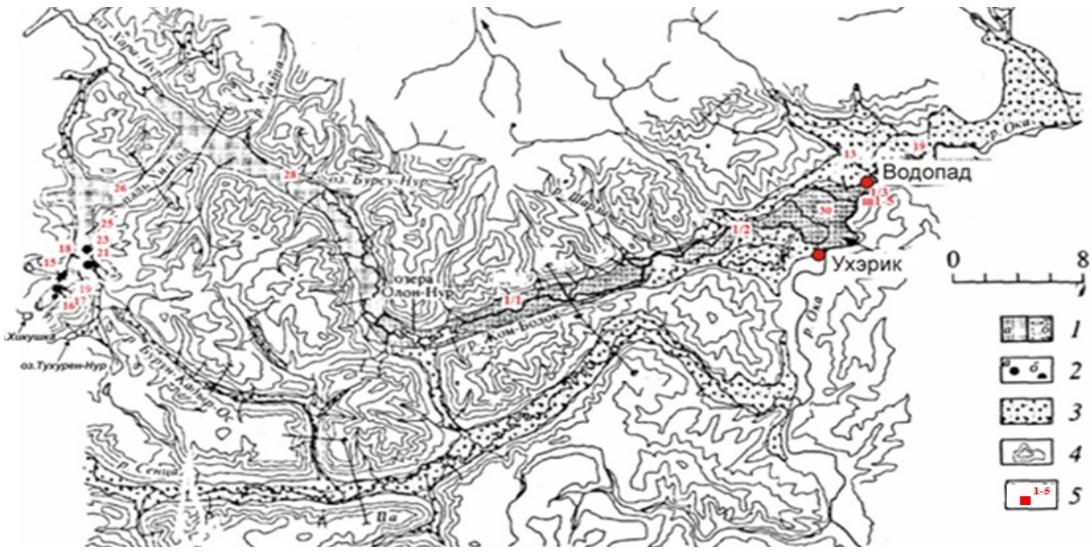

Figure 1. Sketch map of Zombolok lava river in East Sayan (Yarmoluk et al., 2003)

Legend: 1 – series of lava flows; 2 – volcanic cones; 3 – moraine; 4 – relief contours; 5 – sampling sites and their numbers.

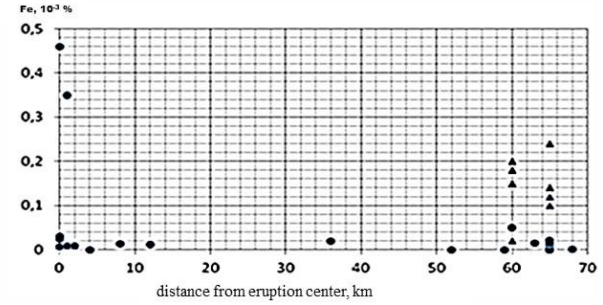

Figure 2. Generalized iron distribution in Zhombolok lava river. Triangles represent the lower parts of the flows

Table 2. The distribution of iron concentration in the different parts of Zhombolok lava flows

	Minimal	Maximal	Average
Upper part	0	$0.05x10^{-3}$%	$0.007x10^{-3}$%
Basal part	$0,02x10^{-3}$	$0,2x10^{-3}$	$0,11x10^{-3}$

As it follows from the calculated estimations the iron concentration in basalt from Zhombolok lava river, collected at a small distance from the eruption center, will be higher in the near-surface layer, on the contrary in basalt collected at a considerable distance, the maximum concentration of iron should be at the base of the flow, whereas near the flow surface the iron particles should be absent. Indeed, our direct estimates of the iron concentration show that it has the highest values in the lower parts of the lava flows farthest from the eruption center of the Zhombolok lava river (triangles in Fig. 2). Single samples with a high concentration of iron in the upper parts of the flows in the immediate vicinity of the eruption center belong only to volcanic bombs. At the end of the Zhombolok lava river (60-70 km from the center of the eruption), an appreciable part of the iron particles should be at the bottom of the flows. This can be seen in sampling sites 1-3 and 1-5 (Fig. 1), where thick succession of lava flows is exposed at confluence of the Zhombolok and Oka rivers. Here the iron concentration in the basal parts of the flows reaches 0.1-0.2 $x10^{-3}$%.

The summarized results from Zombolok lava flows are presented in table 2, from which it is evident that the lower parts of the lava flows are enriched by the iron particles in more than 10 times on average being compared with the upper parts.

Figure 3 shows the general distribution of iron concentration along the vertical section of the Zhombolok lava river: despite the scatter, the trend of increasing iron content from the top down is quite clearly visible.

According to the thermomagnetic analysis in the basaltic lavas of Zhom-Bolok, the main magnetic minerals are primary magmatic titanomagnetites (TM) with Curie temperatures of 70-80 ° C. The presence of such types of TM, along with the absence of magnetite (which is a product of secondary oxidation of TM) indicates an insignificant degree of oxidation of the initial ferromagnetics in basalt. Thus, the iron concentration in the Zhombolok basalts seems to be close to the primary original magmatic one.

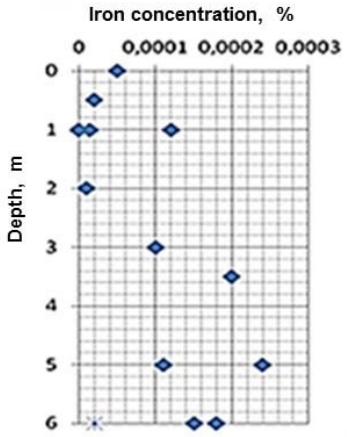

Figure 3. Generalized iron distribution inside the Zhombolok lava river with depth

The second object is another lava river in the valley of the Maly Yenisei river. It starts from the eruption center (51 ° 34' N, 97 ° 33' E) and stretches for several tens of kilometers down the river valley. Here we tested six lava flows (ME1-ME6) at a distance of 37 and 49 km from the eruption center.

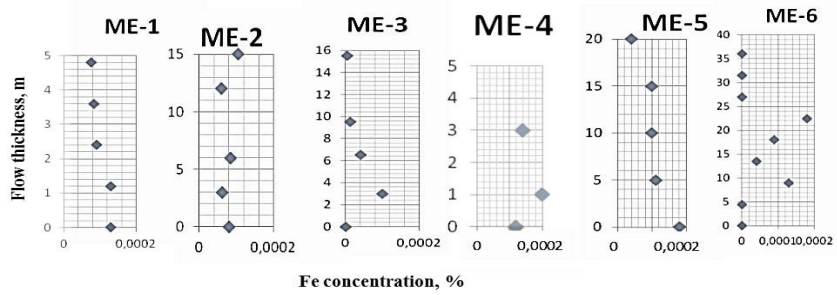

Figure 4. The iron distribution versus depth in lava flows of the Maly Yenisei river (oxidized intervals where the primary TM is absent and consequently the native iron is also destroyed have removed from the graphs).

Figure 4 shows the general tendency of an increase in the iron concentration of iron from the top downwards along the flow section, which is distinctly pronounced in ME-1, ME-3, and ME-5 flows. This tendency is partly disturbed in the flows ME-4 and ME-6, and is absent in the flow ME-2.

Conclusions. The main conclusion of the paper is the evidence of an increase in the concentration of

native iron in the lava flow from the top down, which was obtained in the sections of lava rivers of different ages in two different regions. This fact confirms the assumption of the settling of heavy iron particles in a relatively lighter lava in accordance with the Stokes law. However, this primary magmatic nature of iron distribution is complicated by secondary chemical processes, in particular oxidation. The absence of primary TM in basalt and the presence of secondary magnetite in it, appears to be the signs of oxidation processes and under such conditions the iron particles are not conserved.

Additional complications of this picture are apparently related to the fact that lava flow process differs significantly from laminar flow, as a result, we do not observe a uniform, clear increase in the iron concentration with depth in the flow. These complications of the picture manifest themselves up to the absence of iron in the expected horizons of flows.

Acknowledgements. We are grateful to A.A.Shchetnikov and A.M. Kozlovsky for the samples from basaltic rivers Zhombolok and Maly Yenisey and geological description.

References:

Balkhanov V.S., Bashkuev, Yu.B. Eruption of the lava of Flat Tolbachik (Kamchatka-2012) // Journal of Technical Physics. -2015. – V.85. -No. 8. - P.145-146. (In Russian).
Lebedev E.B., Khitarov N.I. Physical properties of igneous melts. M.: Nauka. -1979. - 200 p. (In Russian).
Persikov E.S. Viscosity of igneous melts. M .: Nauka. - 1984. - 160 p. (In Russian).
Pechersky D.M., Kuzina D.M., Markov G.P., Tselmovich V.A. Native iron on Earth and in space //Izvestya. Physics of the Earth. – 2017. - No. 5. - P. 44-62(In Russian).
Pechersky D.M., Kazansky A.Yu., Markov G.P., Tselmovich V.A., Shchetnikov A.A. The rare phenomenon of accumulation in the lake sediments of particles of metallic iron of terrestrial origin: the Zhombolok volcanic region, the East Sayan //Isvestiya Physics of the Earth. – 2018. - No. 1. - P. 113-127. (In Russian).
Pechersky D.M. Distribution of particles of native iron and Fe-Ni alloys on planets // Saarbrücken: Palmarium Academic Publishing. - 2015. - 56 p. (In Russian).
Fedotov S.A. The large fissure Tolbachik eruption. Kamchatka 1975-1976. M: Nauka. - 1984. - 638 p. (In Russian).
Yarmolyuk V.V., Nikiforov A.V., Ivanov V.G. The structure, composition, sources and mechanism of valley outpourings of lava flows of Zhombolok (Holocene, South Baikal volcanic region) // Volcanology and seismology. – 2003. - No. 5. – P.41-59. (In Russian).

Senin V.G. [1], Zinovieva N.G. [2], Pankrushina E.A.[3], Averin A.A.[4], Khisina N.R.[1] Identification of minerals in shock melted regions in meteorite ELGA. UDC: 523.681.5; 552.6

[1]Institute of Geochemistry and Analytical Chemistry of RAN, khisina@gmail.com,
[2]Moscow State University,
[3]Institute of Geology and Geochemistry of UrO RAN,
[4]Institute of Physical Chemistry and Electrochemistry of RAN

Abstract. Shock melted regions in meteorite Elga are investigated with EMPA and Raman spectroscopy. Secondary shock-produced minerals of extraterrestrial origin are identified as schreibersite $(Fe,Ni)_3P$, troilite FeS, millerite NiS, merrillite $NaMgCa_9(PO_4)_7$, siderite $FeCO_3$, hematite Fe_2O_3 and Ni-magnetite.

***Keywords**: IIE irons, meteorite Elga, shock effects in meteorites, melt pockets, extraterrestrial siderite, Raman spectroscopy*

Introduction. Melt pockets and melt veins represent localized regions of shock-produced melting in meteorites. Shock mechanisms of localized melted areas formation include (1) injection of externally generated melts into the target rock along cracks and fractures and (2) in situ melting of a target rock by collapse of void space (Bogard et al, 1986, 1989; Wiens and Pepin, 1988). Local regions of shock-induced melting often associate with pre-existing vugs in meteoritic rocks (Walton and Show, 2009; Beck et al., 2007; Kuchka et al., 2017). In turn, shock process in porous material involves melting at the grain boundaries and jetting of melt into pores (Kiefer, 1975).

Meteorite Elga relates to silicate-bearing iron meteorites (IIE clan) that consist of rounded silicate inclusions embedded into FeNi matrix. Shock-produced zones in Elga manifest themselves by stratified schreibersite-oxide(s) reaction rims around silicate inclusions (Fig. 1) and by products of the late shock-induced transformation of the rims that are represented by breccias and melt pockets (Fig. 2). Mineralogy of the shock-produced zones was investigated with EMPA, SEM, and Raman spectroscopy.

Methods. Raman spectra of siderite, merrillite and Fe,Ni-oxides in the rim and breccias were measured at the Institute of Physical Chemistry and Electrochemistry of Russian Academy of Sciences using Senterra (Bruker GmbH) with lazer power 5 mW, diameter of beam at the sample 3мкм, excited wave length 532 nm. Raman microprobe measurements of individual micrometer-sized siderite precipitates in the melt pocket used a Horiba Jobin Yvon LabRam-HR (high resolution) system equipped with Olympus BX-FM optical microscope, a grating with 1800 grooves per millimetre, and Si-based, Peltier thermo-electrically cooled charge-coupled device (CCD) detector. Spectra were excited using the He–Ne 632.8 nm emission line (2 mW measured behind the microscope objective). With the system operated in confocal mode and 100× objective (numerical aperture 0.9), the lateral resolution was better than 2 μm (acquisition time 150 seconds, accumulation number 10).

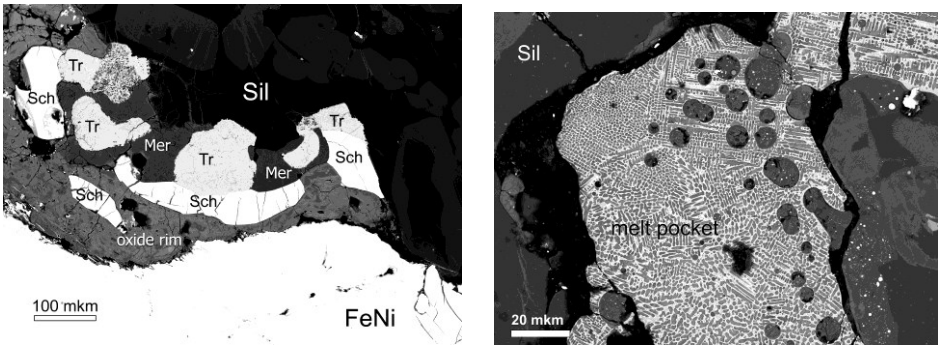

Fig. 1. Mineral assemblage at the contact between FeNi metal and silicate inclusion (Sil). Tr – troilite; Sch – schreibersite; oxide rim – Fe,Ni-oxides (light-grey) and siderite (dark-grey blots); Mer – merrillite.
Fig. 2. Melt pocket microtexture in the in the silicate inclusion.

Table 1. EMPA analyses data for oxygen-bearing phases in shock-melted zones.

Oxides, wt.%		Merrillite		Siderite	Fe,Ni-oxides av. (5)	
FeO	4.38	1.16	2.15	59.85	82.49*	
Fe_2O_3						91.67**
NiO	0.10	0.08	0.15	2.14	7.25	7.25
P_2O_5	43.46	45.65	43.37		0.34	0.34
CaO	44.14	47.53	48.69			
MgO	3.53	3.47	3.64			
SiO_2	1.96	0.15	0.69	0.23	0.17	0.17
Na_2O	2.20	2.61	2.29			
Al_2O_3	0.19					
CO_2***				38.25		
Σ	**99.95**	**100.65**	**101.01**	**100.47**	**90.25**	**99.43**
Sd					0.85	0.90

*calculated as FeO; **calculated as Fe_2O_3; ***CO_2 is calculated by stoichiometry.

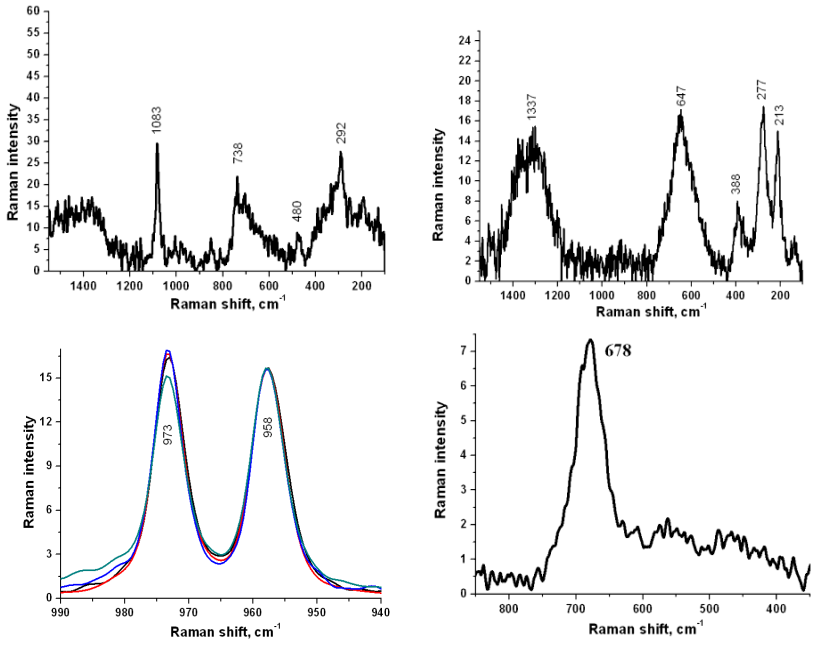

Fig. 3. Raman spectra of minerals occurred in the rim at the contact between silicate and FeNi metal (Fig. 1): (a) – siderite; (b) – hematite; (c) – merrillite: (d) –- magnetite

Chemical analyses of mineral phases in the sample were performed at the Vernadsky Institute of Geochemistry and Analytical Chemistry of Russian Academy of Sciences and in the Laboratory of High Spatial Resolution Analytical Techniques, Department of Petrology, Geological Faculty, Moscow State University. Phosphides, sulphides and FeNi metal were analyzed using SX 100 Cameca with acceleration voltage 15 kv and beam current 10 nA; standard employed were synthetic FeS and Ni, and meteoritic $(FeNi)_3P$. Quantitative chemical analyses of siderite, merrillite and Fe,Ni-oxides were carried out in wavelength-dispersion mode, using a Superprobe JEOL JXA-8230 operated under the following conditions: 20 kV acceleration voltage and $2*10^{-8}$ A beam current. A focused beam was used to analyze minerals and a defocused beam (diameter 10 μm) for the analysis of glass. Both samples and standards were analyzed at the same conditions. The standards employed were: apatite (Ca, P), $ScPO_4$ (P), dolomite (Mg, Ca), siderite (Fe, Mn). The counting time of the signal at the peak for each element was 30s, and that for the background from each side was 15s. A ZAF matrix correction was applied. The mean analytical results are reported in Table. 1.

Results.

Troilite and schreibersite.

Schreibersite forms rims at the boundaries between silicate inclusions and FeNi host. Also, the schreibersite occurs among the products of shock-produced transformation of the rims. Schreibersite clasts are observed in breccias and melt pockets; schreibersite

composes a matrics of phosphide-siderite melt pocket (Fig. 2).Chemical composition of schreibersite in the

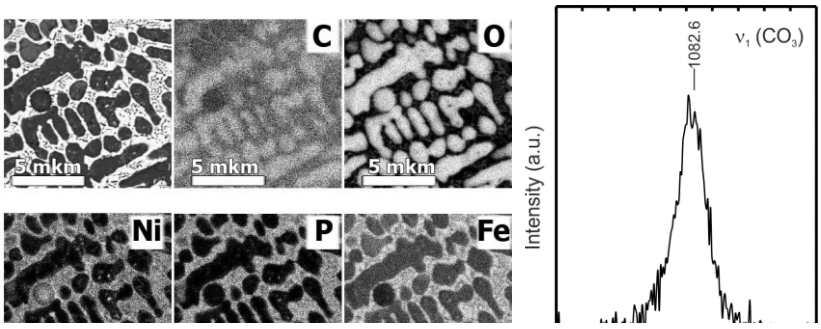

Fig. 4. Element mapping of Fe, Ni, P, C, O distribution and Raman spectra of siderite in melt pocket.

rim is $(Fe_{0.77}Ni_{0.23})_3P$. Troilite together with schreibersite occur in the rims around silicate inclusions (Khisina et al., 2017; Litasov and Podgornykh, 2017). Troilite inclusions that occur in the schreibersite-oxide rim (Fig. 1) exhibit often a ball-like shape and consist of aggregated FeS micrograins rimmed by NiS millerite. Mixed analyzes of cores and rims for individual sulphide grains show stoichiometric ratio as (Fe + Ni)/S = 1:1.

Siderite. Siderite occurs in the reaction rim at the boundary between silicate inclusion and FeNi host; in brecciated region at the contact of silicate inclusion and the crack extended through the FeNi metal; in melt pocket inside silicate inclusion. Siderite in stratified schreibersite-oxide rim has been preliminary estimated by Khisina et al. (2017). Here we report new data supported siderite occurrence in the schreibersite-oxide rim. Siderite is observed at BSE images of schreibersite-oxide rim as patchy contrasts in oxide(s) matrix (Fig 1). Siderite is identified from the chemical analyses data (Table 1) and Raman spectroscopy data (Fig. 3a). Siderite has a chemical composition as $Fe_{0.97}Ni_{0.03}CO_3$ (Table 1). Raman spectrum of siderite (Fig. 3a) exhibits the bands at 1083, 738, 480 and 213 cm^{-1} attributed to siderite.

The siderite in the melt pocket (Fig. 2) occurs in the form of rounded irregular precipitates of 1 - 2 μm in size uniformly distributed in the shreibersite matrix (Fig. 4). The microstructure of the melt pocket and the rounded shape of precipitates evidence a liquid-liquid phase separation in two immiscible melts. Thus we have deal with unmixing due to phosphide-carbonate liquid immiscibility in the shock-produced high-temperature melt. The Raman spectrum from the individual siderite grain in the melt pocket is shown in Fig. 4. The intense band at 1082.6 cm^{-1} corresponds to siderite (Buzgar and Apopei, 2009).

Merrillite. Merrillite occurs together with troilite, schreibersite, siderite, and Fe,Ni-oxide(s) in destroyed region of schreibersite-oxide rim. Raman spectra (Fig. 3c) demonstrate intensive bands at 958 and 973 cm^{-1} of merrillite (Litasov and Podgornykh, 2017). Representative chemical analyses of merrillite are given in Table 1. It should be mentioned that only some analyses (analysis 1) can be calculated for merrillite with a stoichiometry close to ideal crystal chemical formula of merrillite as $NaMgCa_9(PO_4)_7$. From the Table 1 we can observe that chemical compositions vary from point to point by a content of trace elements Si and Fe. Calculated atomic Ca/P ratio varies as 1.26 – 1.36 in Elga' sample deviating from stoichiometric Ca/P ratio equal to 1/29 in ideal merrillite. As it is known, isomorphous substitutions in merrillite allow the entry of Ca in the position of Na (with the simultaneous formation of vacancies); the entry of Fe into the position of Mg and the entry of Si into position P (Jolliff et al., 2006). The substitution of Ca for Fe in Ca position was suggested for merrillite found in other parts of the meteorite Elga (Litasov and Podgornykh, 2017). Taking into account possible isomorphic substitutions, analyzes of merrillite in the shock melted zone given in this report can't be calculated for pure merrillite. The variations of chemical composition observed from point to point in merrillite indicate rather the phase inhomogeneity caused by the capture of the silicate melt portions in the process of impact recrystallization of merrillite.

Fe,Ni-oxides. EMPA chemical analyzes data of Fe, Ni-oxides in the oxide sublayer of the rim and in the oxide clast of breccia when calculated for FeO are characterized by a low amount of oxides (Table 1). The same analyzes when calculated for Fe_2O_3 results in a good amount of oxides, but we can't be sure that all iron is trivalent. Raman spectroscopy was used to identify the oxide phases. In carrying out the Raman experiment, certain difficulties arose. The low quality of Raman spectra due to the probable microporosity of the object with the formation of microaggregates of grains made it necessary to use powerful laser regimes and long signal accumulation times. However, Fe-oxides are easily oxidized under the action of a laser in micro-Raman experiments: magnetite passes into hematite at> 20mW (Shebanova and Lazor, 2003). We carried out a series of measurements at different laser energies and found that in our samples the transition of magnetite to hematite occurs at> 5mW. Therefore, we used the modes 2.0 mW and 5 mW in Raman experiments to obtain Raman spectra of the oxide(s) in the schreibersite-oxide rim around silicate inclusion and in the fragments of breccia. The obtained spectra demonstrate the presence of hematite and Ni-magnetite in the objects of investigation (Fig. 3b,

Fig. 3d). The bands at 1337, 647, 388, 277, and 213 cm^{-1} (Fig. 3b) are attributed to hematite (Shebanova and Lazor, 2003). In addition to hematite, oxide phase of nearly magnetite composition is found from Raman spectra (Fig. 3d). Raman spectrum (Fig. 3d) exhibits the band at 678 cm^{-1}. Position of the main band of pure magnetite Fe_3O_4 in Raman spectra is 654 cm^{-1} (Shebanova and Lazor, 2003), the main band of Fe_2NiO_4 trevorite is at 700 cm^{-1} (Rana and Johri, 2013). As compared to magnetite and trevorite spectra, the band at 678 cm^{-1} in the Raman spectrum of Elga (Fig. 3d) corresponds to Ni-magnetite of approximately equimolar Fe_3O_4-Fe_2NiO_4 composition.

Conclusion. The secondary minerals of extraterrestrial origin, formed as a result of the impact, were identified by EMPA and Raman spectroscopy in the shock-produced zones in Elga meteorite: $(Fe,Ni)_3P$ schreibersite, FeS troilite, NiS millerite, $NaMgCa_9(PO_4)_7$ merrillite, $FeCO_3$ siderite, Fe_2O_3 hematite, Ni magnetite. We conclude that Fe, Ni, P, S, C and oxygen have been involved in shock transformation process, wherein each of these elements occurs in different valence states: Fe^0, Fe^{2+} and Fe^{3+}; Ni^0 and Ni^{2+}; P^0 and P^{5+}; C^0 and C^{4+}. Shock-induced redox reactions proceed obviously at the contacts of silicate inclusion and FeNi host. The schreibersite forming rims at the boundaries between silicate inclusions and FeNi host evidences that the system might approximate a phosphide-phosphate buffer, i.e., part-way through the reduction reaction at high temperatures. Bulk equilibrium was not reached in the system, however, because of a very short duration of impact. The results indicate heterogeneity of pressure, temperature and fO_2 distribution in shocked material in a case of shock wave propagation through heterogeneous rock. A high-temperature shock-induced melting in meteorite Elga might be caused by a presence of vugs (open spaces) in the target rock. The temperature increase at open fissures can be especially high because impedance contrasts of empty space and rock are extreme (Heider and Kenkmann, 2003). Our data demonstrate the first finding of siderite in shock melted zones in IIE iron meteorites. The results prove an extraterrestrial shock-produced origin of siderite in Elga.

Acknowledgments. Authors are thankful to A.A. Shiryaev and A. Burmistrov for their help in conducting research and interpretation of analytical data, and A. Abdrakhimov for technical support. This research was supported by the Program of MSU Development and the Program 7 of ONZ RAN.

References:

Beck P., Ferroir T., Gillet P. (2007) *Geophys. Res. Lett*., 34, L01203.
Buzgar N. and Apopei A.I. (2009) *Ananele Stiintifice Ale Univ., Al. I.Cuza Lasi Geologie*, 55, 97 – 112.
Jolliff B.L. et al. (2006) *Amer. Mineral*., 91, 1583-1595.
Khisina N.R., Teplyakova S.N., Senin V.G., Wirth R. et al. (2017) *Geochemistry International*, 55, 4, 317-329.
Kiefer S. W., Phakey P. P., and Christie J. M. (1975) *Contrib. Mineral. Petrol*., 59, 41-93.
Litasov K. and Podgornykh. (2017) *J. Raman Spectrosc*.
Panta P.C. and Bergmann C.P. (2015) *J. Material Sci. Eng.*, 5:2017.
Rana G. and Johri U.C. (2013) *J. of alloys and compounds* **577**, 376-381.
Shebanova O.N. and P. Lazor (2003) *J. Solid State Chemistry*, 174, 424 – 430.
Walton E. L. and Show C. S. J. (2009) *Meteoritics and Planetary Sci*., 44, 55-76.

Shornikov S. I., Yakovlev O. I. Study of double inversion of MgO/SiO_2 relative fugacity at the CAIs melt's evaporation

Vernadsky Institute of Geochemistry & Analytical Chemistry RAS, Moscow (sergey.shornikov@gmail.com)

Abstract. The composition variation of Ca–Al–inclusions (CAIs) in chondrite at evaporation was studied at temperature of 2173 K in the framework of the thermodynamic model. The semiempirical model was based on the ideal associated solution theory and experimental data on the CaO–MgO–FeO–Al_2O_3–TiO_2–SiO_2 melts obtained by Knudsen effusion mass-spectrometric method in the temperature range of 1600–2500 K. It was observed the typical inversion of MgO / SiO_2 relative volatility due to the predominant evaporation of MgO from the melt at the most of the CAIs compositions. However, for the composition (mol. %: CaO – 14.43, MgO – 25.60, Al_2O_3 – 23.88, SiO_2 – 36.14) there was a double inversion of the MgO / SiO_2 ratio: the first (about 35 mol. % Al_2O_3), which leads to the predominance of MgO contents in the melt, and the second (about 60 mol. % Al_2O_3) which leads to the predominance of SiO_2 contents in the melt. It is shown that small deviations of CaO contents from the considered composition could lead to either the MgO predominance in the melt (compared to SiO_2) due to the SiO_2 preferential evaporation from the melt or the SiO_2 predominance in the melt (compared to MgO) due to the MgO preferential evaporation from the melt.

***Keywords**: CAIs, evaporation, thermodynamics.*

Within the developed thermodynamic model of evaporation of multicomponent oxide melts (Shornikov, 2009) we investigated the composition changes of the Ca-Al-Inclusion melts (CAIs) at 2173 K. The semiempirical model is based on the theory of ideal associated solutions and calibrated on experimental data on the oxide activities in the CaO–MgO–FeO–Al_2O_3–TiO_2–SiO_2 melts. These activities were defined by Knudsen effusion mass-spectrometric method within a temperature range of 1600–2500 K. The accuracy of these approach was confirmed earlier by coincidence of calculations and experimental data on two compositions (Shornikov, 2016). The first of them was a lunar alumina basalt (mol. %: CaO – 19.44, MgO – 7.26, FeO – 3.98, Al_2O_3 – 18.72, TiO_2 – 0.25, SiO_2 – 50.35). A lunar basalt evaporation was studied by the mass-spectrometric method using Knudsen effusion tungsten cells in the temperature range of 1577–2502 K (Markova et al., 1986). The second composition was a synthetic oxide material with an

elemental composition corresponding to the solar (mol. %: CaO – 2.08, MgO – 35.15, FeO – 29.18, Al_2O_3 – 1.38, TiO_2 – 0.08, SiO_2 – 32.13). Their evaporation was studied using graphite vacuum furnaces in the temperature range of 1673–2273 K (Wang et al., 2001). As can be seen from Fig. 1 the model satisfactorily describes the evaporation of CAIs other samples: CAI B (Mendybaev et al., 2018), CAI4 (Kamibayashi et al., 2018), 5aN-3 (Ivanova et al., 2018), the composition of which is shown in Table 1.

Table 1. The CAIs initial composition (mol. %).

Sample	CaO	MgO	Al_2O_3	SiO_2	MgO /SiO_2
5aN-L	11.17	25.00	23.83	40.00	0.63
5aN-3	14.43	25.60	23.83	36.14	0.71
5aN-H	17.03	27.98	23.23	31.76	0.88
CAI4	24.10	24.32	15.52	36.06	0.67
CAI B	26.76	17.05	11.41	44.78	0.38

As shown in Fig. 1, despite the differences in the initial compositions of CAIs, there is a certain similarity in the increase of the contents of the most refractory components in the residual melts during evaporation – CaO and Al_2O_3. This change is accompanied by an inversion of the MgO / SiO_2 relative volatility typical for most compositions, consisting in a predominance of MgO evaporation (compared to SiO_2) from the melt (Fig. 2). However, the evaporation of the *5aN-3* composition occurs on the contrary – these ratio increases and then decreases (Fig. 2).

To explain this phenomenon, we studied the evaporation of two compositions with the slightly low and slightly high of the CaO content in the melt (*5aN-L* and *5aN-H*). As can be seen from the comparison of calculated evaporation trends (Fig. 3*a*), small deviations in the CaO content from the composition *5aN-3* led in the case of the composition *5aN-L* to the MgO predominance in the melt (compared to SiO_2) and to the SiO_2 predominant evaporation of from the melt, and in the case of *5aN-H* – to the SiO_2 predominance in the melt (compared to MgO) and, respectively, the MgO preferential evaporation from the melt. Moreover, the MgO amount in the initial melts was more in the composition of *5aN-H* compared to *5aN-L* (Table 1).

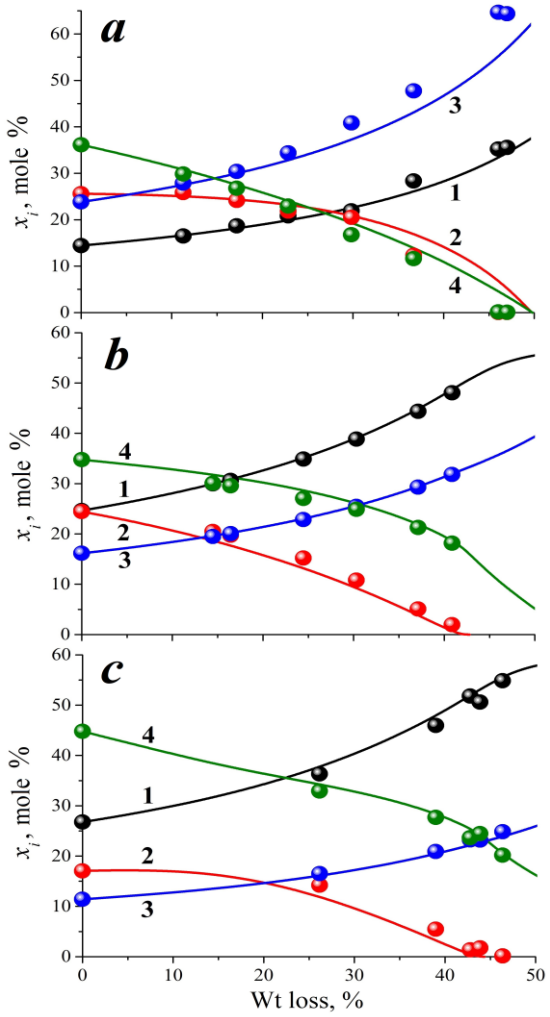

Fig. 1. The experimental (points) and calculated (lines) changes in residual melts of *5aN-3* (*a*), *CAI4* (*b*) and *CAI B* (*c*) at evaporation at 2173 K: 1 – CaO, 2 – MgO, 3 – Al_2O_3, 4 – SiO_2.

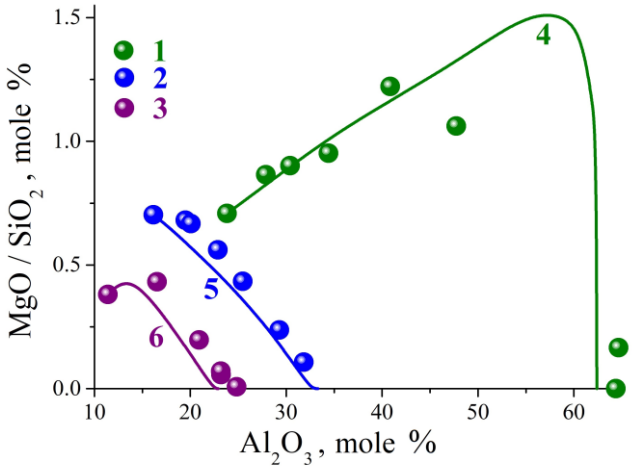

Fig. 2. The experimental (1–3) and calculated (4–6) MgO / SiO_2 molar ratio changes in residual melts of *5aN-3* (1, 4), *CAI4* (2, 5) and *CAI B* (3, 6) at evaporation at 2173 K.

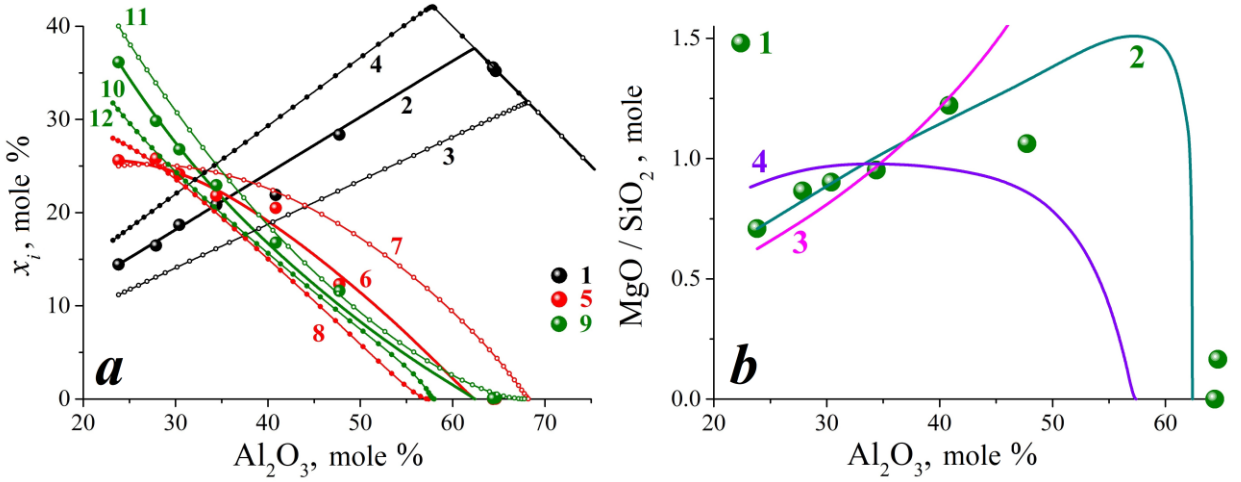

Fig. 3*a*. The experimental (1, 5, 9) and calculated (2–4, 6–8, 10–12) changes in residual melts of *5aN-3* (1, 2, 5, 6, 9, 10), *5aN-L* (3, 7, 11), *5aN-H* (4, 8, 12) during evaporation at 2173 K. Designations: 1–4 – CaO, 5–8 – MgO, 9–12 – SiO_2.

Fig. 3*b*. The experimental (1) and calculated (2–4) MgO / SiO_2 molar ratio changes in residual melts of *5aN-3* (1, 2), *5aN-L* (3) and *5aN-H* (4) at evaporation at 2173 K.

We can see the double inversion of the MgO / SiO_2 ratio in the case of the *5aN-3* composition. The first inversion (about 35 mol. % Al_2O_3) is lead to the MgO predominance in the melt. The second inversion (about 60 mol. % Al_2O_3) is lead to the SiO_2 predominance in the melt (Fig. 3*b*).

Thus, there is an inversion of the MgO and SiO_2 volatility at the high–temperature evaporation of CAIs. It consists in the fact that silicon oxide, being more volatile than magnesium oxide, becomes less volatile at the evaporation conditions of melts rich in refractory oxides (CaO and Al_2O_3). The observed volatility inversion is well explained within the framework of Korzhinsky's theory on acid-base interaction of components in silicate melts (Korzhinsky, 1959) in the case of evaporation of CAIs compositions.

According to the theory, the CaO content increase in the melt leads to an increase in its basicity, which, in turn, increases the activity and, accordingly, the volatility of MgO (and reduces the activity and, accordingly, the volatility of SiO_2). The MgO / SiO_2 ratio decreases with increasing the CaO content, which is a direct consequence of the acid-base factor in the real compositions of CAIs of chondrites.

The present study was supported by RAS Presidium's Program #7 (Experimental and theoretical studies of Solar system objects and star planetary systems. Transients in astrophysics).

References:

Ivanova M. A., Mendybaev R. A., Shornikov S. I., Ryazantsev K. M., MacPherson G. J. (2018) Evaporation of spinel-rich CAIs melts: a possible link to CH-CB CAIs. *LPSC–XLIX*, Abs. #1965.

Kamibayashi M., Mendybaev R. A., Richter F. M., Tachibana S. (2018) Evaporation kinetics of CAI-like melts in low-pressure hydrogen gas and in vacuum: similarities and differences. *LPSC–XLIX*, Abs. #2432.

Korzhinskii D. S. (1959) Acid–base interaction of components in silicate melts and the direction of cotectic lines. *DAN SSSR*, vol. 128, no. 2, pp. 383–386.

Markova O. M., Yakovlev O. I., Semenov G. A., Belov A. N. (1986) Some general experimental results on the evaporation of natural melts in a Knudsen cell. *Geochem. Int.*, vol. 24, no. 11, pp. 1559–1569.

Mendybaev R. A., Teng F.-Z., Kamibayashi M., Georg R. B., Davis A. M., Tachibana S., Richter F. M. (2018) Magnesium isotopic fractionation during evaporation of CAI-like melts in low-pressure hydrogen gas and in vacuum: similarities and differences. *LPSC–XLIX*, Abs. #2580.

Shornikov S. I. (2009) Thermodynamic study of the evaporation kinetics of the CaO–MgO–Al_2O_3–FeO–SiO_2 melts. *Vestn. Otd. nauk Zemle RAN*, vol. 27, no. 1, pp. 1–4.

Shornikov S. I. (2016) Thermodynamics of evaporation of multicomponent oxide systems. *Ceramics and composite materials*, Syktyvkar: Komi scientific center of RAS Ural branch, pp. 446–449 (in Russian).

Wang J., Davis A. M., Clayton R. N., Mayeda T. K., Hashimoto A. (2001) Chemical and isotopic fractionation during the evaporation of the FeO–MgO–SiO_2–CaO–Al_2O_3–TiO_2 rare earth element melt system. *Geochim. Cosmochim. Acta*, vol. 65, no. 3, pp. 479–494.

Tselmovich V.A.[1], Lyukhin A.M.[2], Sheremet V.A.[3] Evidence of an impact process on minerals from Carolina Bays craters (eastern coast of the USA) UDC 551.14 +551.2+554.015.4

[1]Geophysical Observatory "Borok", The Schmidt Institute of Physics of the Earth, Russian Acad. Sci., Borok, Yaroslavl' Region, RF (tselm@mail.ru)
[2] Institute of Remote Forecasting of Ores, LLC, Moscow, RF (alex.lyukhin@gmail.com)
[3]Graduate School of Oceanography, University of Rhode Island, RI, USA (vsheremet@uri.edu).

Abstract. On the Atlantic coast of the USA, spanning more than 1000 km from Florida to NewJersey, there are over 500,000 oval craters, called "Carolina Bays". Samples

extracted with a Nd magnet from loose sediments of 3 craters, located 10 km north of Myrtle Beach, South Carolina, were studied at the Geophysical Observatory "Borok" IPE RAS with SEM "Tescan Vega II". Micro- and nanoparticles and films of pure Ni were found on the surface of the rounded ilmenite, magnetine and quartz grains, as well as microparticles of native metals and alloys. For the first time in the material of these craters, we found the traces of the process of thermal interaction of terrestrial and cosmic materials that occurred in situ. It is assumed that the craters were formed by numerous fragments of an aerodynamically destroyed cosmic body (a comet or an asteroid), approaching the Earth on a very oblique trajectory.

Keywords: *Carolina Bays; oval craters; impact process; nanoparticles and films of pure Ni; native metals; thermal interaction; oblique impact.*

Introduction. On the Atlantic coast of the USA, spanning more than 1000 km from Florida to NewJersey, there are over 500,000 oval craters, up to 15 km in size, called "Carolina Bays" (Fig.1) (named after the bay laurel trees growing inside them), the origin of which causes a controversy. The main features of these natural formations are the following: they have an elliptical shape; all of them are stretched in the same direction to the north-west; their dimensions along the major axis vary from 50 meters to 15 kilometers; they are small depressions below the surrounding topographic surface with a maximum depth of about 15 meters; they often overlap each other without disturbing morphology; the stratigraphy of the rocks under them is not broken; in recent years, exotic black glass have been found in some of them in the form of sponges, fullerenes, hollow carbon spheres containing nanodiamonds (Firestone at al, 2010).

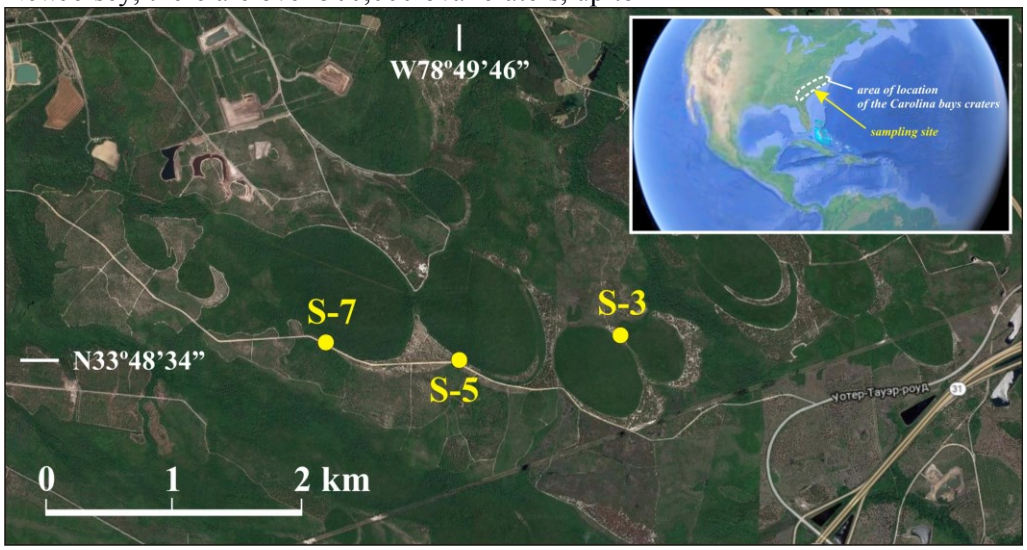

Fig. 1. Carolina Bays Craters on the Google maps and sampling sites (yellow dots).

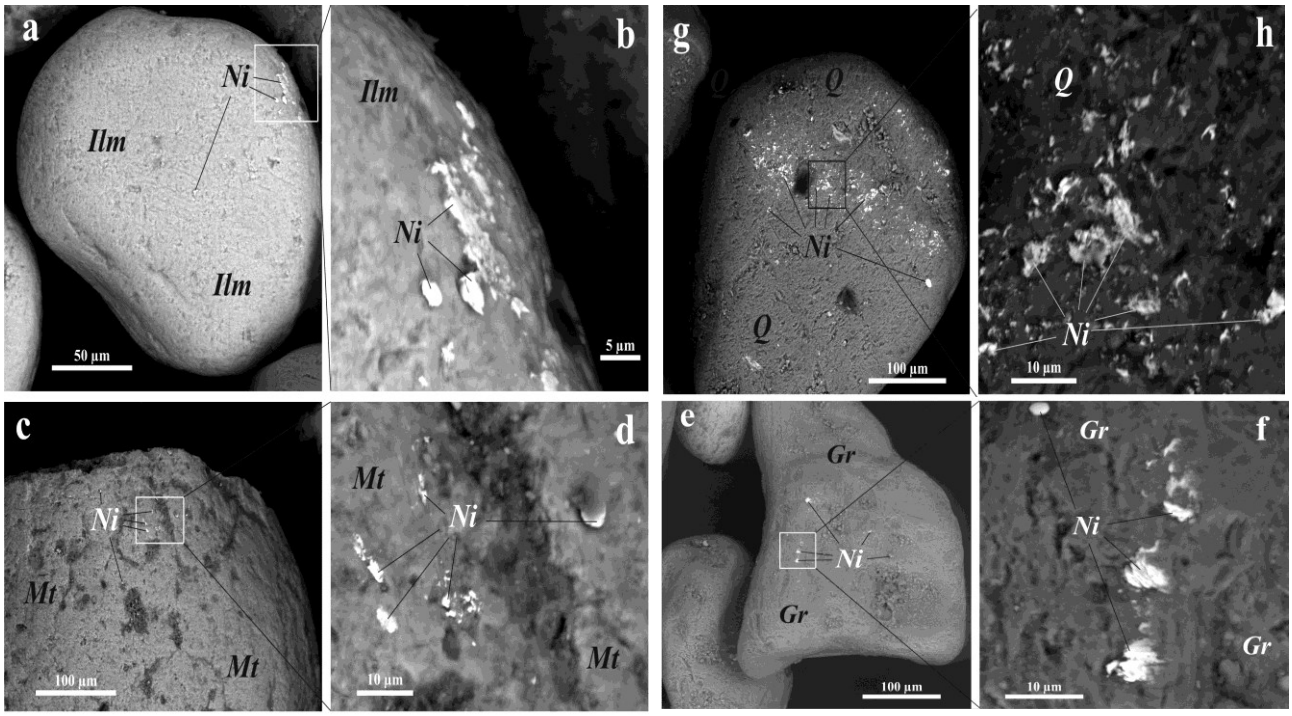

Fig. 2. BSE images, nanoparticles and films of pure Ni (white) on the surface of the rounded ilmenite (a,b), magnetite (c,d) and garnet (e,f) grains, quartz (g,h) grains.

Methods & Results. Samples extracted with a Nd magnet from loose sediments of 3 craters (Fig. 1), located 10 km north of Myrtle Beach, South Carolina, were studied at the Geophysical Observatory "Borok" IPE RAS with a Scanning Electron Microscope (SEM) "Tescan Vega II". Each sample was extracted from approximately 1kg of sand.

Micro- and nanoparticles and films of pure Ni were found on the surface of the rounded ilmenite, magnetite, garnet and quartz grains (Fig. 2). They vary widely in size from individual nanometer particles to areas that occupy a significant part of the surface of the minerals. In this case, these formations are observed only on one side of the grains of terrestrial minerals, which indicates the preferred direction of the shock process. Very frequently, on the rolled mineral grains observed are plaques consisting of a carbon substance of an unknown composition. In addition, the samples contained microparticles of native metals and alloys: Fe, Zn, CuZn, FeCrNi, FeNd.

Conclusions. For the first time in the material of these craters, we found not only the minerals of impact origin but also the traces of the process of thermal interaction of terrestrial and cosmic materials that occurred in situ.

It is assumed that the craters were formed by numerous fragments of an aerodynamically destroyed cosmic body (a comet or an asteroid), approaching the Earth on a very oblique trajectory.

Acknowledgments: The work was carried out on the budget topic "Spatial-temporal structure of the ancient geomagnetic field and petrophysics of magnetic minerals as indicators of geological and geophysical processes", State Registration No. AAAA-A17-117040610183-6. Microprobe studies were carried out with the support of the Russian Foundation for Basic Research, project No. 16-05-00703a.

Reference:

Firestone R.B., West A., Revay Z., Hagstrum J.T., Belgya T., Que Hee S.S. and Smith A.R. Analysis of the Younger Dryas Impact Layer // Journal of Siberian Federal University. Engineering & Technologies, 1 (2010 3) 30-62.

Ustinova G.K. The solar proton effects in the chondrites of low level ablation. UDC 523.165

V.I. Vernadsky Institute of Geochemistry and Analytical Chemistry RAS, Moscow (ustinova@dubna.net.ru)

Abstract. The solar cosmic ray (SCR) contributions to production of the cosmogenic radionuclides in the near-surface layers of the chondrites of low ablation are estimated. It is shown that the solar proton effects develop only at 6-10 cm from the surface of the chondrites. They depend on the level of the solar activity, as well as on the average heliocentric distances of the chondrite orbits and on the depth distributions of the samples inside the chondrites.

Keywords: *chondrites, cosmogenic radionuclides, cosmic rays, solar activity, solar protons.*

Introduction. During orbital revolution, chondrites are irradiated with the galactic cosmic rays (GCR) of $E > 100$ MeV, entering the Solar System isotropically from the surrounding cosmic space, as well as with SCRs (mainly, protons of $E \sim$ 20-500 MeV), which, in accordance with the 11-year variations of the solar activity, are emitted periodically by the sun to meet GCRs. Due to the sun rotation, the initially radial motion of SCRs is gradually twisted as an Archimedean spiral, so that at about ~ 5 AU their motion becomes the practically azimuthal one (Parker,1969). The similar changes are undergone by all the solar irradiations – in particular, by the solar wind, the frozen magnetic fields of which, when being twisted, create hardly insuperable barriers to GCR penetration into the heliosphere, i.e. sweep them out practically. Thus, the solar modulation of GCRs arises, i.e. at the higher solar activity (e.g. SCR intensity) the GCR intensity is lower near the Earth.

Since 1957, monthly measurements of the GCR intensity ($E > 100$ MeV) in the stratosphere (Stozhkov et al., 2009) allow us to analyze cosmogenic radionuclides of different half-lives $T_{½}$ in the meteorites, falling to the Earth, and to derive the unique information on the character of the GCR modulation at different heliocentric distances in accordance with the sizes of the meteoritic orbits (Lavrukhina, Ustinova, 1990; Alexeev, Ustinova, 2006). However, such an analysis provides the necessity to estimate and exclude contributions of the SCRs in production of the radionuclides, which might be essential in the meteorites that fell during the years of the high solar activity.

Dependence on the solar activity: Unfortunately, any continuous data on the SCR intensity are absent. There is a value of 330 proton $cm^{-2}s^{-1}$ (>20 MeV) measured for the maximum solar activity in 1956, 1959 and 1960 (Ebeoglu, Wainio, 1966), whereas the average SCR intensity (>20 MeV) for the solar cycle, as well as for the last million years, is 31 proton $cm^{-2}s^{-1}$ (2.46 proton $cm^{-2}s^{-1}sr^{-1}$), which follows from the ^{22}Na and ^{26}Al radioactivity data of the lunar sample 10017 delivered by Apollo 11 (Lavrukhina, Ustinova, 1971). The anti-correlated interdependency of decline and rise of the GCR intensity near the Earth with the periodical increase and decrease of the SCR intensity allows us to approximate such a process with the Gauss error curve – namely, $y = 330e^{-1.051(x-1.5)^2}$, which links the maximum (330

proton $cm^{-2}s^{-1}$) and the average (31 proton $cm^{-2}s^{-1}$)intensities of the solar protons with, accordingly, the minimal (1.5nucleon $cm^{-2}s^{-1}$ (0.12 nucleon $cm^{-2}s^{-1}sr^{-1}$) and the average (3 nucleon $cm^{-2}s^{-1}$ (0.24 nucleon $cm^{-2}s^{-1}sr^{-1}$) GCR intensities near the Earth (Fig. 1). Using the stratospheric data of the GCR intensity for a time period of the solar activity, one may estimate the corresponding average intensity of the solar protons for that time. Fig. 1 demonstrates clearly that the solar proton intensity can exceed the GCR intensity by two orders of magnitude, which would firstly affect the production of some short-lived radionuclides (e.g. , ^{48}V, ^{51}Cr,…) in the meteorites falling in the years of high solar activity.

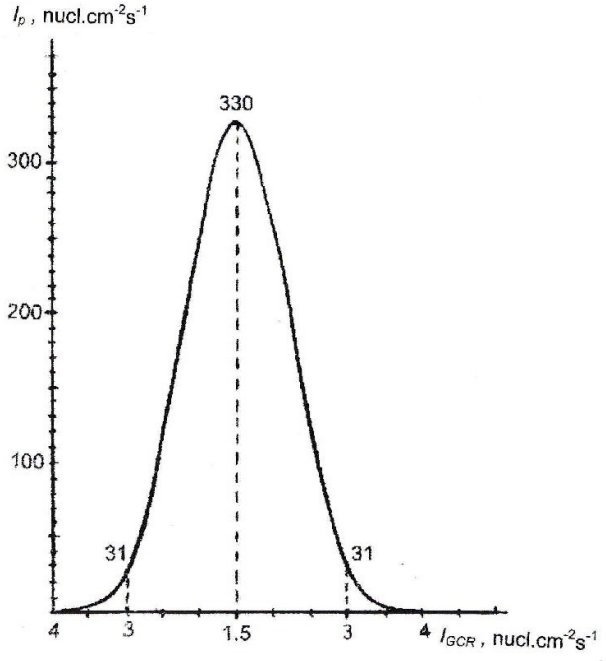

Fig.1. A function $y = 330e^{-1.051(x-1.5)^2}$ of the solar cycle approximation. Real interrelated decreases of the GCR intensity I_{GCR} (from 4 down to 1.5 nucl.$cm^{-2}s^{-1}$) are marked on the x axis at the corresponding increases of the solar proton intensity Ip (from 0 up to 330 nucl.$cm^{-2}s^{-1}$), as well as further: the subsequent increases of the GCR intensity at the corresponding decreases of the solar proton intensity.

Dependence on heliocentric distances: In the case of production of the radionuclides of $T_{½} \geq 1$ y, it should be taken into account that the force of source (e.g., the Sun) is diminished proportionally to the distance squared. Indeed, up to 80% of the measured contents of radionuclides (at the moment of meteorite fall) are accumulated during ~ 1.5 $T_{½}$ of the radionuclides, i.e. at the average heliocentric distances of meteorites corresponding to ~0.75 $T_{½}$ (Lavrukhina, Ustinova, 1990; Alexeev et al., 2015). The known orbits of the Stubenberg (LL6) and Jesenice (L6) chondrites (Meier, 2016) are demonstrated in *r(t)* coordinates in Fig.2. The Jesenice chondrite fell on April 4, 2009 in the prolonged minimum of the solar activity of the 23rd cycle, and the Stubenberg chondrite fell on March 3 2016 during the phase of decreasing solar activity of the 24th cycle, so that the solar proton fluxes near the Earth were far from the maximum ones. Hence, their contribution into the production of the short-lived radionuclides (and even ^{22}Na) at 1 AU in the Stubenberg chondrite was small (see Table 2 below). Besides, as it follows from Fig.2, the average heliocentric distances r_c of the ^{22}Na accumulation in the Jesenice chondrite, and of the ^{54}Mn accumulation in the Stubenberg and Jesenice chondrites equal 1.65 AU, 1.98 AU, and 2.14 AU, respectively. It means that the solar proton fluxes, which initiated the production of the radionuclides, were already reduced by (r_c^2) times in comparison with their intensities at 1 AU.

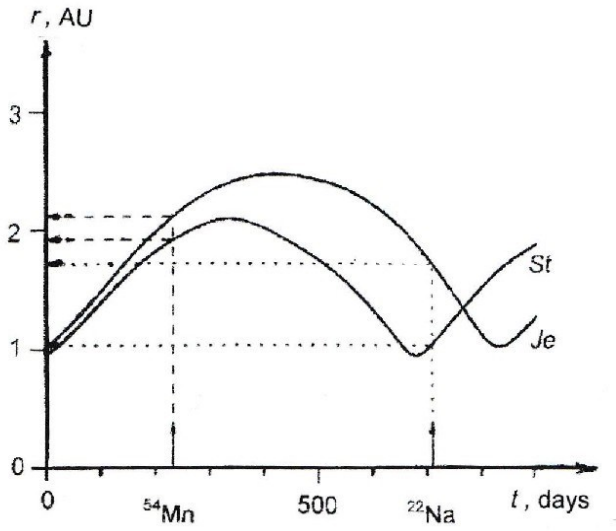

Fig.2. Dependence of the heliocentric distance r on time t of orbits of the Stubenberg (St) and Jesenice (Je) chondrites before their fall to the Earth in t=0. Some moments $0.75T_{½}$ of the average effective accumulation of the radionuclides ^{54}Mn and ^{22}Na are marked on the x axis, and the corresponding average heliocentric distances r_c are shown by arrows on the y axis.

As it was already mentioned above, the long-lived radionuclides being similar to ^{26}Al are produced in lunar samples at the average intensity of the solar protons of 31 proton $cm^{-2}s^{-1}$, which is lower by an order of magnitude than the one registered near the Earth during the periods of the maximum solar activity. Meanwhile, in meteorites the ^{26}Al is accumulated at the average heliocentric distances r_0 of their orbits, which correspond to ¼P of the orbital period P of the meteorites, and, therefore, it is suitably accumulated with the solar proton fluxes which were (r_0^2) times lower. The larger is the orbit of meteorite, the smaller contribution of the solar protons to the production of long-lived radionuclides (in particular, ^{26}Al) should be expected.

Dependence on the radionuclide production cross sections: Considering different radionuclides, it should be taken into account that their contents depend on the cross sections of their production by nuclear-active particles of different energies on the target elements of the meteorite composition. Some difference of the production cross sections of radionuclides in L-chondrites with primary SCRs and GCRs, which are averaged in accordance with their energy spectra, as well as with the chondrite compositions (Lavrukhina, Ustinova, 1990), are presented in Table 1.

Table 1. Weighted mean values of cross sections (in mbarn) of the cosmogenic radionuclides with the solar protons (>0.02GeV) and with the primary GCRs (>0.2 GeV) in L- chondrites.

	^{48}V	^{51}Cr	^{46}Sc	^{54}Mn	^{22}Na	^{55}Fe	^{26}Al
P_{solar}	0.27	5.36	0.11	5.06	7.22	65.62	8.24
P_{GCR}	1.55	6.96	1.26	3.99	4.99	10.07	3.99

Dependence on screening depth in cosmic bodies: One of the main factors defining effects of the solar protons is a sharp drop of their intensity in the nearest surface layers of cosmic bodies.

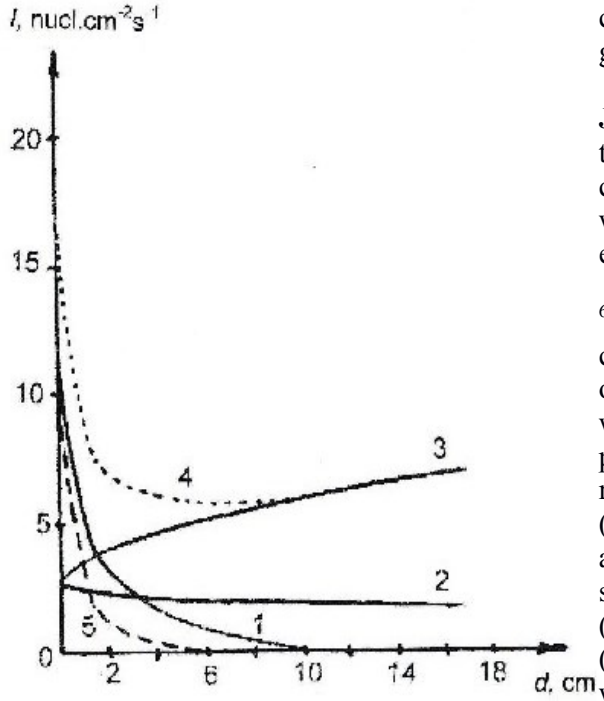

Fig.3. Depth distributions of the primary and secondary nuclear-active particles of the cosmic radiation in the surface layer of the lunar regolith (1 – solar protons; 2 – primary component of the GCRs; 3 – total flux of the primary and secondary GCRs; 4 – total flux of the GCRs and solar protons; 5 – deep drop of the solar protons in L/LL-chondrites.

In Fig. 3, depth distributions of nuclear-active particles in the surface layer of the "Luna-16" regolith, if it is irradiated by the GCRs of the energy spectrum of 1962 and the solar protons of the average intensity of 31 proton $cm^{-2}s^{-1}$, are demonstrated.

Curves 1 and 2 clearly demonstrate how strongly the deep profile of the low-energy solar protons differs from that of the GCR primary component. The solar protons are practically depleted at the first ~10 cm from the surface, whereas the primary GCR component and initiated cascade of the secondary particles prevail at the depths > 2 cm from the surface (curve 3).

The similar regularity for all the nuclear-active particles is demonstrated by curve 4. Indeed, the solar proton effects are dominant at the first 2 cm from the lunar surface, meanwhile, they are practically absent at the depths > 10 cm from the surface, i.e. which is the zone of operation of just the primary and secondary GCRs only.

The curve 5 that is also presented in Fig.3 demonstrates the solar proton profile in the matter of the L/LL-chondrites. It is sharper than that in the lunar regolith, being already depleted at the 6 cm from the surface. It is mainly conditioned by the stronger ionization losses of the energy of particles in the more dense matter of the L/LL-chondrites (~3.5 g cm^{-3}), as compared with that of the lunar regolith (1.7 g cm^{-3}).

The solar proton effects in the Stubenberg and Jesenice chondrites: There is a certain probability that the Stubenberg and Jesenice chondrites, considered here further, have been undergone only weak ablation, so that they might conserve some effects of the solar protons.

Indeed, in Fig. 4 the depth distributions of ^{60}Co/^{26}Al ratios in the Stubenberg and Jesenice chondrites are presented, which differ from each other mainly in the ^{59}Co content (0.056 and 0.088 weight %, respectively), from which ^{60}Co is produced. Ranges of the measured values of these ratios in the investigated samples of the chondrites (Bischoff et al., 2011; 2017) point out to their sizes *R* and to the screening depths *d* of the samples from the surface: namely, *R* ~ 10-20 cm, *d* ~ 2-8 cm (Stubenberg) and *R* ~ 20-30 cm, *d* ~ 2-6 cm (Jesenice). The solar proton effects at such depths would be conserved, because, in accordance with Fig.3, their range of operation is just the nearest to the surface layer of 6 cm. Perhaps, one may expect that, in the bodies of *R* > 10 cm, the solar proton distributions near the surface (d ≤ 6 cm) are practically similar to those in large cosmic bodies, irradiated in 2π-geometry.

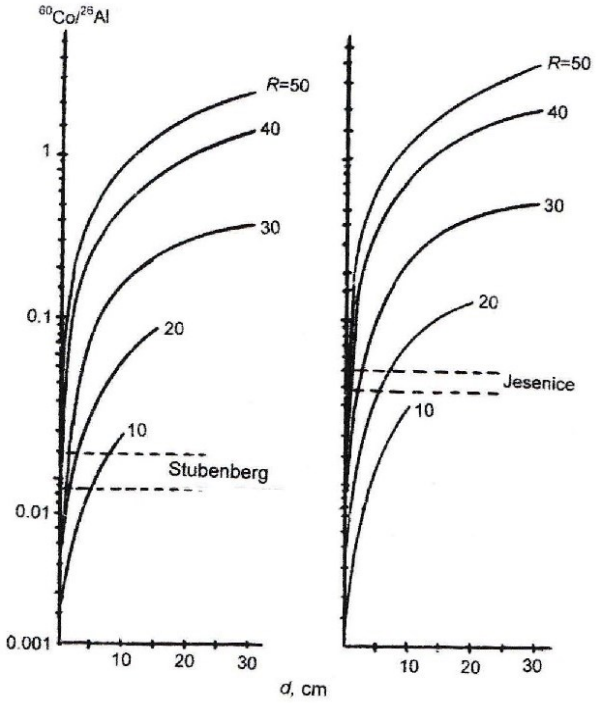

Fig.4. $^{60}Co/^{26}Al$ depth profiles in the Stubenberg and Jesenice chondrites at their different pre-atmospheric radii R (d – depth from the surface). The measured ranges of the ratio in the samples of the chondrites (Bischoff et al.,201; 2017) are marked by dashed lines

Taking into account all the factors (described above), which affect the contents of the different radionuclides produced by the solar protons in the near-surface layers of the chondrites of different orbits, which fell onto the Earth at the different levels of the solar activity, one may determine the contributions of the solar protons into the measured contents of cosmogenic radionuclides of various $T_{½}$ in the Stubenberg and Jesenice chondrites.

The results are presented in Table 2 in comparison with the obtained earlier data for the Bruderheim (L6) chondrite (Lavrukhina, Ustinova 1980; 1990). That L6-chondrite has fallen just after maximum of the 19 solar cycle at the intensity of the solar protons (E > 20 MeV) of 330 proton $cm^{-2}s^{-1}$. The aphelion of its most optimal orbit is q' = 4.06 AU; its average heliocentric distance is r ~ 3.29 AU; pre-atmospheric radius of the chondrite is R ~ 30-50 cm; screening depth of the samples is d ~ 2-10 cm.

Despite the fact that numerous factors, pointed out above, affected the contents of the radionuclides, produced by the solar protons in the chondrites having fallen to the Earth in various years of the solar activity, some definite regularities would be recorded, e.g., the high content of ^{55}Fe and the low one of ^{46}Sc, which is conditioned by the strong difference of their production cross sections with protons of low energy (see Table 1). Further, the short-lived radionuclides, being similar to ^{48}V, ^{51}Cr, and ^{46}Sc, are practically produced just prior to the chondrite fall at ~ 1 AU, so that their contents depend on the level of the solar activity (namely, intensity of the solar protons) for the date of fall. In particular, at the Jesenice chondrite fall during the prolonged minimum of the 23rd solar cycle the GCR intensity near the Earth was ~ 5 proton $cm^{-2}s^{-1}$, which, according to the data of Fig. 1, testifies to the practical absence of the solar protons near the Earth, and, respectively, to their zero contribution to production of the short-lived radionuclides in the chondrite (Table 2). Rare singularities are ^{22}Na and ^{55}Fe in the Stubenberg chondrite, in which their average heliocentric distance is also r ~ 1 AU (see Fig. 2). Therefore, despite the intensity of the solar protons near the Earth being by an order of magnitude smaller in comparison with their intensity at the Bruderheim chondrite, the solar proton contributions into the ^{22}Na and ^{55}Fe production in the Stubenberg chondrite are much higher, because in the Bruderheim chondrite they are produced at the average heliocentric distance of r ~ 3.29 AU, i.e., at the solar proton intensity that is smaller proportionally to that distance squared. The quite different situation is in the case of ^{26}Al and other long-lived radionuclides, which are produced at the average intensity of the solar protons for the last million years of about 31 proton $cm^{-2}s^{-1}$, and which, thus, do not depend anyway on the level of the solar activity over meteorite falls. In particular, the solar proton contributions in the ^{26}Al production in the chondrites, considered in Table 2, are defined only by relations of the average heliocentric distances of their orbits. In the case of the radionuclides of various life-times, some joint action of all the factors that affected the magnitude of the solar proton contribution to their production should be taken into account.

Table 2. Contributions of the solar protons (E > 20 MeV) into production of the measured contents of the radionuclides (in dpm kg^{-1}) in the Bruderheim, Jesenice and Stubenberg chondrites, which fell to the Earth, respectively, on March 4, 1960 (in the phase of maximum of the 19th solar cycle), on April 4, 2009 (on the growing branch of the 24th cycle) and on March 3, 2016 (at the drop of the 24th cycle).

	^{48}V	^{51}Cr	^{46}Sc	^{54}Mn	^{22}Na	^{55}Fe	^{26}Al
Buderheim	6.1	122.0	1.5	18.1	15.2	138.5	0.8
Jesenice	0	0	0	0	0.32	2.92	2.1
Stubenberg	0.09	1.85	0.02	5.4	44.4	404.8	2.8

The work is partly supported by Program № 28 of Fundamental Researches of the Presidium RAS

References:

Alexeev V.A., Ustinova G.K. Solar modulation of galactic cosmic rays in the three-dimensional heliosphere according to meteorite data // Geochemistry International. – 2006. – V. 44. – P.423–438.

Lavrukhina A.K., Ustinova G.K. Meteorites as probes of cosmic ray variations. – M: Nauka., 1990. – 262p.(in Russian).

Alexeev V.A., Laubenstein M., Povinec P. P., Ustinova G.K. Variations of cosmogenic radionuclide production rates along the meteorite orbits // Adv. Space Res. – 2015. – V. 56. – P. 766-771.

Bischoff A., Barrat J-A., Bauer K., et al., The Stubenberg meteorite – An LL6 chondrite fragmental breccia recovered soon after precise prediction of the strewn field // Met. Planet. Sci. – 2017**.** – doi:10.1111/maps.12883.

Bischoff A., Jersec M., Grau T., et al., Jesenice –A new meteorite fall from Slovenia // Met. Planet. Sci. – 2011. – V. 46. N 6. – P.793-804;

Ebeoglu D.B., Wainio K.M. Solar proton activation of the lunar surface //J. Geophys. Res. – 1966. – Vol.71. N. 24. – P. 5863-5872.

Lavrukhina A. K. and Ustinova G. K. Solar proton medium flux constancy over a million years // Nature . – 1971. – V. 232. – P. 462-463.

Meier, M.M.M. Meteorites with photographic orbits , 2016. (*http://www.meteoriteorbits.info*).

Parker E.N. Cosmic magnetic fields. // Space Sci. Rev. – 1969. – Vol.9, N 3. – P. 325-360.

Stozhkov, Yu.I., Svirzhevsky, N.S., Bazilevskaya, G.A., et al. Long-term (50 years) measurements of cosmic ray fluxes in the atmosphere. // Adv.Space Res. – 2009. – V. 44. – P. 1124–1137.

Yakovlev O. I., Shornikov S. I. Mg and Si isotope fractionation in dependence on acidity-basicity of CAIs melts

Vernadsky Institute of Geochemistry and Analytical Chemistry RAS, Moscow (*yakovlev@geokhi.ru*)

Abstract. High-temperature vaporization process of the chondrite Ca–Al–Inclusions (CAIs) is interesting for researchers as CAIs present the most ancient matter of Solar system. The CAIs consist of refractory minerals – hibonite, spinel, melilite, fassaite, anorthite, perovscite which consist of low fugacity oxides – Al_2O_3, CaO, TiO_2 and moderate fugacity oxides – MgO and SiO_2. The CAIs have clear features of mass-dependent isotopic fractionation Mg and Si, which, according to experimental data, are formed at high mass losses of evaporating melt. When CAIs melts evaporate at high temperatures, the SiO_2 and MgO volatilities are inverted: SiO_2, which is more volatile than MgO, becomes less volatile when melts are enriched in refractory CaO. This volatility inversion can be explained within the framework of the theory of acid–base interaction between components in silicate melts. According to this theory an increase in CaO concentration in the melt increases its basicity, and this, in turn, increases the activity (and hence, also volatility) of MgO and decreases those of SiO_2. This acidity-basicity factor has a strong effect on the rate of magnesium and silicon evaporation that in turn has a strong effect on isotope fractionation which as the melt evaporates increases the efficiency of isotopic fractionation in magnesium compared to silicon isotopes.

Keywords*: vaporization, condensation, Ca-Al-Inclusions, isotope fractionation, acidity-basicity factor.*

High-temperature evaporation processes in silicate melts are of great interest to researchers in connection with the study of the unique substance of the Solar system – Ca–Al–inclusions of chondrites. This substance is referred to as CAIs (abbreviation for "Ca–Al–Inclusions"). CAIs represent the oldest objects in the Solar system with an age of 4.567 billion years. They consist mainly of refractory minerals – hibonite, spinel, melilite, fassaite, anorthite, perovskite, and in the chemical relation of refractory oxides (Al_2O_3, CaO, TiO_2) and moderately volatile oxides (MgO and SiO_2). There are amazing isotope characteristics: high content of ^{16}O and daughter products of a number of short-lived isotopes in the CAIs composition. There are clear signs of mass-dependent isotope fractionation Mg, Si, O. At the same time, for some elements there are signs of nonlinear isotopic anomalies of unknown nature. Most researchers are of the opinion that CAIs formed by condensation of gas of Solar composition at the earliest stage of evolution of the Sun. Some researchers develop an alternative hypothesis according to CAIs are objects formed outside the Solar system. According to modern concepts, after the emergence of primary (condensate) products, processes of fractional high-temperature evaporation played a significant role in the formation of CAIs compositions. When evaporating, CAIs lost up to 50 % of magnesium and up to 25 % of silicon (Richter et al., 2002). The individual CAIs lost in evaporation of ~ 80 % of silicon and ~ 85 % of magnesium (Williams et al., 2017). Evaporative losses of magnesium, silicon led to deep mass-dependent fractionation of isotopes: $\delta^{25}Mg$ to 39 ‰; $\delta^{29}Si$ to 17 ‰ (Williams et al., 2017). Strong evidences of the differentiation during CAIs evaporation gave the isotopic analysis of Mg, Si, and O in the residual melts which were obtained in the vacuum experiments with corresponding initial compositions (Mendybaev et al., 2013).

To date, the CAIs origin and the particularities of their isotopic characteristics with respect to Mg and Si are clear and do not give rise to disputes. However, there are questions, and there are a lot of them, to the physico-chemical conditions of the evaporation process, namely, temperature, melt cooling rate, pressure and composition of the surrounding gas, the composition of the CAIs initial condensate. Here we will focus on an important, in our opinion, evaporation factor, which is usually not

considered in the list of primary evaporation conditions. It is the acid-base melt factor, which, among other factors, determines the evaporation sequence of MgO and SiO_2 oxides from CAIs melt, as well as the isotopic composition of magnesium and silicon in the residual melt.

In our paper (Yakovlev et al., 2017) we showed that D. S. Korzhinskii's theory on acid-base interaction of components in silicate melts (Korzhinskii, 1959) explains well the behavior of moderately volatile and different acid-base properties of MgO and SiO_2 oxides at evaporation from CAIs melts. It was shown that with the increase in the melt basicity, the parameter of which is the activity of oxygen ions, the activity of MgO, which has the base properties in the melt, should increase, and the activity of SiO_2, which has the acid properties in the melt, decrease. CAIs compositions can be described within the framework of the quadric oxide system $CaO–MgO–Al_2O_3–SiO_2$. According to the acid-base properties of oxides of these system are divided into acid (SiO_2), amphoteric (Al_2O_3) and basic (CaO and MgO).

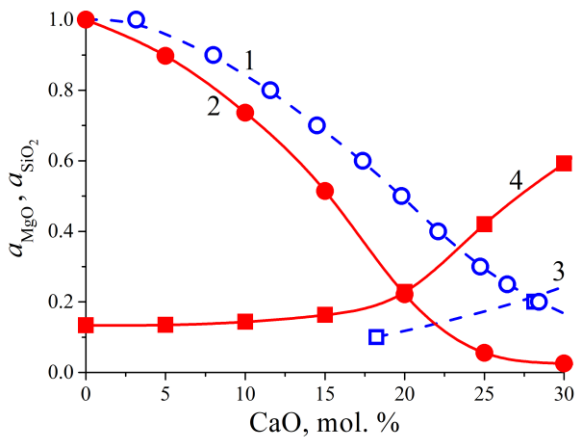

Fig. 1. Dependencies of SiO_2 (1, 2) and MgO (3, 4) activities in the $CaO–MgO–SiO_2$ melt *vs*. CaO content at temperature of 1600 °C and at constant mole ratio of $MgO / SiO_2 = 2 : 3$, calculated by: 1, 3 – (Rein and Chipman, 1965) and 2, 4 – (Shornikov, 2016).

Moreover, CaO has more basic properties and, accordingly, greater dissociation degree than MgO, and therefore CaO produces more oxygen ions during dissociation. For this reason, calcium oxide is the main donor of oxygen ions in the melt, and therefore its concentration plays a major role in determining the melt basicity parameter. It is logical to assume then that the MgO and SiO_2 activity depend and mainly determined by the CaO concentration in the melt, and thus, if the higher CaO content in the melt, than the higher the MgO activity values and lower the SiO_2 activity values. Theoretical calculations confirm this regularity (Rein and Chipman, 1965; Shornikov, 2016). Fig. 1 shows the dependencies of activities of SiO_2 (1, 2) and MgO (3, 4) in the ternary $CaO–MgO–SiO_2$ melt *vs*. CaO content at a temperature of 1600 °C and a constant mole ratio of $MgO / SiO_2 = 2 : 3$. The dependences presented in the Fig. 1 clearly illustrate the strong and opposite effect of CaO concentration on the MgO and SiO_2 activity. It is in full compliance with the Korzhinskii's theory of acid-base interaction of the melt components.

The general principle of acid-base interaction is directly related to the evaporation phenomena in vacuum and is the determining factor in a multicomponent melt evaporation. Indeed, the activity of the component in the melt determines the volatility or the partial pressure value of the component in the vapor. The dependence of the partial pressure of the component on its activity in the melt is expressed in the generalized Raoult-Henry law:

$$P_i = P_i^{\circ} a_i = P_i^{\circ} x_i \gamma_i, \quad (1)$$

where P_i is the pressure of the *i*th component over the melt; P_i° is the pressure of the *i*th pure component; a_i is the activity of the *i*th component in the melt; x_i is the molar fraction of the *i*th component in the melt; γ_i is the activity coefficient of the *i*th component in the melt.

The expression of the Raoult-Henry law shows that the volatility or, more correctly, the pressure of the *i*th oxide over the melt depends on three parameters:

1) the vapor pressure of the pure oxide, that is, its individual properties;
2) the oxide concentration in the multicomponent melt;
3) the interaction nature of oxide in the melt.

As shown above, the MgO and SiO_2 activities in melts depends on the CaO concentration, which plays a major role in the formation melt basicity. In accordance with this relationship, in the CAIs evaporating melt at the CaO content increasing, the magnesium oxide activity will increase (and accordingly the MgO volatility will increase too) and, on the contrary, the silicon oxide activity will decrease (and the SiO_2 will become less volatile).

Our studies also show that the acid-base interaction factor is also related to the phenomena of isotope fractionation of magnesium and silicon during their evaporation in vacuum. The MgO and SiO_2 activity and volatility changes during evaporation determine their evaporation rates from the melt. The evaporation rate of the component in vacuum is calculated by the Hertz-Knudsen equation:

$$J_i = \frac{\varphi_i P_i}{(2\pi RTm_i)^{1/2}}, \quad (2)$$

where J_i is the evaporation rate or flow of the ith substance when evaporating from the surface of the condensed phase (mol/cm^{2}sec); φ_i is the evaporation coefficient of the ith substance; P_i is the saturated vapor pressure of the ith substance (dyn/cm^2); m_i is the molecular weight of the ith substance (g/mol); R is the gas constant (erg/grad mol); T is the absolute temperature. Considering Raoult-Henry's low the Hertz-Knudsen equation needs to be rewritten in the form (Yakovlev et al., 1972, 1973):

$$J_i = \varphi_i(P_i^{\circ}a_i)/(2\pi RTm_i) - \varphi_i(P_i^{\circ}x_i\gamma_i)/(2\pi RTm_i) \quad . \qquad (3)$$

The obtained equation shows that at evaporation of multicomponent melt, the component evaporation rate is determined not only by the pure component vapor pressure, but also their concentration in the melt and the activity coefficient, taking into account the nature of the interaction of this component in the melt. The equation clearly shows the dependence of evaporation on the composition of the system. The concentration of each and every component of the melt changes (in particular, the CaO concentration increases) and, consequently, the general chemical environment and, consequently, the acidic-basic properties of the melt in the evaporation process. Under these conditions, the acid-base factor has a strong influence on the MgO and SiO_2 evaporation rates. It leads to the fact that the evaporative weight loss of magnesium are becoming higher relative to the weight loss of silicon.

In turn, the Mg and Si evaporation rates determine the efficiency of isotope fractionation, which increases in the basic acidity of magnesium oxide and decreases in acidic silicon oxide as the melt evaporates. We tested this statement using experimentally obtained data on magnesium and silicon isotopic fractionation measured in the residual melt after their evaporation (Mendybaev et al., 2013). The data were obtained at evaporation of the mixture (41.3 wt. % SiO_2; 3.0 wt. % Al_2O_3; 53.4 wt. % MgO; 2.4 wt. % CaO) at 1900 °C. The Fig. 2 shows the dependence of the $\delta^{26}Mg / \delta^{30}Si$ ratio on the calcium oxide content in the melt. The cross symbol shows the CaO initial content before evaporation. The data demonstrate more efficient mass fractionation of magnesium isotopes compared to mass fractionation of silicon isotopes as calcium oxide accumulates in the melt.

Thus, the accelerated weight loss of magnesium is determined by its increasing activity in the melt (as a consequence of the increase in the basicity of the melt during evaporation). In turn, it determine its effective mass fractionation of magnesium isotopes in comparison with the mass fractionation of silicon isotopes.

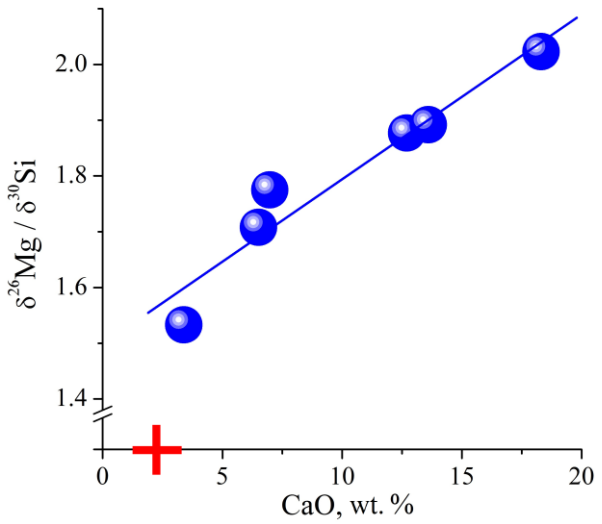

Fig. 2. Efficiency of fractionation of magnesium and silicon isotopes *vs*. the calcium oxide content. The CaO content in the initial composition is indicated by cross symbol.

References:

Korzhinskii D. S. (1959) Acid–base interaction of components in silicate melts and the direction of cotectic lines. *DAN SSSR*, vol. 128, no. 2, pp. 383–386.

Mendybaev R. A., Richter F. M., Georg R. B., Janney P. E., Spicuzza M. J., Davis A. M., Valley J. W. (2013) Experimental evaporation of Mg- and Si-rich melts: Implications for the origin and evolution of FUN CAIs. *Geochim. Cosmochim. Acta*, vol. 123, pp. 368–384.

Rein R. H., Chipman J. (1965) Activities in the liquid solution SiO_2–CaO–MgO–Al_2O_3 at 1600 °C. *Trans. Met. Soc. AIME*, vol. 233, no. 2, pp. 415–425.

Richter F. M., Davis A. M., Ebel D. S., Hashimoto A. (2002) Elemental and isotopic fractionation of Type B calcium-, aluminum-rich inclusions: Experiments, theoretical considerations, and constraints on their thermal evolution. *Geochim. Cosmochim. Acta*, vol. 66, no. 3, pp. 521–540.

Shornikov S. I. (2016) Thermodynamic properties of the CaO–MgO–SiO_2 melts. *Experiment in Geosciences*, vol. 22, no. 1, pp. 40–42.

Williams C. D., Ushikubo T., Bullock E. S., Janney P. E., Hines R. R., Kita N. T., Hervig R. L., MacPherson G. J., Mendybaev R. A., Richter F. M., Wadhwa M. (2017) Thermal and chemical evolution in the early solar system as recorded by FUN CAIs: Part I – Petrology, mineral chemistry, and isotopic composition of Allende FUN CAI CMS–1. *Geochim. Cosmochim. Acta*, vol. 201, pp. 25–48.

Yakovlev O. I., Kosolapov A. I., Kuznetsov A. V., Nusinov M. D. (1972) The results of the study of the fractional evaporation of basaltic melt in the vacuum. DAN SSSR, vol. 206, no. 4, pp. 970–973.

Yakovlev O. I., Kosolapov A. I., Kuznetsov A. V., Nusinov M. D. (1973) Features of K and Na vaporization from the melts in a vacuum. Moscow Univ. Geol. Bull., vol. 28, no. 5, pp. 85–88.

Yakovlev O. I., Ryazantsev K. M., Shornikov S. I. (2017) The role of acidity–basicity in evaporating refractory inclusions in chondrites. *Geochem. Int*., vol. 55, no. 3, pp. 251–256.